

UC Berkeley

UC Berkeley Electronic Theses and Dissertations

Title

Modeling Surface Stabilization in Nanoclusters and Nanoparticles

Permalink

<https://escholarship.org/uc/item/4rd1j956>

Author

McCandler, Caitlin

Publication Date

2024

Peer reviewed|Thesis/dissertation

Modeling Surface Stabilization in Nanoclusters and Nanoparticles

By

Caitlin McCandler

A dissertation submitted in partial satisfaction of the

requirements for the degree of

Doctor of Philosophy

in

Engineering - Materials Science and Engineering

in the

Graduate Division

of the

University of California, Berkeley

Committee in charge:

Professor Kristin Persson, Chair

Professor Mark Asta

Professor Eran Rabani

Summer 2024

Modeling Surface Stabilization in Nanoclusters and Nanoparticles

Copyright 2024
by
Caitlin McCandler

Abstract

Modeling Surface Stabilization in Nanoclusters and Nanoparticles

by

Caitlin McCandler

Doctor of Philosophy in Engineering - Materials Science and Engineering

University of California, Berkeley

Professor Kristin Persson, Chair

Nanoclusters, with their atomically-precise structures that have metal cores and molecular-like electronic structures, are interesting materials with a broad range of applications in energy and chemical industries. Gold clusters are of specific interest due to their high quantum efficiency, bio-compatibility, catalytic activity and selectivity. Current characterization techniques lack the temporal and spatial resolution required to understand the behavior of nanoclusters in relevant environments, and as such, synthetic efforts to design new nanoclusters largely rely on trial and error. This thesis describes several approaches to better understand the synthesis and stability of nanoclusters using theory and modeling.

As with all modeling, there are trade-offs between model complexity and efficiency. In this thesis, nanoclusters and nanoparticles are simulated with appropriate modeling techniques to answer the relevant questions that are posed at different length and time-scales. In the first part of this thesis, density functional theory (DFT) simulations are employed to map the potential energy surfaces of gold nanoclusters stabilized by ligands. Considering ensembles of clusters was very important in this work, and over 10,000 phosphine-stabilized gold clusters were generated with a ligation algorithm and their stabilities as a function of environment were calculated. These simulations give insight into the importance of ligands in determining stable cluster conformations, as well as the impact of cluster size and ligation on electronic structure and bonding. Next, simulations over longer time periods than would be tractable to calculate with DFT are performed, made possible by the development of an interatomic potential for thiolate-protected gold nanoclusters. The interatomic potential is fitted to many examples of DFT calculated nanoclusters and learns the energy-structure relationships that are present in all thiolate-protected gold nanoclusters. The potential is used to perform long ($\sim 0.1\mu\text{s}$) simulations of $\text{Au}_{25}(\text{SR})_{18}$, a known nanocluster that is remarkably stable. Interesting mechanisms are uncovered in the simulations which are not yet possible to observe experimentally. Finally, in order to understand the surprising miscibility of the immiscible elements Au and Rh in ultra-small nanoparticles, I developed a continuum model informed

by DFT calculations but applicable to any size of nanoparticle that depends on the enthalpy and entropy of mixing as well as surface energies and surface affinities to adsorbate species present in the synthesis conditions. The unusual mixing behavior observed experimentally is in fact due to the nature of the surface environment of the particle. Overall, at any length scale, the conclusion remains the same: the surface environment has a remarkable impact on nanocluster and nanoparticle energetics and behavior, and care must be taken to model them appropriately to achieve the goal of synthesis by design.

Contents

Contents	i
List of Figures	iii
List of Tables	v
1 Overview of the Dissertation	1
2 Introduction	3
2.1 Nanocluster Synthesis and Characterization	3
2.2 Nanomaterials Modeling Techniques	5
3 Ligation in Nanocluster Modeling	8
3.1 Abstract	8
3.2 Introduction	8
3.3 Results/Discussion	10
3.4 Conclusions	28
3.5 Methods/Experimental	30
3.6 Data	33
3.7 Supporting Information	33
3.8 Associated Content	33
3.9 Acknowledgements	34
4 Gold Nanocluster Dynamic Simulations	36
4.1 Introduction	37
4.2 Validation of the Potential: Structural, Vibrational and Dynamical Properties	38
4.3 Cluster Isomerization and Cluster-Cluster Reactions	42
4.4 Conclusion	46
4.5 Methods	49
4.6 Acknowledgements	53
4.7 Data Availability	53
5 Surface Environment Impact on Binary Metal Nanoparticle Phases	55

5.1	Summary of Quantitative Electron Microscopy of Au-Rh Nanoparticles . . .	55
5.2	Theoretical Analysis of Miscibility in Au-Rh Nanoparticles	56
5.3	Conclusions	66
5.4	Methods: DFT calculations	66
Bibliography		68

List of Figures

3.1	Energetic and size distributions of the >10,000 $\text{Au}_n(\text{PH}_3)_m$ structures in the dataset	10
3.2	Grand canonical energies of $\text{Au}_n(\text{PH}_3)_m$ as a function of m	12
3.3	Energies of $\text{Au}_7(\text{PH}_3)_m$ isomers for varying number of ligands, m	14
3.4	Energies of $\text{Au}_n(\text{PH}_3)_m$ isomers for varying number of ligands, m	18
3.5	An illustration of the concept of hidden ground states	21
3.6	Planar to non-planar transition as a function of particle size and ligand environment	22
3.7	s-d hybridization in planar and non-planar clusters	23
3.8	Cluster destabilization with greater s-d hybridization at higher ligand coverage	24
3.9	Ligand binding preference to corners and edges over facets of gold	25
3.10	$\text{Au}_n(\text{PH}_3)_m$ phase diagram	26
3.11	$\text{Au}_n(\text{PH}_3)_m$ phase diagram with monomers and dimers excluded	27
3.12	Odd-even effect in cluster energies	28
3.13	Possible transient intermediates in nanocluster growth	30
3.14	Ligation algorithm	31
3.15	Density of states (DOS) of representative examples of phosphine-stabilized gold clusters	35
4.1	Benchmarking of the potential: Energetics	40
4.2	Benchmarking of the potential: Dynamics	43
4.3	Au_{25} isomerization at 450K	44
4.4	Isomerization mechanism: $\text{Au}_{25\text{A}}$ conversion to $\text{Au}_{25\text{B}}$	45
4.5	Au_{25} coalescence and $[\text{AuSR}]_n$ ring formation at 500K	47
4.6	Snapshots of a MD simulation of Au_{25} coalescence and $[\text{AuSR}]_n$ ring formation	48
4.7	Systematic energy error in GPAW versions 1.3.0 and 22.8.0	50
4.8	Active learning: visualizations of extrapolation grade measurements	51
5.1	Experimentally determined phase diagram of Au-Rh nanoparticles with diameters ranging 1.2-4 nm	57
5.2	Thermodynamic mixing parameters of bulk and nanoscale Au-Rh systems	58
5.3	Schematic of constructions for core-shell, heterodimer and alloyed particles	60
5.4	Predicted adsorption energies of organic adsorbates to Au and Rh surfaces	61
5.5	DFT calculations of $\text{Au}_{101}\text{Rh}_{100}$ particles with and without CH_3 adsorbates	62
5.6	DFT calculations of the regular solution interaction parameter, w , for Au-Rh	63

5.7	Theoretical phase diagram of Au-Rh nanoparticles with diameters ranging 1.2-4 nm	64
5.8	Passivation effect on Au-Rh nanoscale phase diagram	65
5.9	Temperature effect on Au-Rh nanoscale phase diagram	66

List of Tables

3.1	Ligand binding energies	13
3.2	Hidden ground states	20
3.3	Experimental reference clusters	29
4.1	Known neutral gold-thiolate clusters: relaxation energy errors	39
4.2	Architecture of final potential	53

Acknowledgments

I would like to thank my advisor, Prof. Kristin Persson, for always making me feel that my work is worthwhile, and better yet, that I am more important than my research. Her encouragement and guidance allowed me to grow into a confident, independent researcher.

I would like to express my gratitude to Jakob Dahl for being a wonderful mentor, collaborator, and friend. I'll never forget him smiling and nodding through my entire first conference presentation. Thanks also to Matt Horton and Ryan Kingsbury for their sage advice and interest in my success. The wonderful Persson people are the best community I could have asked for here in Berkeley and I would like to especially acknowledge Guy Moore and Hetal Patel for being excellent listeners and friends.

I am so grateful that I have had the opportunity to collaborate with scientists around the world and bring some of their knowledge back to Berkeley. It was a particular pleasure and honor to join the lab of Prof. Hannu Häkkinen in Jyväskylä, Finland, for a semester. Thank you for hosting me, teaching me the history of the field of nanocluster science, and believing in our project. I want to acknowledge Noora and Pipsa Hyttinen for being especially welcoming during my time in Finland. I would also like to thank Prof. Ralf Drautz, Yury Lysogorskiy and Anton Bochkarev, for their time and advice when I was getting started using ACE potentials. Their commitment to making their work accessible by the scientific community is something that we should all strive to emulate. Here at Berkeley, I also was very lucky to be included on a project with Prof. Peidong Yang and his students Peng-cheng Chen and Mengyu Gao, which helped me connect my computational work to reality.

A sincere thank you to the NDSEG program and the Kavli Foundation for providing the funding that allowed me to elect my own research directions.

Finally, the biggest thank you to my family and friends, whose love and support mean everything to me. My time spent at Berkeley and in the PhD was comprised of many unexpected but happy experiences. Flynn, meeting you was the best one.

Chapter 1

Overview of the Dissertation

In this dissertation, I will focus on modeling nanocluster and nanoparticle syntheses, with the ultimate goal of directing synthesis outcomes in the future. Chapter 2 provides technical background relevant to all chapters, focusing on the stages of nanocluster and nanoparticle synthesis, current characterization techniques and limitations, and computational methods for modeling nanoscale systems with increased accuracy. The introduction contains text from Ref. [1] discussing nanoscale structure prediction and methods relevant for nanomaterials modeling. Effective modeling of reaction environments at different length scales (spatial and temporal) are discussed. Specifically, considerations of ligands and surface chemistry are highlighted as being especially important for modeling the synthesis of gold nanoclusters and multi-component nanoparticles.

Chapter 3 contains the complete article, Ref. [2], and investigates the extent to which stabilizing ligands change the potential energy landscape of nanoclusters. Specifically, we found that the presence of phosphine ligands dramatically changes the energetics and bonding of gold nanoclusters. Previous computational studies have successfully modeled gold nanoclusters in the gas phase, but their behavior in solution in the presence of protecting ligand groups is still poorly understood. These results showcased the necessity of including ligands in calculations of nanocluster energies, as well as the predictive power of high-throughput methods for discovering gold nanocluster products and their formation pathways.

Most problems in nanocluster synthesis, namely the simulation of ensembles of clusters, clusters in the mid-size regime ($n=20-150$), and dynamic processes, are beyond the scope of first-principles methods. When density functional theory becomes intractable, less expensive methods can be used instead, including a fitted interatomic potential for the specific system. In Chapter 4 I discuss the development of an Au-S-C-H interatomic potential and its application to thiolate-protected gold nanoclusters. This work will be published in ACS Nano, and is currently available as a preprint article (Ref. [3]). As an initial use case of this Au-S-C-H interatomic potential, I simulated the isomerization, agglomeration and coalescence of $\text{Au}_{25}(\text{SR})_{18}$ gold nanoclusters. Agglomeration and coalescence are important but not well understood factors affecting the synthesis, storage and stability of nanoclusters. Specifically, understanding the mechanisms and conditions that give rise to agglomeration versus coa-

lescence for nanoclusters will have implications on the lifetime of stability for nanoparticle seed precursors, the metastability of non-equilibrium structures, the calcination process in heterogeneous catalysis, and for the impact of processing techniques such as precipitation, centrifugation, washing and drying on final synthesis outcomes.

In the final chapter, Chapter 5, I discuss a thermodynamic model that explains the observed miscibility of the immiscible elements Au and Rh in ultra-small nanoparticles. I summarize the experimental observations made by Prof. Peidong Yang's group in order to motivate my theoretical contribution to the work Ref. [4]. Predicting synthesis outcomes for nanoparticles, even small nanoparticles with diameters less than 10 nanometers, requires a different approach than for nanoclusters in which each atom can tractably be modeled. Additionally, when multiple elements are present, it is important to consider the thermodynamics of mixing the two elements in addition to the surface effects. In order to capture all the relevant effects that govern synthetic outcomes of Au-Rh nanoparticles, I develop a thermodynamic model that predicts the miscibility and phase separation of Au-Rh as a function of size. Notably, the mixing behavior matches the experimental observations only when passivating species are present that stabilize the nanoparticle surfaces.

Chapter 2

Introduction

Reproduced in part with permission from “Yang, R.X., McCandler, C.A., Andruic, O., Siron, M., Woods-Robinson, R., Horton, M., Persson, K.A. Big Data in a Nano World: A Review on Computational, Data-Driven Design of Nanomaterials Structures, Properties, and Synthesis. ACS Nano 2022, 16, 12, 19873–19891” Copyright 2022 The Authors.

2.1 Nanocluster Synthesis and Characterization

Nanoclusters (NCs) are a subclass of nanoparticles, delineated as such due to their ultrasmall sizes. NCs comprise up to 100–150 atoms (<1 nm), while nanoparticles generally refer to larger structures between 1 and 100 nm. This distinction originates from the irregularity of nanoclusters, which have stronger quantum confinement effects, off-lattice atomic arrangements, variable bond lengths, and more diversity in their resulting properties. On the other hand, nanoparticles typically exhibit atomic configurations and symmetries that resemble the bulk crystal structure, which in turn correlates with more predictable properties. The properties of NCs are greatly dependent on their composition, size, atomic configuration, and surface functionalization. NCs are of practical interest because they exhibit large surface areas that are ideal for catalyzing reactions and discrete electronic states for optical applications.

In nanocluster synthesis, precise control of the shape, size, and stoichiometry is important for harnessing the diverse electronic, magnetic, optical and catalytic properties uniquely seen at this scale. A study by Nesbitt *et al.* on the catalytic activity of Au₁₉, Au₂₀ and Au₂₂ provides an excellent example of how different-sized NCs can have unpredictable properties: the conversions measured for the best performing catalysts were 2-3 times higher than those of the worst performing catalysts, even though the NCs differed by only one Au atom.[5] Atomic precision is therefore clearly important, but the reasons for the differences in performance and stability are still not well understood.

Solution-based growth, also called colloidal synthesis, is the preferred method to synthesize nanoclusters for several reasons. It offers the introduction of protective ligands to im-

prove separation, storage, and size control.[6] Additionally, solvated nanoclusters are required for solution-based processes including photocatalysis, thin film processing, and drug delivery. Typical colloidal nanoparticle syntheses are mediated by ‘seeds’, which are small nanoparticles or nanoclusters that serve as nuclei, and are either purchased or pre-synthesized. Nanoparticle synthesis is then performed by injecting seeds and other precursors (reducing agents, a monomer source, stabilizing ligands, etc.) into a hot solution of a surfactant and a high boiling point solvent to limit the kinetic barrier to growth.[7] Nanocluster syntheses, on the other hand, aim for products with atomic level precision and, therefore, rely on different methods—which are often more complicated. In practice, very specific and unpredictable methods are in many cases required to achieve specialized shapes and sizes. As a representative example, the synthesis of $[\text{Au}_{19}(\text{PHC}\equiv\text{C})_9(\text{Hdppa})_3](\text{SbF}_6)$ detailed by Wan et. al. involves the dropwise addition of a reducing agent to monomer precursors for 18 hours, then evaporation to dryness, redissolution, centrifugation, filtration, precipitation, and additional centrifugation. The dissolution-precipitation procedure is then repeated until the supernatant is colorless.[8, 9]

In addition to modifying solvents, reducing agents, temperature, *etc.* in a colloidal synthesis, changing the stabilizing ligand has an impact on the surface energies of the nanocrystal and results in different synthesis products. The most successful and well-studied ligands for the gold nanocluster system are phosphine, thiolate, and halides because of their strong binding that inhibits uncontrolled growth. Although ligands play an important role in nanocluster synthesis, the behavior of nanoclusters has been studied mainly theoretically in the gas phase without stabilizing ligands.[10–27] Importantly, the ground states predicted for vaporized gold do not resemble colloidal products. As an example, the ground state of the Au_{13} gas phase nanocluster has been highly studied and debated in literature, with at least 14 density functional theory (DFT) studies finding 12 unique structures to be the ground state.[10, 13, 16–25, 27, 28] None of these 12 different proposed gas phase structures resemble the icosahedral geometry seen in solution phase experiment.[29] Additionally, Johnson et. al.[30] performed experiments exchanging one phosphine ligand, PR_3 , for another with increasing sizes of functional groups, R, and found that ligand binding energies increase with size of ligand, concluding that ligand substitution is necessary to consider in the theoretical modeling of these nanoclusters.

Several characterization techniques are possible for the study of nanoclusters, but each has fundamental limitations in resolution. With a combination of all the main techniques—mass spectroscopy (MS), small-angle X-ray scattering (SAXS), single crystal x-ray diffraction (SCXRD), X-ray absorption fine structure spectroscopy (XAS), liquid cell transmission electron microscopy (LC-TEM)—one can learn about the size distribution of clusters in a solution and the configurations of the heavy atoms in a single-crystal of nanoclusters. In most cases, however, the knowledge of the nanocluster geometry from X-ray techniques does not have atom-level resolution and the ligand-metal interfaces are ill-defined.[31] Electron microscopy has improved enough to see, with rapid sampling, some configurations of nanoclusters, but likely not the thermodynamic cluster, due to the huge amount of energetic perturbation on the system from the electron beam energy.[32]

Over the past two decades, colloidal nanoclusters have been synthesized with increasing diversity and identified with atomic-level precision.[30] This has led to greater interest in *directing* the synthesis to design new specific shapes and sizes. However, experimental nanocluster characterization is time-intensive due to the difficulty of isolating nanoclusters in high enough purity for X-ray crystallography. Synthetic yields can be low because of poor selectivity and transient, metastable intermediate clusters may be difficult to isolate or probe with in-situ characterization techniques. Identifying stable nanocluster geometries computationally can help validate experimental measurements and guide new synthesis efforts. Hence, improved predictions of stable structures, intermediate clusters, and possible reaction pathways provide a guide to possible synthesis products of specific structure and size, as well as fundamental understanding of how these nanoclusters form.

2.2 Nanomaterials Modeling Techniques

In nanomaterials, the size and morphology provide extra degrees of freedom that add tunability of properties as well as complexity of the available phase space. To explore and direct synthesis efforts in this phase space, computational structure prediction can provide a map of stable, low-energy synthesizable configurations. Nanoparticles are one class of nanomaterials that have a wide range of shapes and sizes. Identifying stable nanocluster geometries computationally is important for comparing to experimental measurements and directing synthesis efforts; however, the time and length scales will generally determine the level of theory that is computationally tractable.

The computational method that offers the greatest accuracy in calculating nanocluster systems is coupled cluster theory, but this method is extremely expensive and currently intractable for calculating structural relaxations, large nanoclusters/nanoparticles, or ligated clusters. Initial work has been done to approximate the coupled cluster theory accuracy for nanoclusters interacting with oxide surfaces,[33] and future developments in coupled cluster theory may eventually enable more accurate calculations. The highest level of theory that is currently tractable for the study of protected nanoclusters is DFT. Some nanocluster DFT calculations employ dispersion corrections, hybrid exchange–correlation functionals, spin–orbit coupling, and implicit/explicit solvation for increased accuracy. It is important to note that DFT captures ground state energies at zero Kelvin and relies on exchange–correlation functionals that approximate electron–electron interactions. As mentioned in the previous section, DFT has been known to struggle to predict the ground state structures of even bare nanoclusters in the gas phase, with 14 studies predicting 12 unique ground states for Au_{13} depending on the functional and structure searching methods used.[10, 13, 16–25, 27, 28] Even considering the approximations made with DFT, DFT is typically too expensive of a method for calculating a larger nanoparticle, an array of many nanoclusters, or a simulation over many time steps. For this reason, less computationally expensive methods are typically used to estimate the structure and energies, including semi-empirical tight binding methods or interatomic potentials.[34] The potential energy surface (PES) of

a nanostructure dictates the global minima, i.e., the most stable atomic configurations given the composition. Sampling the entire PES via first-principles methods in the complex geometry is computationally infeasible; hence, a number of structure generation methods have been developed.

The major techniques to generate plausible structures are genetic algorithms,[35] basin hopping,[36] random structure searching,[37] and simulated annealing.[38] Less standard methods include particle swarm algorithms[39] and other variants of these broad methods including tree growth algorithms,[40] Tabu ("taboo") algorithms,[41] and ab initio random structure searching (AIRSS).[42] Several reviews have previously highlighted these techniques and their advantages for certain systems.[43–45] Furthermore, some of these algorithms have been adapted to screen for properties beyond thermodynamic stability, such as vertical electron affinity.[46, 47] An efficient method to rapidly generate structures is to simply reuse and recalculate structures that were previously found for similar elements. As an example of this approach, Sokol et al. conducted a data mining study with the idea that binary heteropolar materials have similar energy orderings to each other and showed that the low-energy structures of $(\text{ZnO})_n$ clusters exhibit similar energy orderings when applied to other binary heteropolar materials such as $(\text{AlN})_n$. [48] The tendency of certain elements to behave similarly at the nanoscale can be quantified by comparing the relative ordering of stabilities for structures with each element. The similarity of different elements at the nanoscale was quantified by comparing the energy rankings of clusters with similar atomic arrangements at the nanoscale for all elements in the Quantum Cluster database. [49] A study conducted by Chaves et al. is another example of a systematic study of transition metal nanoclusters, where they used structures from the literature as a starting point and then conducted a Monte Carlo Revised Basin Hopping Structure Search.[23, 50, 51]

An interatomic potential (IAP) is an empirical parametrization of a potential energy surface that can be fitted to nanoparticles. Recently, machine-learned potentials (MLPs) specifically applied to nanoparticle systems have become increasingly sophisticated and can rival traditional atomistic methods. Machine learning potential regression methods bring benefits over more traditional physics-based methods in that the models can be built agnostically to the material, applied to a diverse set of input systems, and have been shown to improve the topology of the PES.[34, 52, 53] It is important to note that, like any parametrized model, MLPs are fundamentally limited by the quality of their training data. Many, on the order of 50000, first-principles calculations of nanoclusters, including their structures, energies, and forces, are required to fit IAP models with very good accuracy,[53, 54] with the possibility of reducing that number to 500 calculations by using active learning that iteratively queries the energy landscape in regions of failure and updates the training pools.[55] IAPs excel at small structures for which we can sample many configurations, and large structures in which bulk-like behavior and surface facets dominate. On the other hand, medium-sized structures, on the order of a few hundred atoms large, are challenging because they fall between the two regimes—they are typically too large for first-principles approaches and too disordered to model as a bulk crystal with surface facets. Bridging the data gap between these two length scales will be the key to future developments in nanoparticle structure prediction.

Cluster expansions, methods typically applied to bulk crystals with well-defined lattices, have emerged as a possible approach to rapidly estimate the energies of nanoparticles. Cluster expansions have effectively modeled the surface and adsorbates of nanoparticles.[56, 57] An off-lattice cluster expansion formalism, the Atomic Cluster Expansion (ACE), has recently been developed by Drautz.[58] PACE, the performant open-source implementation of ACE, has exhibited comparable accuracy and performance for small Cu and Si clusters as other MLPs.[54] Other equivariant MLPs that have recently emerged and show excellent accuracy include the Neural Equivariant Interatomic Potential (NeQuip),[59] Allegro,[60] and MACE[61] (a message-passing variant of ACE). We emphasize the usefulness of diligent data reporting standards, as combining data from several individual studies can provide a superior starting point for further development by furnishing informed guesses of stable structures when considering a new system. Curating quality data on the energies and geometries of nanoparticles will act as innovation multipliers across a wide range of nanomaterial design efforts. Furthermore, the record of prior tuned/trained IAP speeds up the development of potentials, thus improving the efficiency of structure prediction. We note here the example of OpenKIM and NIST interatomic potential repositories, which have archives of previously fitted potentials for many systems.[62–64] Databases such as these provide excellent avenues to build on existing work and close the gap from bulk to nanostructures.

Chapter 3

Ligation in Nanocluster Modeling

Reproduced in part with permission from “McCandler, C. A., Dahl, J. C., and Persson, K. A. Phosphine-Stabilized Hidden Ground States in Gold Clusters Investigated via a $Au_n(PH_3)_m$ Database. ACS nano 17.2 (2022): 1012-1021.” Copyright 2022 The Authors.

3.1 Abstract

Nanoclusters are promising materials for catalysis and sensing owing to their large surface areas and unique electronic structures which can be tailored through composition, geometry, and chemistry. However, relationships correlating synthesis parameters directly to outcomes are limited. While previous computational studies have mapped the potential energy surface of specific systems of bare nanoclusters by generating and calculating the energies of reasonable structures, it is known that environmental ions and ligands crucially impact the final shape and size. In this work, phosphine-stabilized gold is considered as a test system and DFT calculations are performed for clusters with and without ligands, producing a database containing >10,000 structures for $Au_n(PH_3)_m$, ($n \leq 12$). We find that the ligation of phosphines affects the thermodynamic stability, bonding, and electronic structure of Au nanoclusters, specifically such that ‘hidden’ ground state cluster geometries are stabilized that are dynamically unstable in the pure gold system. Further, the addition of phosphine introduces steric effects that induce a transition from planar to non-planar structures at 4-5 Au atoms rather than up to 13-14 Au atoms as previously predicted for bare clusters. This work highlights the importance of considering the ligand environment in the prediction of nanocluster morphology and functionality, which adds complexity as well as a rich opportunity for tunability.

3.2 Introduction

Nanoclusters (NCs), a class of ultra-small nanoparticles, are promising materials for catalysis, fluorescent sensors, bioimaging, nanomedicine and precursors for nanoparticle synthesis.

These materials measure less than 2 nm (<150 atoms) and exhibit molecular-like electronic structures as well as irregular atomic configurations. Their electronic and physico-chemical properties are highly dependent on their composition, size, atomic configuration, and surface functionalization. Additionally, NCs exhibit large surface areas that are ideal for catalyzing reactions and discrete electronic states for optical applications.

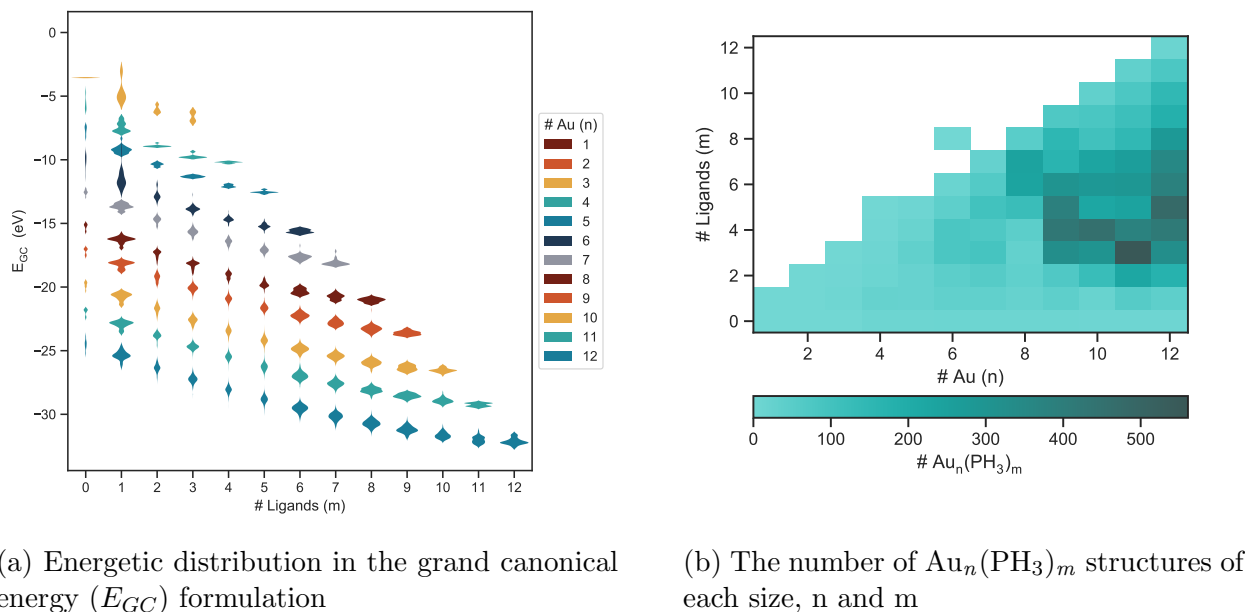
It has been over 50 years since a gold cluster was first crystallographically resolved,[65] and over the past two decades, nanoclusters have been synthesized with increasing diversity and identified with atomic-level precision.[66] This has led to greater interest in *directing* the synthesis to design specific shapes and sizes. However, experimental nanocluster synthesis is time-intensive due to the difficulty of isolating nanoclusters in high enough purity for characterization and X-ray crystallography.[67] Synthetic yields can be low due to poor selectivity, and transient, metastable intermediate clusters may be difficult to isolate or probe with *in situ* characterization.

Hence, improved predictions of stable structures, intermediate clusters and possible reaction pathways provide a guide to possible synthesis products of specific structure and size, as well as fundamental understanding of how these nanoclusters form.

Solution-based growth is the preferred method to synthesize nanoclusters for several reasons. Firstly, it offers the introduction of protective ligands to improve separation, storage and size control.[6] Secondly, solvated nanoclusters are required for solution-based processes including photocatalysis, thin film processing and drug delivery. Combinations of ligands can provide a variety of stable configurations and surfaces, and result in highly variable catalytic performance.[68] Importantly, ligation has been shown to be more effective at controlling the synthesis product than using kinetic control.[69] It is clear that cluster thermodynamic stability as well as electronic structure and bonding are fundamentally influenced by the presence of ligands.

The structural and thermodynamic landscape of nanoclusters can be effectively explored using computational techniques. Indeed, global structure searching studies have extensively characterized the potential energy surface (PES) for bare gold clusters in the gas phase and have been highly successful in predicting the products of gold vaporization. [10–26] Additional work has been done to predict the geometry of the ligand shell given the precise locations of the metal core atoms, [31] to monitor the impact of SCH₃ on Au₁₁, [70] PH₃ on Au₁₃ [71] and Au₈, [72] PH₃ and Cl on Au₅₅, [73] and PH₂(CH₂)_MPH₂ (spacer M = 3, 5) on cationic Au_n (n = 7–11). [74] However, to the best of our knowledge, there has been no work examining how ligation changes the sequence of stable cluster geometries, effectively stabilizing otherwise ‘hidden’ ground states.

Here we present an extensive, grand canonical, data-driven study on ligated neutral gold clusters, spanning >10,000 structures. We map the impact of ligation on the core gold structure (gold kernel), and analyze trends in preferred ligand binding sites, ground state geometries, and hybridizations of gold-gold bonding. As a model ligand, we select phosphine, which exhibits weaker binding energies than thiolate ligands, and is hence more suitable for catalysis [75] and leads to less structural rearrangement. While clusters tend to adopt positive charge according to the superatom model of stable electron counting, [76] we consider only

Figure 3.1: Distributions of the $Au_n(PH_3)_m$ dataset

neutral clusters here. We show that, for the open system of phosphine and gold, phosphine ligation constitutes a crucial factor in the global search for stable nanocluster ground states.

3.3 Results/Discussion

Population Distribution

The ligation generation algorithm (see Computational Methods and Details) resulted in 10,868 distinct $Au_n(PH_3)_m$ ($n \leq 12$) structures, which includes the initial set of pure gold structures, as well as an addition of the monomer, dimer, and experimental structures from the CSD.[77] Due to the relaxation of a gold core in presence of ligands, a highly diverse set of nanoclusters were produced. In total we obtained 4516 additional distinct geometries, as defined by having different gold structures to the original set. Details of the energy distribution and the number of structures calculated for each size are shown in Figure 3.1. Larger gold core sizes generated more structures due to the increased combinatorial space of ligand sites. It should also be noted that the initial gold kernels were the lowest energy species in the previously performed global energy search conducted to create the Quantum Cluster Database,[24] and as such are useful for the comparison with the PES of bare gold NCs.

The weaker binding energy and the single lone pair of electrons in phosphine ligands leads

to a simple radial monodentate binding motif, which is easier to model than the complicated ‘staple’ motif that thiolate ligands with three lone pairs available for binding adopt. Also, the weaker binding of phosphine causes less structural rearrangement of the gold NC core. Finally, a simple PH_3 ligand can be substituted for the more complex but more commonly used triphenyl phosphine (PPh_3) to reduce the computational cost while still capturing some of the steric interactions, unlike halides. However, we emphasize that some important differences to experimentally used ligands remain, including less steric hindrance, weaker binding energies, less electronegativity, and less polarizability.[78–82] Further, bidentate phosphine ligands are not expected to be well represented with a simple PH_3 ligand.

Grand Canonical Energy Formulation

The grand canonical energies of the structures were obtained according to

$$E_{GC} = E - n\mu_{Au} - m\mu_{PH_3} \quad (3.1)$$

where n represents the size of the gold cluster (number of gold atoms), and m represents the number of PH_3 ligands in the cluster. All subsequent discussion of energy will refer to the grand canonical energy.

The chemical potentials of gold and phosphine, μ_{Au} and μ_{PH_3} , were calculated with DFT as the total energy of a gold atom and a phosphine complex in vacuum and were obtained as -0.29 eV and -15.62 eV respectively. The grand canonical energies of all structures in the dataset are shown in Fig. 3.2, as a function of the number of bonded ligands.

We note that there is likely a window of relevant chemical potentials, accessible by tuning the composition and concentration of the solution. For example, by applying the entropy correction of phosphine in the gas phase at 300K provided in the NIST database,[83] the resulting chemical potential of phosphine would lower to -16.28 eV/ PH_3 . Lower chemical potentials indicate a more stable environmental phosphine state, which competes strongly with the gold nanocluster ligation. We find that using the NIST gas phase value results in sparingly ligated ground states, in contrast with experimental observations. Hence we expect that most relevant solution chemical potentials of phosphine to be higher than -16.28 eV. Using the higher DFT calculated μ_{PH_3} , we find that ligand binding energy tapers off when sizes, n , are equal to number of ligands, m . The ligand binding energy also decreases for larger structures of gold, meaning that a ligand is more stabilizing for smaller structures. A summary of the calculated ligand binding energies are included in table 3.1. The most stable structures of all ground states with $n = m$ were examined for ligand saturation, however none of the structures, given the starting positions, were able to accommodate another ligand. Some experimentally realized structures, however, are able to bind more ligand head groups than gold atoms, typically by utilizing bidentate ligands (CSD IDs: 1541477,[84] 1009716,[85] 862706[86]).

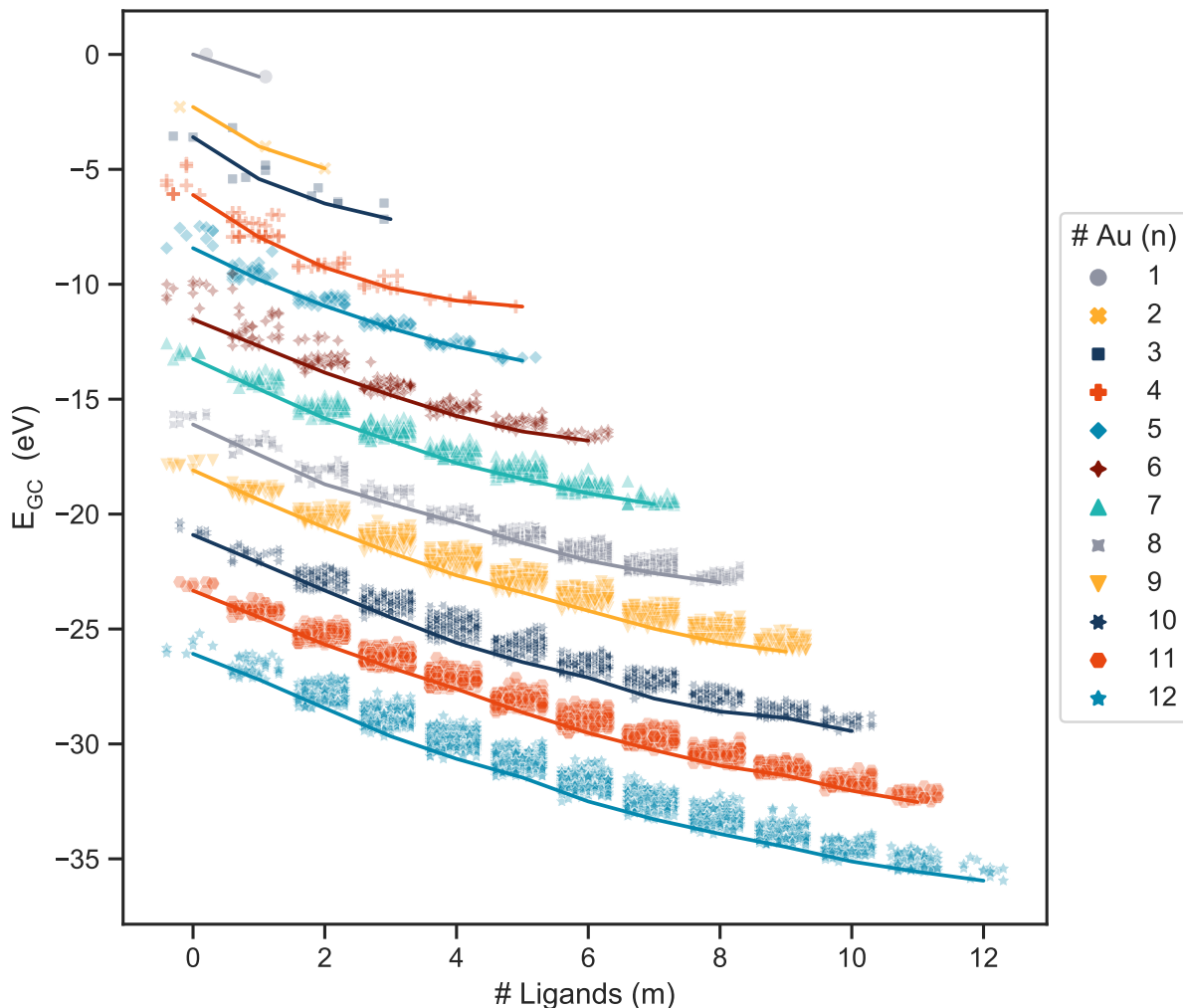


Figure 3.2: Grand canonical energies of the >10,000 structures in the dataset, including the experimental set. $\mu_{Au} = -0.29$ eV and $\mu_{PH_3} = -15.62$ eV. The slope of the guide lines indicate the ligand binding energies. The ligand binding energies are tabulated in the SI (table S1).

Thermodynamic Stability Ranking

We find that the predicted ground states, and thermodynamically ranked isomers depend strongly on the number of ligands bound to the nanocluster. This demonstrates that ligands stabilize some geometries more than others, and that using the bare nanocluster energy rankings is not sufficient to predict the sequence of stable nanocluster structures as a function of size in an environment where ligating species are available.

In order to analyze the impact of ligands on the relative thermodynamic stability, struc-

Au _n	PH ₃ Ligand Binding Energy (eV)											
	1st	2nd	3rd	4th	5th	6th	7th	8th	9th	10th	11th	12th
Au ₁	0.967											
Au ₂	1.715	0.961										
Au ₃	1.819	1.070	0.681									
Au ₄	1.836	1.322	0.905	0.536								
Au ₅	1.367	1.147	0.968	0.810	0.604							
Au ₆	1.159	1.156	0.981	0.909	0.674	0.398						
Au ₇	1.313	1.276	0.974	0.973	0.692	0.625	0.470					
Au ₈	1.319	1.283	0.851	0.810	0.888	0.776	0.542	0.405				
Au ₉	1.286	1.212	1.087	0.991	0.739	0.799	0.782	0.609	0.388			
Au ₁₀	1.202	1.216	1.172	1.105	0.838	0.679	0.908	0.565	0.280	0.571		
Au ₁₁	1.152	1.192	1.005	0.929	1.019	0.897	0.746	0.676	0.429	0.661	0.496	
Au ₁₂	1.123	1.244	1.220	0.982	0.813	1.042	0.776	0.635	0.567	0.633	0.446	0.388

Table 3.1: Ligand binding energies. Calculated using Eq. 3.2 with $\mu_{PH_3} = -15.62$ eV

tures with the lowest energy for a given gold kernel geometry were identified from each set of structures with n gold atoms and m ligands. Figure 3.3 shows the differences in the thermodynamic stability between the isomers and the ground state structure with the same number of m ligands for a representative 7 gold atom kernel size. All other sizes between $n=3-12$ are included in Fig. 3.4. Relevant gold kernel geometries are identified and show large differences in calculated energies above the hull as a function of ligation. Importantly, we find that structures that have been observed experimentally (CSD IDs: 2023935,[87] 668368,[88] 1123093,[90] 1123094,[89] 1123095[91]) were correctly identified as ground states only with $m=6$ and $m=7$. Notably, these structures are 200 meV and 470 meV above the hull, respectively, in their bare, unligated state. Further, the ground state bare Au₇ cluster is not present in the Au₇(PH₃)₇ set because the core gold geometry undergoes significant reorganization to accommodate 7 ligands; hence there is no structure-matched equivalent ligated structure.

Below, we summarize some of the findings and comparisons to experimental synthesis products for each gold kernel size, n . In these comparisons, it is important to keep in mind that synthesis procedures involve crystallization and other post-synthesis techniques in order to improve selectivity. Also, any experimental structure that relaxed away from the geometry (and bonding) reported in the CSD were not considered as experimental references but are included in the dataset.

n=4: The experimentally realized Au₄ structure is a tetrahedron with 4 ligands (CSD IDs: 1206655,[92] 1231463[93]). The bare tetrahedral structure is energetically unfavorable in computations, though it becomes notably more stable with ligation, improving agreement

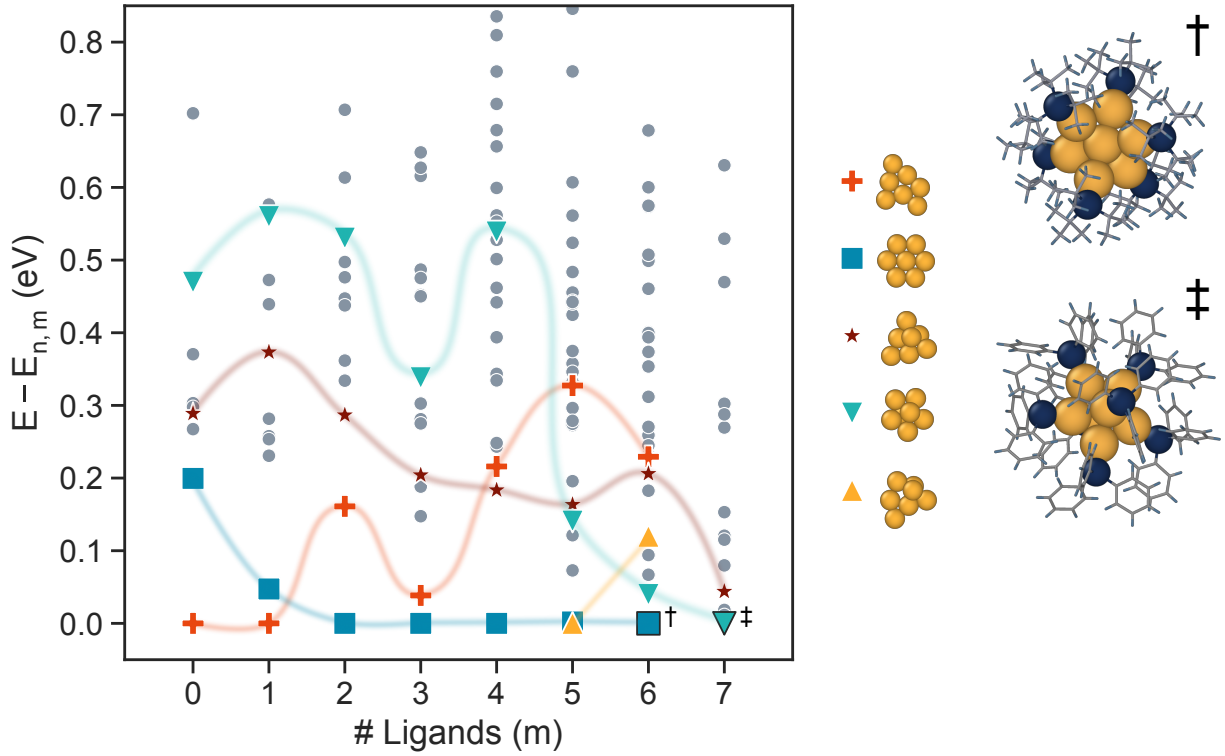
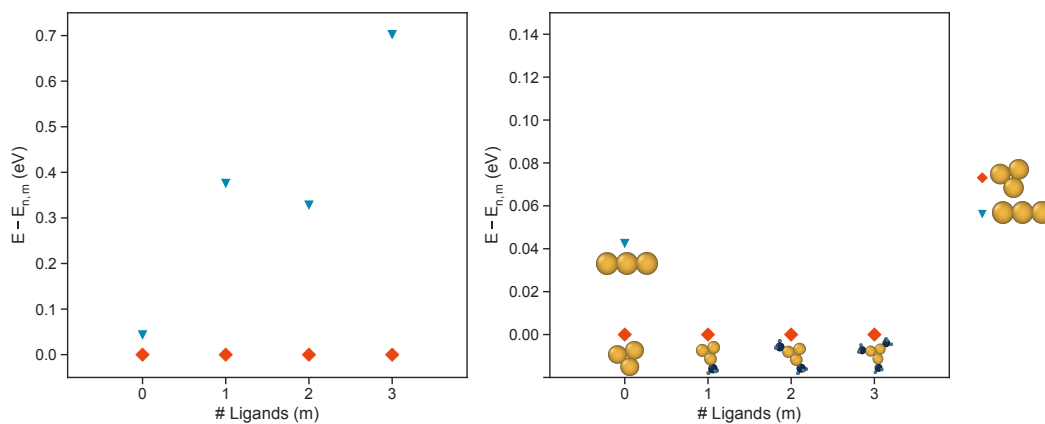


Figure 3.3: Energies of $\text{Au}_7(\text{PH}_3)_m$ isomers for varying number of ligands, m , showing the strong influence of ligation. The energies are referenced to the minimum value for each m , $E_{7,m}$. Each point represents a distinct gold kernel with the optimal ligand configuration for the given m ; four gold kernels are highlighted in order to demonstrate how relative energies change with ligation. Experimental structures from literature sourced from the CSD are denoted with black outlines. Here, experimental structures are the lowest in the energy orderings for 6^\dagger (CSD ID: 2023935[87]) and 7^\ddagger (CSD IDs: 668368,[88] 1123094,[89] 1123093,[90] 1123095[91]) ligands.

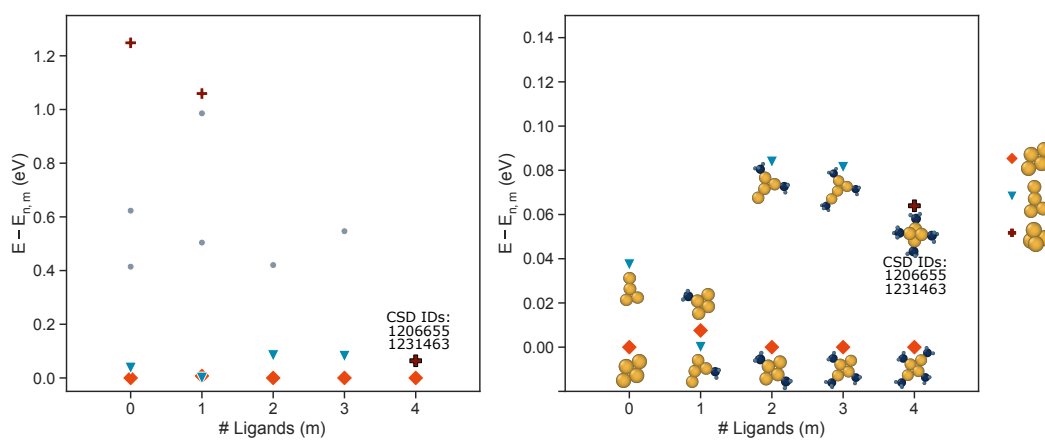
with experimental observations.

n=6: Two experimental clusters are considered (CSD IDs: 1120743,[94] 1272194[95]). These structures are slightly distorted from a square bipyramidal geometry and an octahedral geometry, and were ranked 5th and 9th among the computed $\text{Au}_6(\text{PH}_3)_m$, at 14 meV/Au and 55 meV/Au above the most stable cluster. The two most theoretically stable gold kernels differ from the lowest energy experimental structure only by the rearrangement of 1 gold atom. Without ligation, the most stable Au_6 structure is a planar triangle, but with ligation this planar structure is destabilized to 29 meV/Au above the most stable n=6 structure.

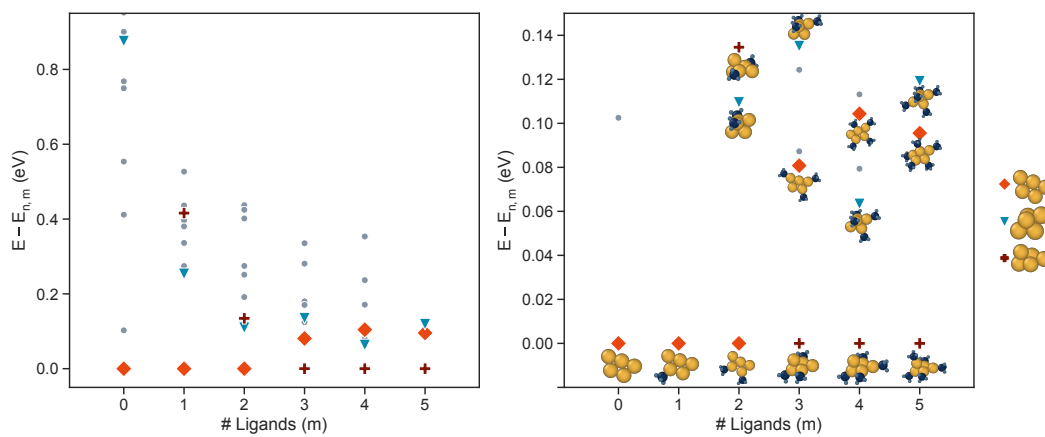
n=8: One experimental structure retained its initial geometry during DFT relaxation



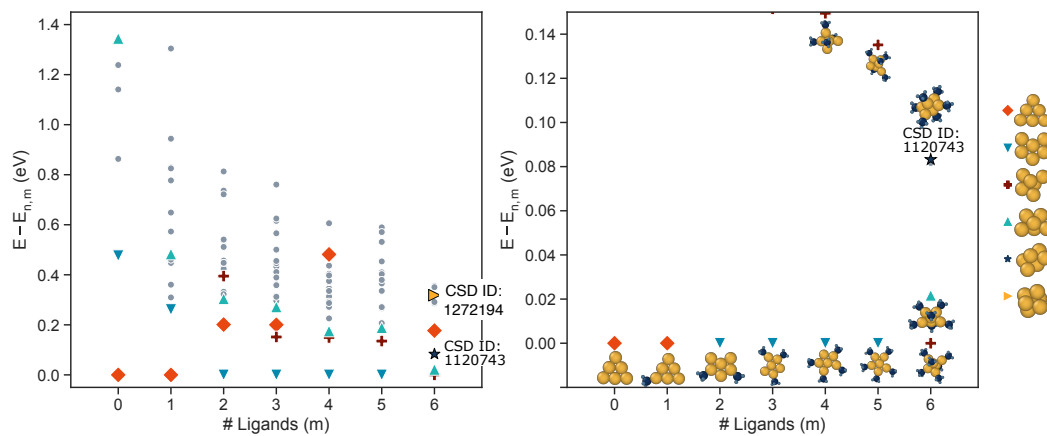
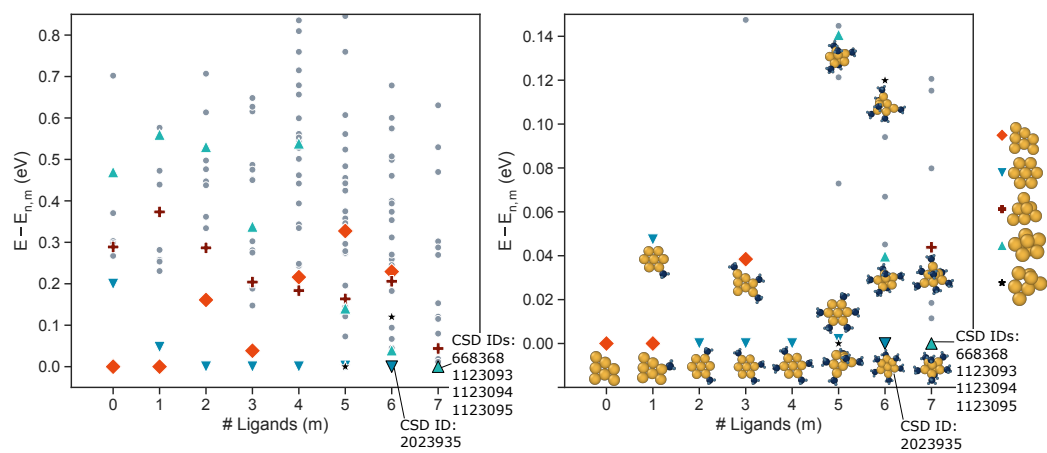
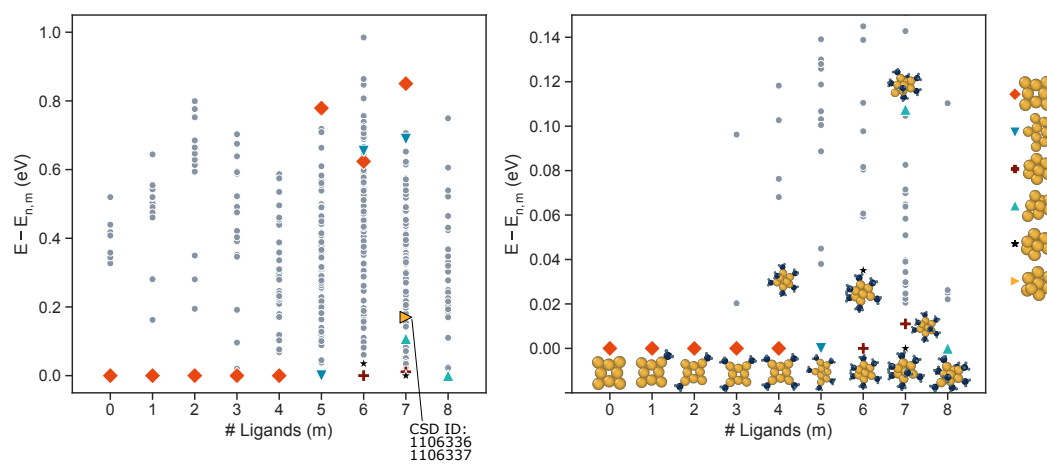
(a) n=3

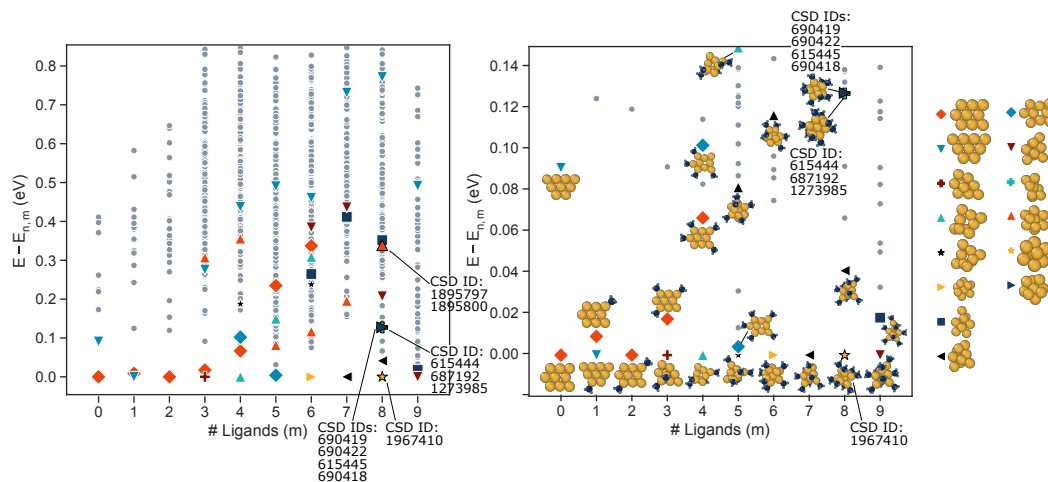
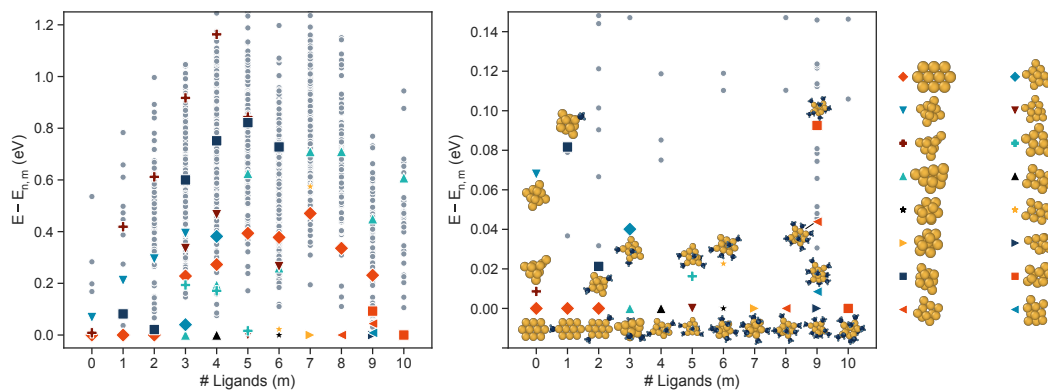
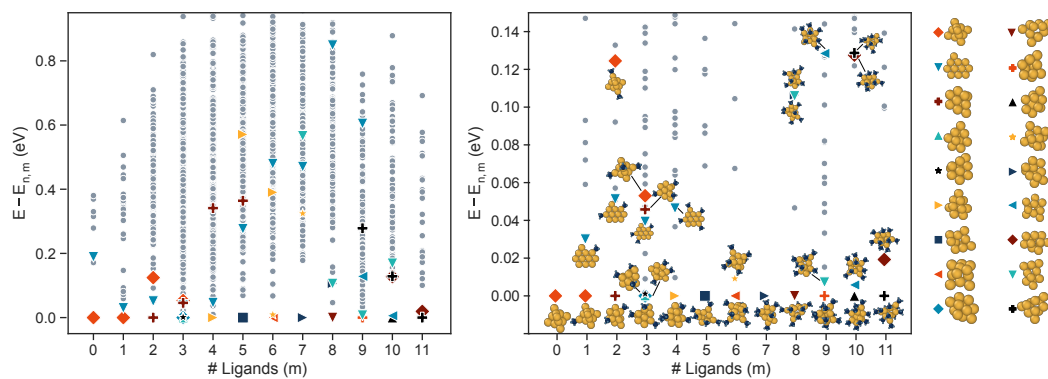


(b) n=4



(c) n=5

(d) $n=6$ (e) $n=7$ (f) $n=8$


 (g) $n=9$

 (h) $n=10$

 (i) $n=11$

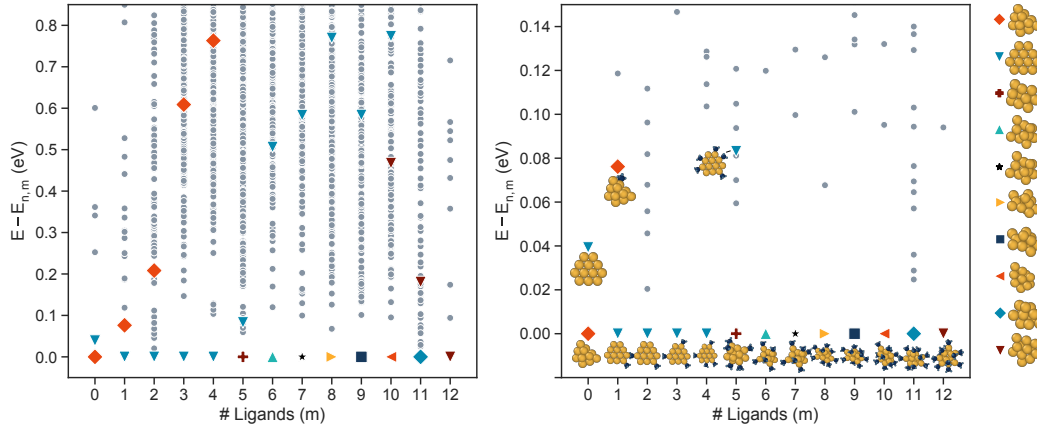
(j) $n=12$

Figure 3.4: Energies of $\text{Au}_n(\text{PH}_3)_m$ isomers for varying number of ligands, m . The energies are referenced to the minimum value for each m , $E_{n,m}$. Each point represents a unique gold kernel with the optimal ligand configuration for the given m ; relevant gold kernels are highlighted in order to demonstrate how relative energies change with ligation. Experimental structures from literature sourced from the CSD are denoted with black outlines and their CSD IDs. Note that equivalent gold kernels are defined as having the same gold-gold bonding with a bond length cutoff of 3.2\AA .

and is considered here (CSD IDs: 1106337,[96] 1106336[97]). It has 7 ligands ($m=7$) with a hexagonal base structure and a relatively high energy, ranking 55th (72 meV/Au) within the $\text{Au}_8(\text{PH}_3)_m$ structures. A lower chemical potential of phosphine, μ_{PH_3} , would lower the relative energy of the $\text{Au}_8(\text{PH}_3)_7$ experimental structure as it is not fully saturated with ligands. The Au_8 kernel that is the most stable in the bare system by 41 meV/Au can only accept 4 ligands before it breaks its 4-fold (square) symmetry or becomes highly energetically unfavorable.

n=9: Four different experimental $\text{Au}_9(\text{PH}_3)_8$ structures were used as references, each having one central unligated Au atom. They are ranked 33rd (43 meV/Au) with octahedral geometry (CSD ID: 1967410[98]), 51st (57 meV/Au) with ‘butterfly’ geometry (CSD IDs: 615444,[99] 687192,[100] 1273985[101]), 52nd (57 meV/Au) with ‘crown’ geometry (CSD IDs: 690419,[102] 690422,[103] 615445,[104] 690418[105]), and 84th (81 meV/Au) with ‘distorted crown’ geometry (CSD IDs: 1895800,[106] 1895797[107]) above the $\text{Au}_9(\text{PH}_3)_m$ hull, respectively. The ‘distorted crown’ experimental structure is likely high in energy with monodentate PH_3 ligands as it was synthesized with bidentate ligands.

Hidden Ground States

Many of the ligated structures exhibit gold kernels that are not local energy minima in the PES without ligation (*i.e.* there is no energy barrier between the geometry and a lower energy geometry). These structures are truly *hidden ground states*[108] such that they are dynamically unstable (*e.g.* a saddle point in the PES) in a pure gold system. An example of a hidden ground state identified here is the $\text{Au}_8(\text{PH}_3)_8$ structure. In the case of this cluster, ligands stabilize a more 3D structure, labelled in Fig. 3.5 as (a), which is *dynamically* unstable in its bare form and relaxes to a markedly different structure, labelled (b). Hence, the $\text{Au}_8(\text{PH}_3)_8$ ground state structure cannot be obtained by naive ligation of the bare ground state. Similarly, the ground state $\text{Au}_5(\text{PH}_3)_5$ manifests a 3D structure, but spontaneously relaxes into a 2D geometry when the ligands are removed. The presence of such hidden ground states is an indication that a gold cluster PES is significantly affected by ligation. Hence, a pool of unligated metastable structures is likely to miss potential synthesis products and neglecting the effect of ligation leads not only to a shift in the relative energies of different geometries but also to overlooking specific ground states entirely.

To explore the prevalence of hidden ground states, we examined the ground state structures - for all combinations of n atoms and m ligands - for metastability in their unligated state. From this analysis, 25 structures out of the 75 total ground states ($3 \leq n \leq 12$, $1 \leq m \leq n$) and 6 out of the 10 fully ligated structures ($n = m$) were found to be hidden ground states. The full list of hidden ground state structures is included in table 3.2.

Planar to Non-planar Transition

The size dependence of the planar to non-planar transition of gold clusters is relevant for predicting structure-function correlations. However, most of the work has focused on bare clusters in the gas phase [11–25] and predicts large planar to non-planar transition sizes, up to 13-14 Au atoms.[23, 24] Here we find that the 2D to 3D transition in ligated systems occurs much earlier, with the transition occurring between 4 to 5 gold atoms. This finding better represents the early transition size of 3 to 4 gold atoms observed experimentally. Tetrahedral Au_4 structures have been synthesized and characterized experimentally with bulky ligands: $[\text{Au}_4(\text{P}(\text{mesityl})_3)_4]^{2+}$ and $[\text{Au}_4(\text{P}(\text{tert-Bu})_3)_4]^{2+}$. [92, 93] We speculate that if more bulky ligands were used in this study, like PPh_3 , the size at which the transition occurs could be lowered further and recreate the experimental 2D to 3D transition size of 3 to 4 gold atoms. Fig. 3.6 quantifies the degree to which the relative energy between 2D and 3D structures changes with the addition of ligands. Structures are defined to be planar (2D) if the average squared distance of gold atom positions to an optimal fitting plane is less than 0.1 \AA . Positive values indicate that a 2D structure is preferred and negative values indicate that a 3D structure is preferred.

We find 3D structures to be preferable for ligated structures for two main reasons: sterics and s-d hybridization. Both effects will be discussed in the following sections.

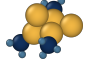
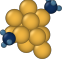
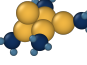
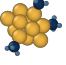
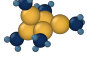
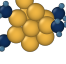
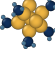

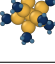

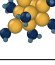
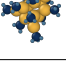
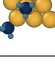

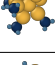
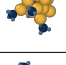
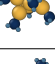

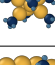
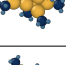

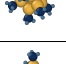
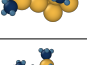
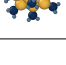

Au (n)	Ligands (m)	Unique ID	Image	Au (n)	Ligands (m)	Unique ID	Image
5	3	84		11	2	163	
5	4	109		11	3	407	
5	5	121		11	4	1039	
8	6	546		11	7	1953	
8	7	902		11	9	2317	
8	8	923		11	11	2554	
9	3	185		12	5	1345	
9	6	1212		12	6	1479	
9	7	1532		12	7	1831	
9	9	1832		12	9	2558	
10	3	249		12	10	2858	
10	4	640		12	12	3043	
10	10	2030					

Table 3.2: Hidden ground states. These structures are all ground states for different size combinations of n and m . When their ligands are removed and they are geometrically relaxed again with DFT, their bonding changes, indicating that the ligands change the potential energy surface of gold to have different local energy minima, which we call hidden ground states.

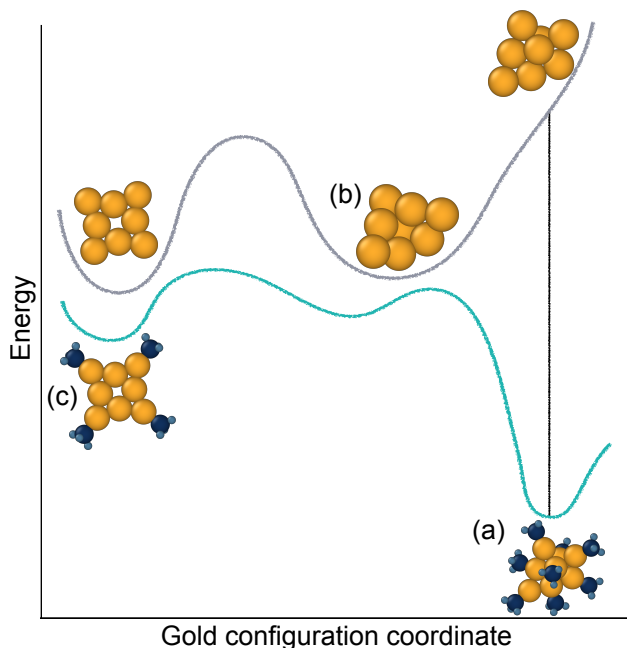


Figure 3.5: An illustration of the concept of hidden ground states, where the energy for bare gold and ligated gold are sketched as a function of a schematic gold configuration coordinate. Structure (a) is a hidden ground state as it is the most stable $\text{Au}_8(\text{PH}_3)_8$ structure in the dataset, but relaxes to structure (b) when its ligands are removed. Structure (c) is the most stable structure that can be achieved for the hollow square Au_8 kernel that is the most stable in the bare PES [72]

s-d Hybridization

Bare gold nanoclusters have been extensively investigated for the role of s-d hybridization in stabilizing planar configurations; While many argue that hybridization between the 5d and 6s orbitals is the key factor in stabilizing the planar gold structures,[109, 110] others have found that effects such as vdW interactions[21] and d-electron delocalization[111] are more important. Shafai *et al.* noted a shift in the d-band center in $\text{Au}_{13}(\text{PH}_3)_{12}$ to lower energies for more 3D geometries, as well as increased Au s-d overlap with the P p-orbitals in 3D structures, while planar structures exhibit both bonding and anti-bonding contributions.[71] Spivey *et al.* found that 3D geometries allow for better orbital mixing in $\text{Au}_{11}(\text{SCH}_3)_m$ of S p-orbitals and Au d-orbitals.[70]

Here we find a strong correlation between higher s-d hybridization and 2D configurations of gold, as suggested by literature, and exemplified in Fig. 3.7 for a representative cluster size of $n = 12$. We further examine how the s-d hybridization is affected by ligation. Figure 3.8 shows the trend in stabilization from s-d hybridization, H_{sd} (as calculated per Eq. 3.3

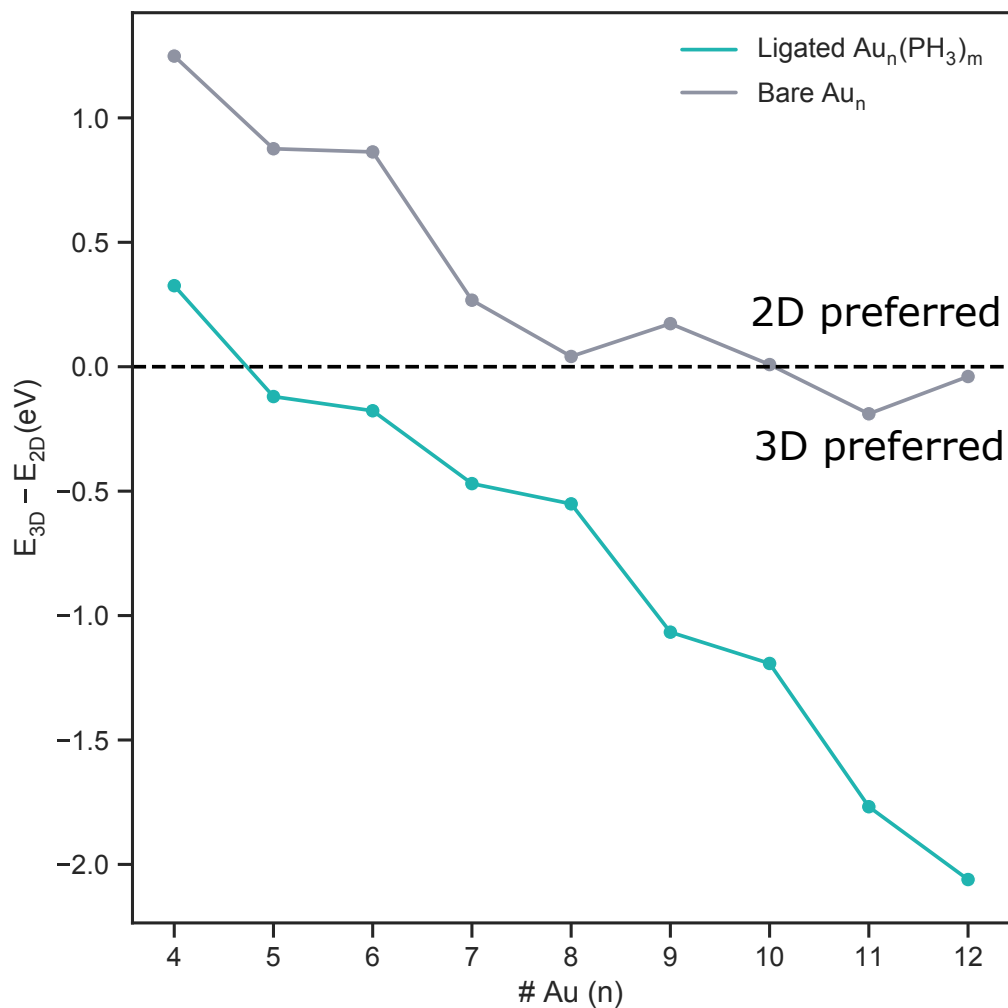


Figure 3.6: The energy difference($\Delta E = E_{3D} - E_{2D}$) between the most stable 2D and 3D clusters as a function of cluster size, as predicted with and without ligation.

in Section 3.5), as a function of ligation. As shown, there is a distinct increase in energy (destabilization) with respect to s-d hybridization, H_{sd} , as a function of ligation. Given that phosphine exhibits a weaker binding energy as compared to other widely-used ligands such as thiolates, these effects will likely be even more pronounced in systems with stronger binding energies.

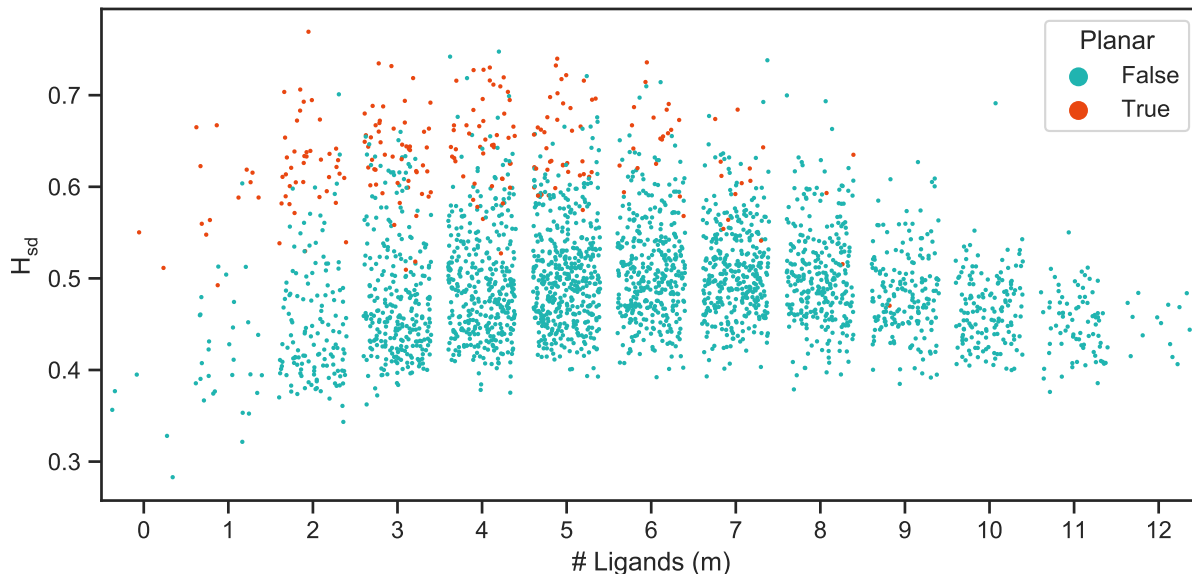


Figure 3.7: S-d hybridization is higher for planar structures. This is a representative example of the degree of hybridization in all planar and non-planar structures with $n=12$, results with other cluster sizes are similar.

Steric Effects

To analyze the local environment of the ligand binding sites and its impact on the cluster energy, we calculate the distances between neighboring ligands and evaluate the gold binding site topology. Analyzing the trends we observe two similar but distinct steric effects. First, the steric repulsion of ligands in close proximity favors structures where the ligands maximize their distance from each other. Extrapolating to bulkier ligands, such as PPh_3 , it is likely that these effects will be amplified due to the larger radius of steric interaction. Secondly, we find that corner sites are preferred over edges and faces (see Fig. 3.9). Comparing mono-ligated structures (*i.e.* $Au_n(PH_3)_1$), we classify the structures by ligand binding site (corner, or edge/face) by examining all bond angles between the binding gold atom and its neighboring gold atoms. Corner bonds are then defined as having Au-Au-Au (central Au is the binding Au) bond angles no greater than 140° . All structures with the same gold geometry were then compared according to their classifications. Indeed, corner-bound ligands were found to exhibit an average of 361 meV stronger binding energy than ligands bound to edges and faces of gold. Importantly, for larger sizes with saturated ligation, this preference for corners over edges lead initially planar structures to relax into 3D structures during geometry optimization in order to create more corner and edge sites.

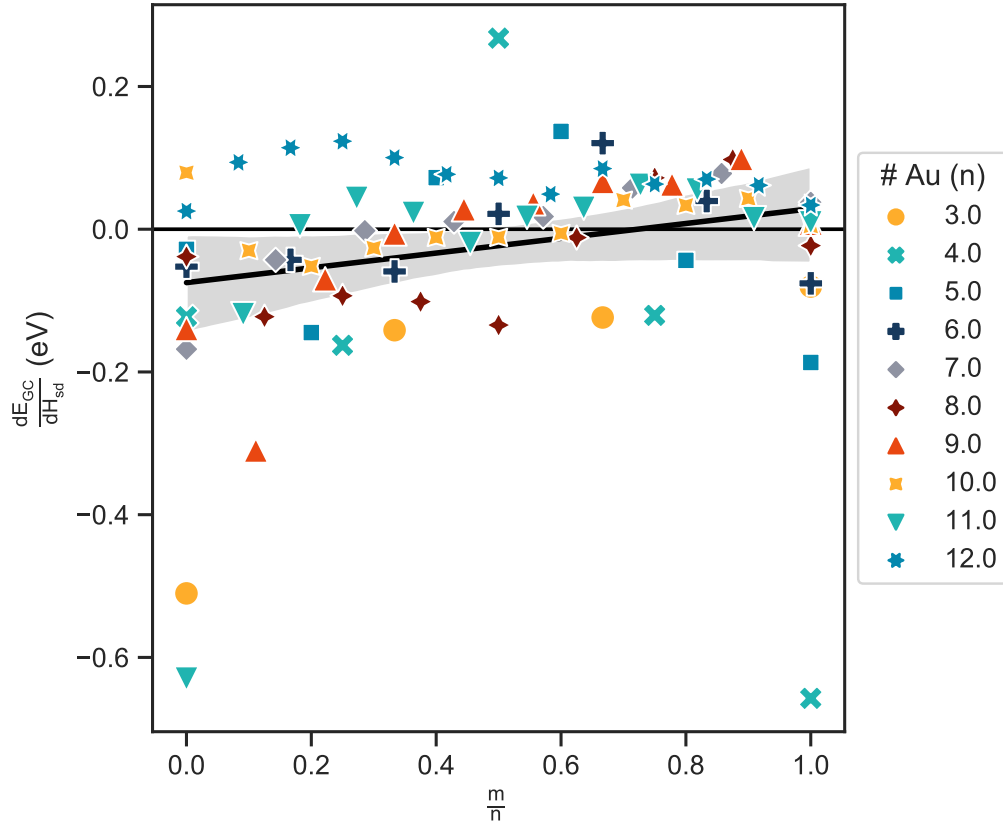


Figure 3.8: The derivative of grand canonical energies with respect to s-d hybridization index, $\frac{dE_{GC}}{dH_{sd}}$, for each set of cluster sizes, n and m . The positive trend line indicates that clusters are destabilized with greater s-d hybridization at higher ligand coverage (ratio of ligands to gold atoms, $\frac{m}{n}$). Note that clusters with n atoms and m ligands with 4 or fewer datapoints were not considered due to poor statistics. S-d hybridization is responsible for the stabilization of 2D structures in the bare gold system. 3D structures are more stable when ligated, possibly having to do with this trend in reduced stabilization from s-d hybridization with more ligands.

$\text{Au}_n(\text{PH}_3)_m$ Phase Diagram

To explore the phase space of most stable PH_3 -ligated Au clusters, we compute the grand canonical energy (Eq. 3.1) for a range of chemical potentials, μ_{Au} and μ_{PH_3} , reflecting the ability to control these parameters through the concentration of precursors in solution. Additionally, the ligand binding energy, E_{binding} , related to chemical potential according to Eq. 3.2 below, also correlates to the sterics and electron donating properties of the ligand

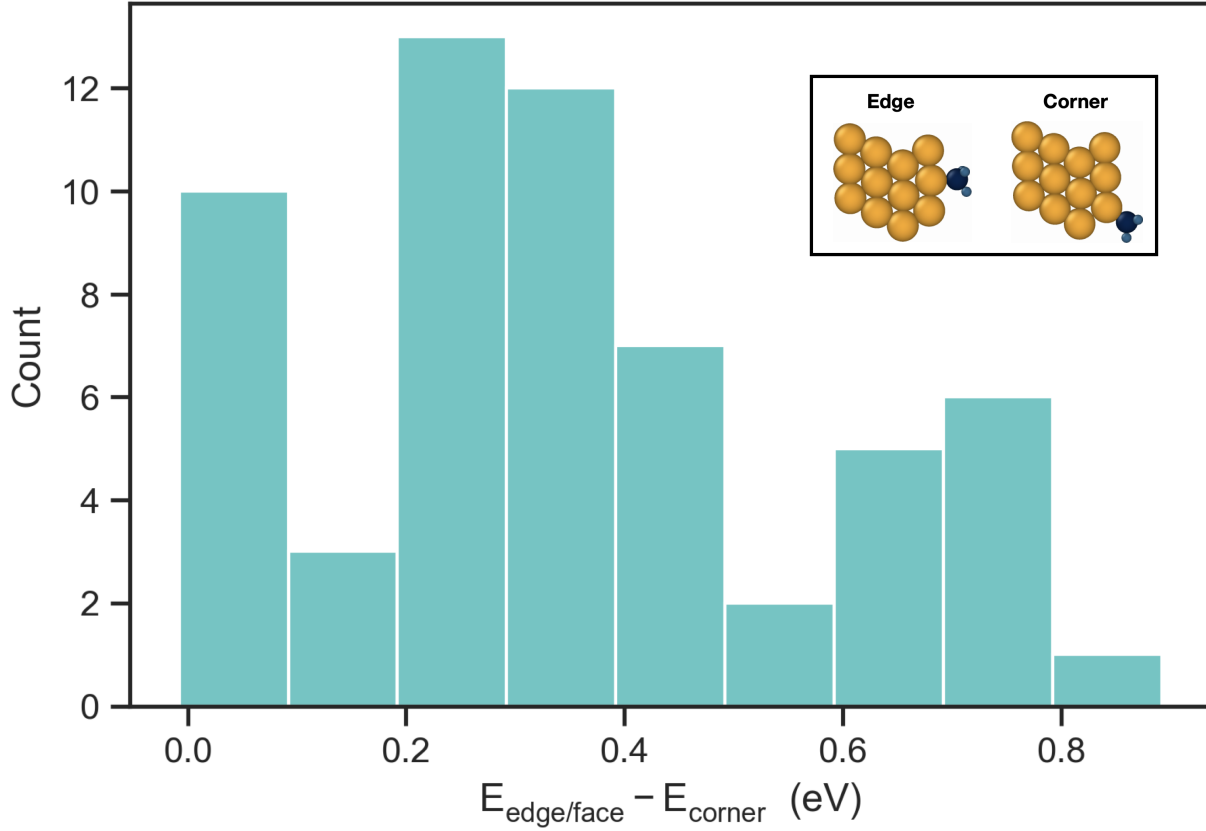


Figure 3.9: Binding energy preference to corners over edges and faces of gold. Corner binding sites are defined as having no gold-gold-gold angles greater than 140° .

and can thus be changed by utilizing different chemical species.[30]

$$E_{\text{binding}} = -\mu_{\text{PH}_3} + (E_{n,m+1} - E_{n,m}) \quad (3.2)$$

To estimate a synthesis yield based on relative energies, we assume that the structure population follows a Boltzmann distribution at 300K. The results are shown in Fig. 3.10, which prompts us to make the following observations. Changes between which structures are the most stable in the grand canonical ensemble only occur at very low chemical potentials of gold. The gold monomer and dimer occupy a large portion of the available phase space. However, at higher gold chemical potential, we find favorable conditions for small cluster formation, with a range of ligation as a function of phosphine chemical potential. At high phosphine chemical potential there is a strong stabilization of the largest, fully ligated cluster (here $\text{Au}_{12}(\text{PH}_3)_{12}$), indicative of crystallization. We note that $n=12$ is the limit of this dataset, and it is likely that larger sized clusters would successfully compete at these conditions.

A number of factors can influence the agreement between Fig. 3.10 and experimental outcomes, and we emphasize that our findings should be taken as trends within chemical potential space, rather than pinpointing absolute values. For example, careful benchmarking work has shown DFT to exhibit errors in estimating the Au_2 binding energy.[81] An equivalent construction of a phase diagram included in Fig. 3.11 shows the structures that might exist aside from the monomers and dimers.

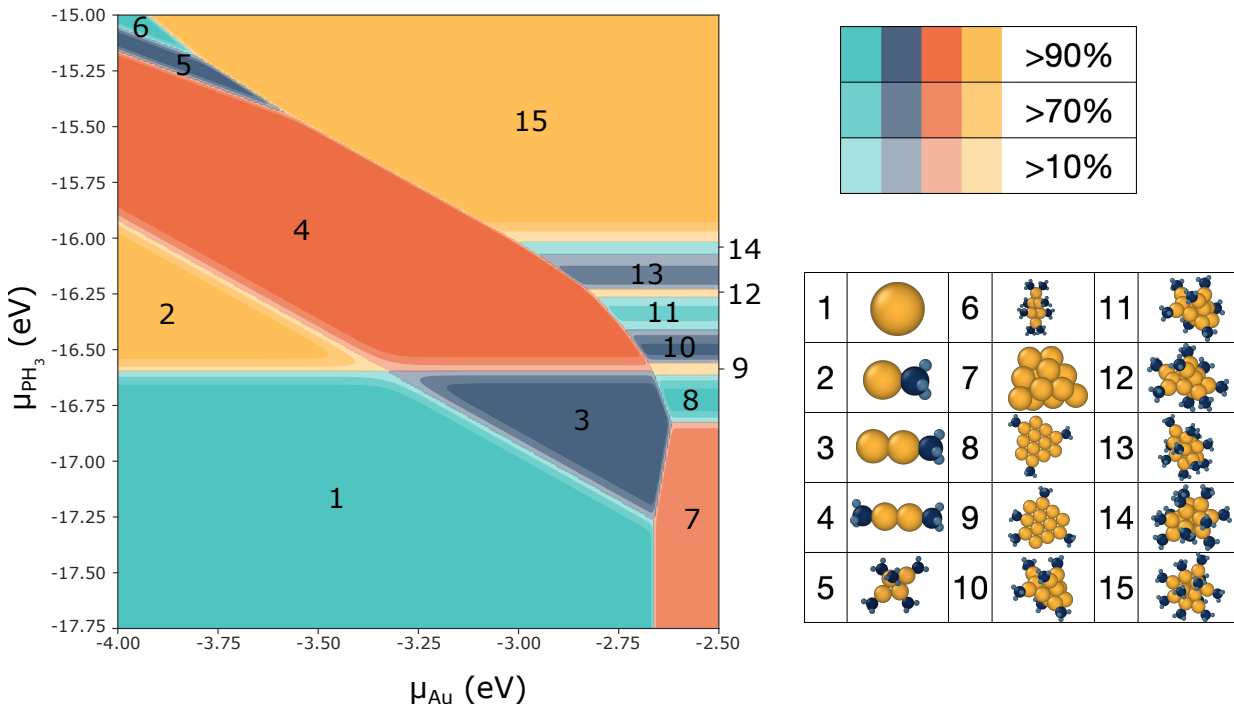


Figure 3.10: The $\text{Au}_n(\text{PH}_3)_m$ phase diagram was created by finding the most stable structure in the dataset for a range of chemical potentials. The stable species are shown on the right. The fraction of the solution product that they would expect to represent is calculated at 300K via Boltzmann population statistics.

Nanocluster Growth

During a solution synthesis reaction of gold NCs, gold is reduced from Au (I) or Au (III) precursors. Hence, the concentration and thus the chemical potential of Au (0) are expected to monotonically increase, providing a measure of relative reaction progress. As a result, one would expect transient intermediate-sized structures to participate in the growth process from one cluster size to another. At transition points, *i.e.* chemical potentials at which the grand canonical energies of two stable structures Au_{n1} and Au_{n2} are equal, the set of clusters of intermediate size Au_{nx} ($n1 < nx < n2$) then present unstable intermediates, or transition

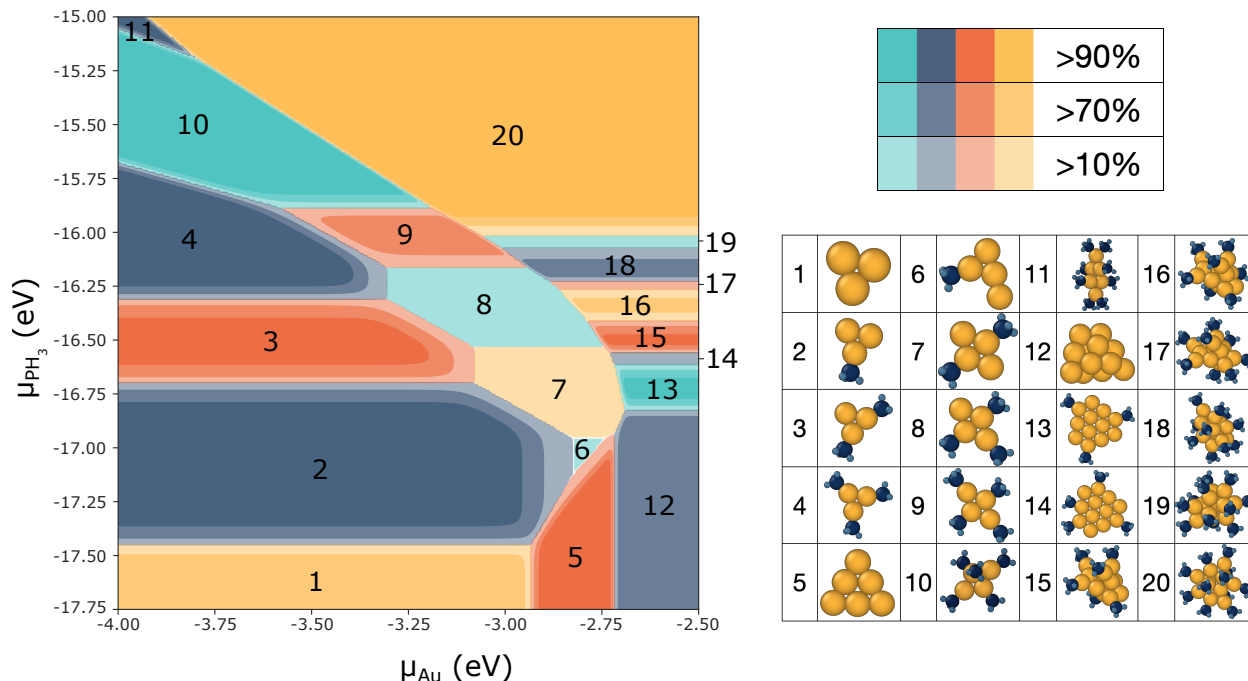


Figure 3.11: Phase diagram without considering monomer and dimers. The phase diagram was created by finding the most stable structure in the dataset (excluding the monomer and dimer) at that given chemical potential. The stable species are shown on the right. The fraction of the solution product that they would expect to have is calculated at 300K via a Boltzmann population.

state structures. We can propose a model nanocluster growth mechanism to illustrate this concept using the lowest energy structures as example intermediates. We note, however, that many other structures are likely accessible as intermediates due to their relatively small energy differences and to temperature and kinetic effects. An example sequence of potential metastable intermediate clusters for a phosphine chemical potential of -15.9 eV is included in Fig. 3.13. We note that one of the intermediates in this reaction pathway (size 7) has been successfully synthesized (CSD IDs: 668368,[88] 1123094,[89] 1123093,[90] 1123095[91]).

While including ligation significantly improves the qualitative agreement between observed and predicted clusters, there are a few remaining questions and discrepancies. For example, calculated intermediates with odd numbers of gold atoms are systematically predicted to be higher in energy than the even-sized structures. Different odd-even behavior has been computationally reported and we observe the same trend here (see Fig. 3.12) with even-sized structures being predicted to be more stable than odd-sized structures, [12, 14, 27, 112, 113] however this behavior is not supported by experimental evidence. We do, however, note that even- and odd-sized clusters synthesized experimentally all exhibit even and odd cationic charges, respectively (Table 3.3). Thus, using a neutral (even)

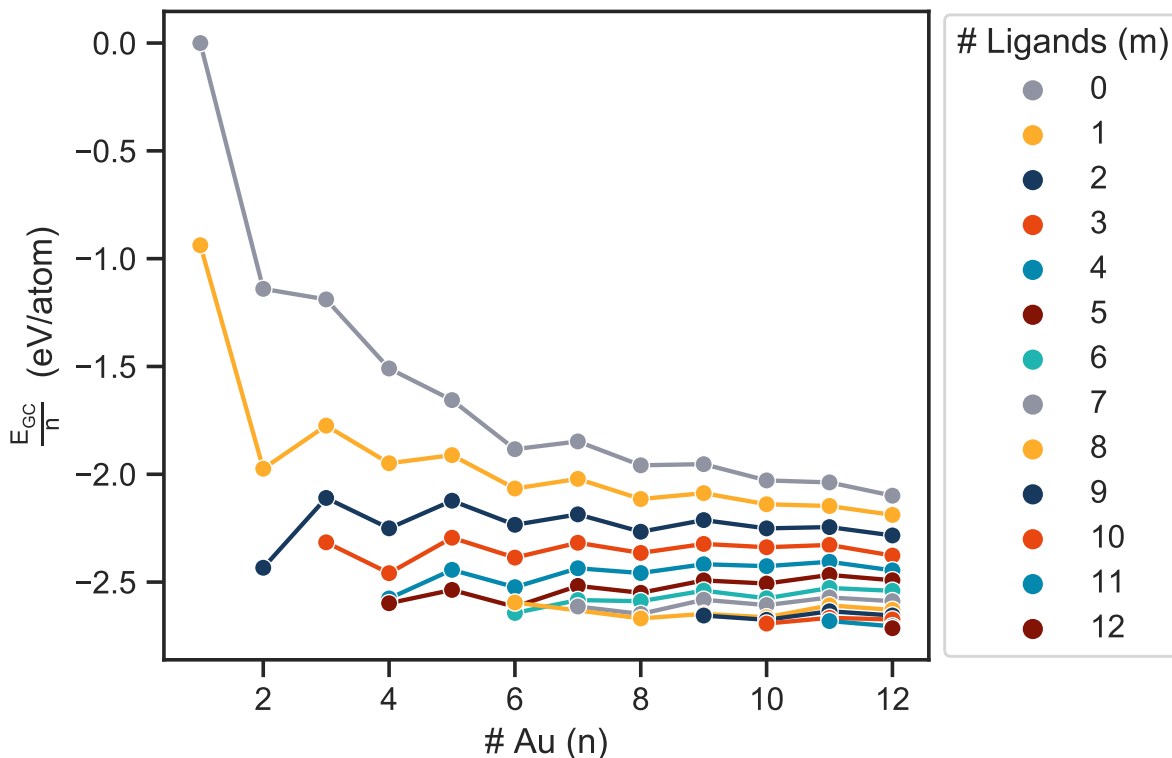


Figure 3.12: Grand canonical energy per atom of all the clusters, showing odd-even alternation in energies.

charge may preferentially favor even-sized clusters.

3.4 Conclusions

We generate and calculate - by a first-principles grand-canonical formalism - thousands of $\text{Au}_n(\text{PH}_3)_m$ nanocluster structures to compare and analyze stability-promoting chemistry-structural trends. We find that the addition of phosphine ligands dramatically changes the bonding and hybridization in gold NCs such that the planar to non-planar transition occurs between $n=4$ and $n=5$, earlier than predicted for the bare gold system and in improved agreement with experimental observations. The stabilization of 3D cluster geometries in the presence of ligation is rationalized by a combination of steric effects and s-d hybridization analysis. Furthermore, ligation stabilizes cluster geometries that are dynamically unstable in a pure gold system, resulting in a significant population of ‘hidden ground states’. These ground states manifest themselves in phase maps of cluster stability as a function of chemical potential, which lends insight into possible formation mechanisms. Our approach showcases

CSD ID	Au (n)	Ligands (m)	Charge (+)	Total e- count
1206655	4	4	2	10
1231463	4	4	2	10
1120743	6	6	2	16
1272194	6	6	2	16
2023935	7	6	1	18
668368	7	7	1	20
1123094	7	7	1	20
1123093	7	7	1	20
1123095	7	7	1	20
1106337	8	7	2	20
1106336	8	7	2	20
1895800	9	8	3	22
1895797	9	8	3	22
615444	9	8	3	22
687192	9	8	3	22
1273985	9	8	3	22
1967410	9	8	3	22
690419	9	8	3	22
690422	9	8	3	22
615445	9	8	3	22
690418	9	8	3	22

Table 3.3: The experimental structures that were used as references in this study and their total electron counts, with the assumption that each gold donates 1 electron and each phosphine donates 2 electrons to the superatom.

the necessity of including ligands in calculations of nanocluster energies, as well as the predictive power of utilizing high-throughput DFT methods to map out potential gold nanocluster products and their formation pathways.

Simplifications employed here that are likely to further influence the stability of Au NCs include the use of PH_3 instead of bulkier PR_3 groups, the absence of solvation effects and the neutral charge states. We expect that the treatment of charge will reduce the odd/even energetic disparity and that the increased steric repulsion of bulkier ligands will promote more compact clusters. Calculating the effect of steric bulk, charge and solvation increases the computational demand beyond current capabilities for high-throughput electronic structure computation, and hybrid machine-learning models may be required for efficiently exploring this high-dimensional combinatorial chemical space. Future inclusion of these effects as well as increased cluster size is anticipated to guide practitioners to different experimental

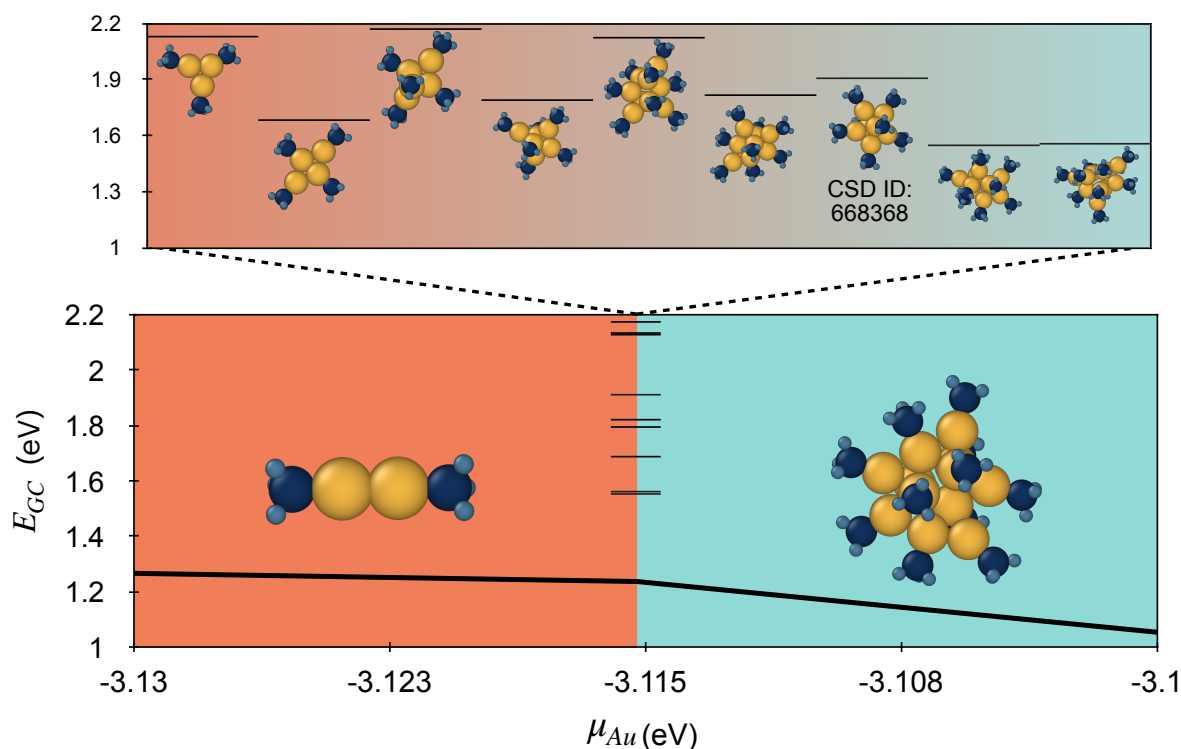


Figure 3.13: Possible transient intermediates in the transition between a small stable structure to a large stable structure. Assuming an increasing μ_{Au} and constant μ_{PH_3} , set here to be -15.9 eV, the Au_{12} structure (right) would become more stable than the dimer (left), and some transient intermediate species (examples included in the inset) would be expected to exist in the growth process.

conditions and suggest formation mechanisms that can be empirically tested.

3.5 Methods/Experimental

Ligation Algorithm

A database of phosphine-ligated nanoclusters is generated from an initial set of bare structures as outlined below and illustrated in Fig. 3.14. The algorithm is divided into steps i)-v) as follows (the same numbers are used in Fig. 3.14).

i) **Initial structures.** A group of previously predicted low energy bare gold clusters is defined from the Quantum Cluster Database.[24] 81 structures between 3 to 12 atoms with low energies are taken as the initial set of gold cluster geometries.

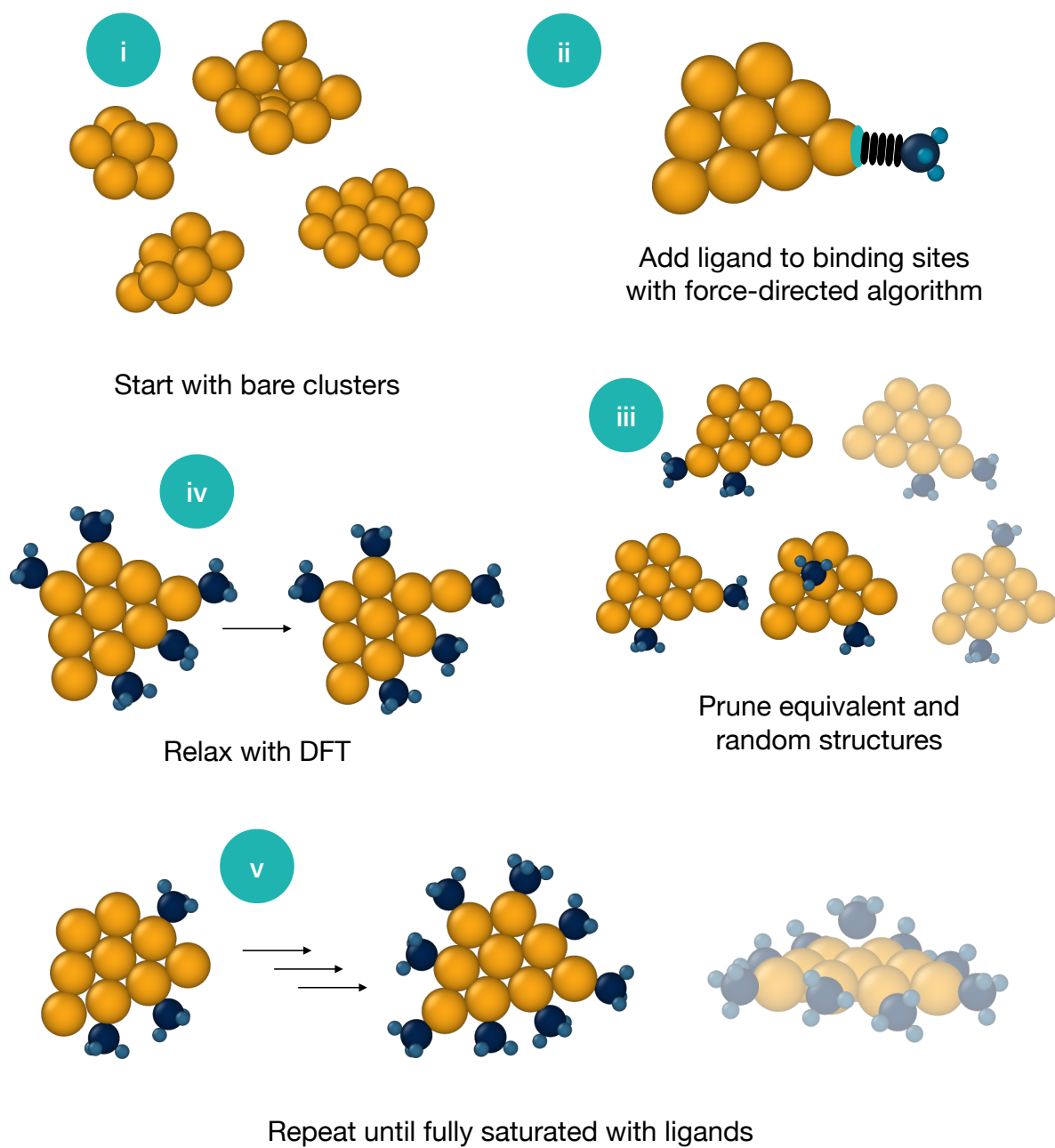


Figure 3.14: Ligation Algorithm. Additional ligated clusters were generated by adding PH_3 successively onto bare gold clusters.

ii) **Addition of ligands.** A structure with an additional PH_3 ligand is created for each possible ligand binding site. Binding sites are identified as gold atoms on the surfaces of the clusters that do not already have a bond to a PH_3 ligand. Reasonable guesses for optimal ligand placements are made with a Fruchterman-Reingold force-directed algorithm, implemented by the *networkx* code, which treats the created bond between the Au and P as a spring and then adds electrostatic repulsion so that the new ligand is positioned away from the cluster.

iii) **Pruning.** Each structure is compared to all others in the set and any duplicate or symmetrically equivalent structures are removed. Structures are defined as duplicates if they have isomorphic bonding (Au-Au and Au-P bond cutoffs of 3.2 and 2.5 Å, respectively). In order to manage the combinatorial explosion of possible partially-ligated structures, a random fraction of structures with duplicate gold kernels were removed under the assumption that those remaining constituted a sufficient sampling of possible partially-ligated structures. To show an example as to why the structures required further pruning, we calculate the possible structures generated through the $\text{Au}_{12}(\text{PH}_3)_m$ ligation. Each gold kernel could be ligated in $12!$ different ways. By subtracting all symmetry-equivalent ligation, this number could be reduced to about 4000 per single gold kernel. Given that the relaxation of gold kernels to different geometries generated approximately 400 distinct Au_{12} kernels, a full combinatorial evaluation would still require computation of about 1.5 million structures. Randomly discarding a fraction of the structures at each step reduced the number of structures calculated to a more manageable 3213 Au_{12} structures. The fraction of pruned structures correlated with the structure size and number of combinations of ligand configurations; As many as 90% of the largest structures ($n=12$) with half ligation ($m=6$) were pruned, while none of the smaller ($n < 8$) or fully ligated ($n=m$) structures were pruned.

iv) **Relaxation.** The structures are geometrically relaxed with DFT.

v) **Repeat and terminate.** Steps ii)-iv) are repeated until the structures are fully saturated with ligands. Over-saturation is achieved when the last ligand does not bind to the cluster (Au-P distance $> 2.5\text{\AA}$), and such structures are excluded in the final set. At this point, the algorithm terminates. We note that the outlined sequential procedure - which adds one ligand at a time and relaxes that cluster - does not target highly symmetric ligated structures.

Computational Methods and Details

The structures of $\text{Au}_n(\text{PH}_3)_m$ are geometrically relaxed with density functional theory (DFT). Additionally, 50 phosphine-stabilized gold structures from the Cambridge Structural Database (CSD) were computed with PH_3 in place of their organophosphine (PR_3) ligands. 21 of those (10 different structures) maintained the same structures and gold bonding (Au-Au bond cutoff of 3.2 Å) during DFT geometry optimization and were taken as a set of reference experimental structures.

Spin-polarized calculations were performed with a plane wave basis set, as implemented in the Vienna Ab-initio Simulation Package (VASP).[114] A cutoff energy of 520eV was

applied for the plane wave basis set and the electron-ion interactions were described by the projector augmented wave (PAW) method.[115] The exchange and correlation energies were calculated using the Perdew-Burke-Ernzerhof (PBE) form of the generalized gradient approximation (GGA).[116] The structures were provided at least 10Å of vacuum along each direction to reduce self-interaction between periodic images. [117, 118] One k point, *i.e.*, the γ point, was used in the cluster calculations and Gaussian smearing was applied with a width of 0.2 eV. Spin orbit coupling was not considered given its computational cost and contradicting conclusions regarding its effect on the relative stability of bare Au clusters.[10, 14] A post-relaxation dispersion energy correction with zero damping (D3) was then applied. [119]

The s-d hybridization, H_{sd} , is calculated according to the method described in literature and reproduced in Eq. 3.3,[21, 120] where variable I represents the atom index, S represents the spin state, W_E represents the occupation of the eigenvalue E, and m represents the index of d-orbitals. w_s and w_d are the weights of the projected wavefunction on the spherical harmonics within the Wigner-Seitz atomic radius around each atom;

$$H_{sd} = \sum_{I,S} \sum_E W_E^2 \sum_m w_s^{I,S,E} w_{d,m}^{I,S,E} \quad (3.3)$$

where only contributions from the orbitals of gold atoms were considered. An example graph of the DOS for a bare gold and ligated structure decomposed into s and d states is included in Fig. 3.15.

3.6 Data

The phosphine-stabilized gold structures are all publicly accessible on MPContribs at the following link <https://contribs.materialsproject.org/projects/auph3>

3.7 Supporting Information

Distribution of structures in the dataset, density of states with and without ligation, s-d hybridization calculations for planar vs. non-planar structures, binding energies to corners vs. edges/faces of clusters, a detailed phase diagram for the gold size range of n=3-12, detailed relative energy diagrams with low energy structure renderings, and a table of ligand binding energies, a table of hidden ground states discovered as a result of this study, and a table of experimental reference structures with their electron counts.

3.8 Associated Content

Caitlin A. McCandler; Jakob C. Dahl; Kristin A. Persson; Phosphine-stabilized hidden ground states in gold clusters investigated via a $\text{Au}_n(\text{PH}_3)_m$ database. 2022. ChemRxiv. 10.26434/chemrxiv-2022-q1hj2 (accessed July 21, 2022).

3.9 Acknowledgements

C.A.M. acknowledges useful discussions with J. Dagdalen, M. Horton and R. Kingsbury. C.A.M., J.C.D., and K.A.P. thank the U.S. Department of Energy, Office of Science, Office of Basic Energy Sciences, Materials Sciences and Engineering Division, for their support under Contract No. DE-AC02-05-CH11231 within the Data Science for Data-Driven Synthesis Science grant (KCD2S2). This research used resources of the National Energy Research Scientific Computing Center, a DOE Office of Science User Facility supported by the Office of Science of the U.S. Department of Energy under Contract No. DE-AC02-05CH11231 using NERSC award BES-ERCAP0020531 and award BES-ERCAP0013481. C.A.M. gratefully acknowledges the National Defense Science and Engineering Graduate (NDSEG) fellowship for financial support. J.C.D. acknowledges support by the National Science Foundation Graduate Research Fellowship under DGE 1752814 and by the Kavli NanoScience Institute, University of California, Berkeley through the Philomathia Graduate Student Fellowship.

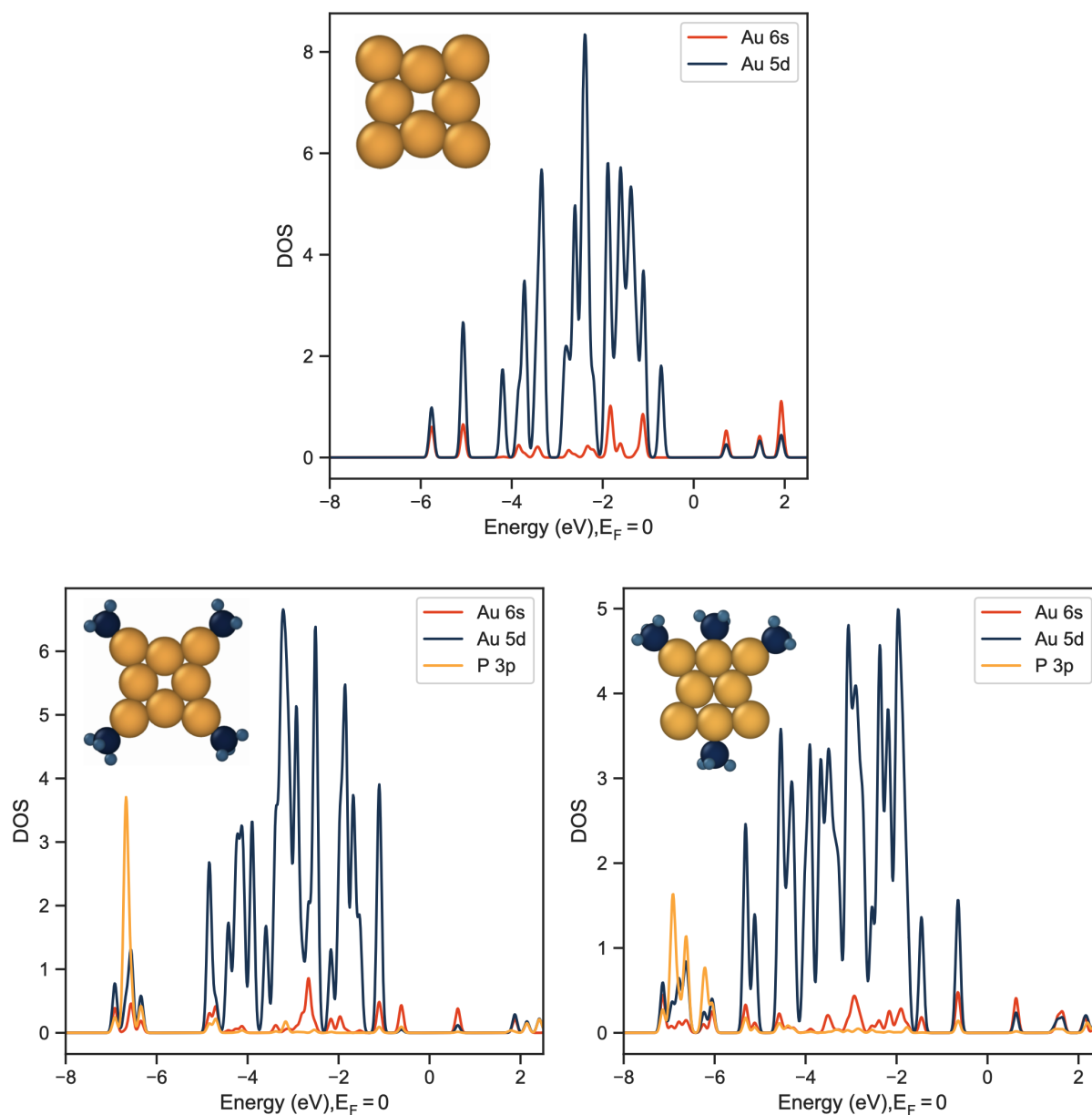


Figure 3.15: Density of states (DOS) of representative examples of a (left) bare gold cluster, and (middle, right) phosphine-stabilized gold clusters. The middle structure has an energy of -84.47 eV and the right structure has an energy of -83.73 eV. Only s and d orbitals from Au atoms and p orbitals from P atoms are included in the DOS. The DOS were smeared with Gaussian broadening of 0.1 eV applied around the discrete electronic energy levels for easier visualization. The DOS for the bare structure on the left matches results obtained in other studies[111, 121].

Chapter 4

Gold Nanocluster Dynamic Simulations

Reproduced in part with permission from “McCandler, C. A., Pihlajamäki A, Malola S, Häkkinen H, Persson K. Gold-Thiolate Nanocluster Dynamics and Intercluster Reactions Enabled by a Machine Learned Interatomic Potential. ACS nano. Accepted” Copyright 2024 The Authors.

Abstract

Mono-layer protected metal clusters comprise a rich class of molecular systems, and are promising candidate materials for a variety of applications. While a growing number of protected nanoclusters have been synthesized and characterized in crystalline forms, their dynamical behavior in solution, including pre-nucleation cluster formation, is not well understood due to limitations both in characterization and first-principles modeling techniques. Recent advancements in machine-learned interatomic potentials are rapidly enabling the study of complex interactions such as dynamical behavior and reactivity at the nanoscale. Here, we develop an Au-S-C-H Atomic Cluster Expansion (ACE) interatomic potential for efficient and accurate molecular dynamics simulations of thiolate-protected gold nanoclusters ($\text{Au}_n(\text{SCH}_3)_m$). Trained on more than 30,000 density functional theory calculations of gold nanoclusters, the interatomic potential exhibits *ab initio* level accuracy in energies and forces, and replicates nanocluster dynamics including thermal vibration and chiral inversion. Long dynamics simulations (up to 0.1 μs time scale) reveal a novel mechanism explaining the thermal instability of neutral $\text{Au}_{25}(\text{SR})_{18}$ clusters. Specifically, we observe multiple stages of isomerization of the $\text{Au}_{25}(\text{SR})_{18}$ cluster, including a novel chiral isomer. Additionally we simulate coalescence of two $\text{Au}_{25}(\text{SR})_{18}$ clusters and observe series of new clusters where the formation mechanisms are critically mediated by ligand exchange in the form of $[\text{Au}-\text{S}]_n$ rings.

4.1 Introduction

Protected nanoclusters—small atomically precise nanoparticles stabilized by organic ligands—are promising materials for catalysis, optics, and biological sensing.[122–126] Tailoring their properties necessitates not only establishing structure-property relationships but also guiding synthesis towards narrowly disperse solutions of specific sizes and morphologies. However, while many thiolate-protected nanoclusters have been synthesized and crystallized, the temporal and spatial resolution of the current best characterization techniques limit the ability to image synthesis over time or to observe the dynamic solution-exchange events that contribute to processes such as coalescence. Similarly, *ab initio* molecular dynamics (AIMD) simulations are limited to sub-nanosecond time periods due to computational cost.

Recent developments in interatomic potential architectures and computational packages show promising results for increased system size and time scale of atomic simulations while maintaining density functional theory (DFT) level accuracy.[127–131] In this work, the Atomic Cluster Expansion (ACE) interatomic potential formalism was selected due to its speed, accuracy, and ability to extrapolate atomic-level interactions.[54, 58] ACE potentials predict energies and atomic forces from a sum of the atomic interactions present in the structure, including multi-body interactions, while also considering the symmetries of atomic interactions to reduce the total number of functions required to represent the system. The overall computational scaling is therefore linear with respect to the system size, and as such, the evaluation speeds rival those of classical potentials while enabling bond breaking and formation, a feat not viable for classical force fields. Furthermore, in comparison to previously fitted interatomic potentials, specifically for gold thiolate clusters,[132–136] ACE potentials are well positioned to produce accurate dynamical behavior as each atom is only classified by its element and position, with no bonding enforced between atoms or sub-classifications specifying if the atom is a member of the ligand shell or the cluster core. Importantly, exchange between core and ligand gold constituents is possible.

Trained on more than 30,000 DFT calculations of gold nanoclusters, the Au-S-C-H ACE potential successfully reproduces *ab initio* level structure-energy properties of nanoclusters with a variety of atomic packings of the gold core (icosahedral, decahedral, FCC, etc.) and with sizes up to 144 Au atoms. By limiting the cases to neutral thiolated (SCH₃) clusters in vacuum environments, the potential shows remarkable applicability due to its accuracy, force prediction, speed, and facilitating bond making and breaking. This development allows us to probe long-timescale dynamical events that are beyond reach of DFT methods. In particular, long finite-temperature simulations of Au₂₅(SCH₃)₁₈, up to 0.1 μ s time scale, evidence a transformation from the ground state structure into several unique Au₂₅(SCH₃)₁₈ structural isomers. Chirality, a property not previously predicted be possible in the Au₂₅(SCH₃)₁₈ system, is observed to be accessible through reversible low-energy transformation pathways. Furthermore, simulations of agglomeration and coalescence of two Au₂₅(SCH₃)₁₈ clusters reveal the importance of higher-energy reactive isomers as key intermediates in initiating coalescence. Finally, gold-thiolate rings are found to facilitate size and shape equilibration of the reaction products, as well as atom exchange between clusters.

4.2 Validation of the Potential: Structural, Vibrational and Dynamical Properties

A high degree of accuracy is required to obtain reliable dynamical behavior. We compare a range of properties obtained for known thiolate protected nanoclusters using the ACE potential against *ab initio* predicted energies, forces, vibrational modes, and transition state barriers to benchmark the capabilities of the potential in a range of different aspects.

Structure-Energy Landscape

As described in the Methods Section, the training and testing data comprise a collection of molecular dynamics trajectories of Au_{38} isomers obtained from previous studies, as well as clusters with a variety of sizes sampled with the active learning process. In summary, 31,942 structures were used for training and 11,702 structures were used for testing. The root mean squared error (RMSE) for the testing and training datasets are 2.27 meV/atom and 11.0 meV/atom respectively (Figure 4.1A). The testing error is lower than the training error likely due to the fact that the testing data consist of structures generated using AIMD, while the training data include some structures that deviate from equilibrium geometries, hence the standard deviations of testing and training data are 34 meV/atom and 56 meV/atom respectively (See Methods: *ab initio* training data). A previously fitted Extreme Minimal Learning Machine (EMLM) model achieved a RMSE of 16.9 meV/atom for the same test set.[135] The RMSE of the forces for the testing and training dataset 121.1 meV/Å and 87.83 meV/Å respectively, which corresponds to 14% and 22% error in the respective forces.

We further test the ability of the ACE potential to reproduce the DFT geometries and energies of known neutral gold thiolate nanoclusters, sourced from single crystal X-ray diffraction (XRD) coordinates reported in literature, with their thiol ligands (SR) replaced with methanethiol (SCH_3) (Table 4.1). [137–153] Each of these reference clusters were separately relaxed with DFT and with the ACE potential. We note that there will always be slight distortions between the XRD coordinates and those predicted by DFT, especially given that the bulky SR groups are replaced here by SCH_3 . The deviation between the relaxed geometries with the two methods are calculated by their root mean square displacements (RMSD) of the Au, S and C atoms calculated with the Kabsch-Umeyama algorithm implemented in *pymatgen* (Figure 4.1C).[155] Thiolate-protected gold nanocluster cores can adopt a variety of atom packing types, and most commonly adopt face centered cubic (FCC) or icosahedral geometries. The training structures, $\text{Au}_{38\text{T}}$ and $\text{Au}_{38\text{Q}}$, have icosahedral centers, as does Au_{25} and Au_{144} (except for the central gold atom). Many of the structures considered here exhibit FCC cluster cores, including Au_{21} , $\text{Au}_{28\text{A}}$, $\text{Au}_{28\text{B}}$, Au_{36} , Au_{40} , $\text{Au}_{42\text{A}}$, Au_{44} , Au_{52} , and Au_{92} , and even decahedral cores, including Au_{102} . The other clusters have structures that are difficult to define by their packing type. Au_{36} , which presents a FCC core, showed the least agreement between ACE and DFT, with a RMSD of 0.32, and its DFT predicted structure is shown in contrast to its ACE predicted structure in Figure 4.1C. The structure

Table 4.1: Comparison of relaxed structure energies of known neutral gold thiolate nanoclusters from the literature. [137–153] The thiol ligands in the reported crystal structures of each nanocluster are here replaced with methanethiol (SCH_3) and their geometries are relaxed with a structural optimization, either using DFT or ACE as the calculator. The ACE energy of the DFT-relaxed structure was compared to the DFT energy of the DFT-relaxed structure (DFT optimized error) and the ACE energy of the ACE-relaxed structure was compared to the DFT energy of the DFT-relaxed structure (ACE optimized error). The training examples mainly consist of simulated data from $\text{Au}_{38\text{T}}$ and $\text{Au}_{38\text{Q}}$, and as such, the prediction errors for those clusters are relatively low. The potential can represent nanoclusters with a wide variety of gold core structures and sizes apart from the Au_{38} clusters, however with slightly higher expected error.

Name	Ref.	Formula	Methylated Formula	Cohesive Energy Prediction Error (meV/atom)	
				DFT Optimized	ACE Optimized
Au_{18}	[137, 154]	$\text{Au}_{18}(\text{SC}_6\text{H}_{11})_{14}$	$\text{Au}_{18}(\text{SCH}_3)_{14}$	-2.0	-3.7
Au_{21}	[138]	$\text{Au}_{21}(\text{S}^t\text{Bu})_{15}$	$\text{Au}_{21}(\text{SCH}_3)_{15}$	-0.2	-2.7
Au_{24}	[139]	$\text{Au}_{24}(\text{SCH}_2\text{Ph}^t\text{Bu})_{20}$	$\text{Au}_{24}(\text{SCH}_3)_{20}$	-10.1	-13.8
$\text{Au}_{25\text{A}}$	[140]	$\text{Au}_{25}(\text{PET})_{18}$	$\text{Au}_{25}(\text{SCH}_3)_{18}$	-6.4	-8.0
Au_{28}	[141]	$\text{Au}_{28}(\text{SC}_6\text{H}_{11})_{20}$	$\text{Au}_{28}(\text{SCH}_3)_{20}$	1.5	-0.2
Au_{36}	[142]	$\text{Au}_{36}(\text{SPh})_{24}$	$\text{Au}_{36}(\text{SCH}_3)_{24}$	5.5	-0.3
$\text{Au}_{38\text{Q}}$	[143]	$\text{Au}_{38}(\text{PET})_{24}$	$\text{Au}_{38}(\text{SCH}_3)_{24}$	-0.4	-2.1
$\text{Au}_{38\text{T}}$	[144]	$\text{Au}_{38}(\text{PET})_{24}$	$\text{Au}_{38}(\text{SCH}_3)_{24}$	0.1	-2.0
Au_{40}	[145]	$\text{Au}_{40}(\text{o-MBT})_{24}$	$\text{Au}_{40}(\text{SCH}_3)_{24}$	6.9	3.7
$\text{Au}_{42\text{A}}$	[146]	$\text{Au}_{42}(\text{TBBT})_{26}$	$\text{Au}_{42}(\text{SCH}_3)_{26}$	2.4	-2.6
$\text{Au}_{42\text{B}}$	[147]	$\text{Au}_{42}(\text{TBBT})_{26}$	$\text{Au}_{42}(\text{SCH}_3)_{26}$	3.5	1.5
Au_{44}	[148]	$\text{Au}_{44}(\text{TBBT})_{28}$	$\text{Au}_{44}(\text{SCH}_3)_{28}$	7.2	2.4
Au_{52}	[149]	$\text{Au}_{52}(\text{PET})_{32}$	$\text{Au}_{52}(\text{SCH}_3)_{32}$	7.9	4.1
Au_{92}	[150]	$\text{Au}_{92}(\text{TBBT})_{44}$	$\text{Au}_{92}(\text{SCH}_3)_{44}$	10.1	6.3
Au_{102}	[151, 153]	$\text{Au}_{102}(\text{p-MBA})_{44}$	$\text{Au}_{102}(\text{SCH}_3)_{44}$	4.6	2.1
Au_{144}	[152]	$\text{Au}_{144}(\text{SCH}_2\text{Ph})_{60}$	$\text{Au}_{144}(\text{SCH}_3)_{60}$	8.1	6.9

PET=phenylethanethiolate, TBBT=4-*tert*-butylbenzenethiolate, o-MBT=2-methylbenzenethiolate, p-MBA=*para*-mercaptopbenzoic acid

differences are difficult to identify by eye, indicating that the deviation even in the worst case is low. Performing the structural optimization with the ACE potential therefore yields similar results to performing the structural optimization with DFT, at a fraction of the computational cost.

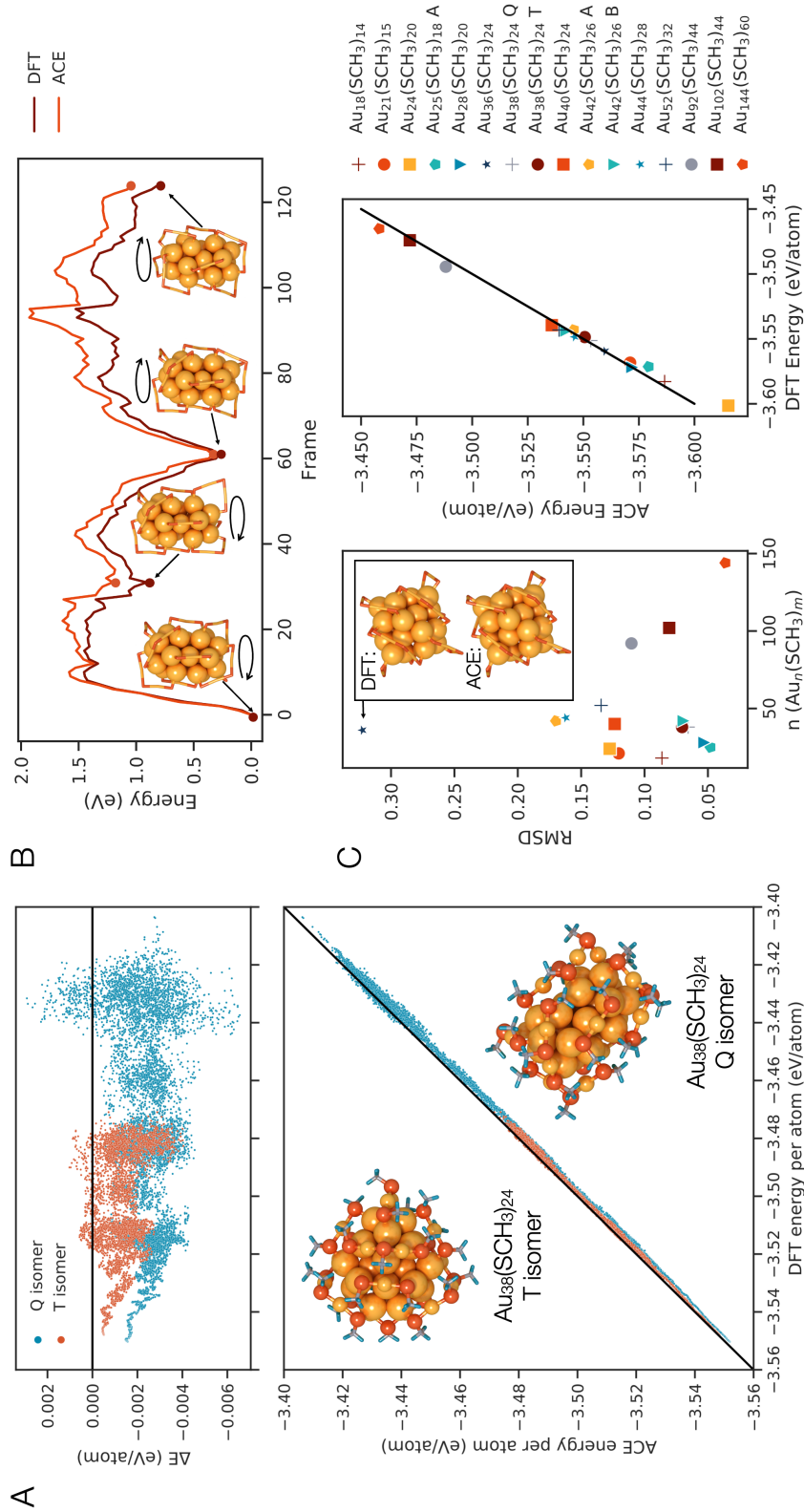


Figure 4.1: A. Testing data parity plot, The AIMD test runs are for Au_{38}T up to 500K (4049 steps) and for Au_{38}Q up to 800K (7653 total steps). B. Chiral transition state energies for the twisting of the isomer. C. Crystal structures of known nanoclusters relaxed in the ACE potential have comparable (Left) RMSD and (Right) predicted energies with respect to those relaxed with DFT.

Transition States

One of the most difficult regions to map in the potential energy surface (PES) of any structure is the transition state, or saddle point, along the trajectory between two metastable structures, or PES local energy minima. As the majority of training data lies within potential energy wells, extrapolations must be made to predict the height of the saddle point separating energy minima. Here, we assess the accuracy of the potential in predicting the energies over a transition between the chiral enantiomers of the Au₃₈Q isomer, with DFT reference energies at each step of the transformation (Figure 4.1B). The trace of the curve has the same characteristic peaks and valleys, albeit with a positive overall shift in the predicted energies. We hypothesize that the energy scaling issue is likely due to the fact that the potential prioritizes learning the forces as opposed to the energies (see Methods section) which will retain the shape of the curve as compared to the DFT calculated one, with a deviation in the true energy.

Vibrations

Vibrational densities of states (VDOS) of the gold-thiolate clusters are recreated with the ACE potential as compared with AIMD. The atom-resolved VDOS calculated for Au₃₈Q with each simulation method are included in Figure 4.2A. Note that the AIMD simulations use deuterium instead of hydrogen, and as such the vibrational modes that include hydrogen or deuterium are not the same, but do match experimentally determined values for similar molecules, like methane and methane-d₄. The methane (CH₄) stretching vibrations exist at 2917 and 3019 cm⁻¹, and the bending/rocking modes exist at 1306 and 1534 cm⁻¹, while the methane-d₄ (CD₄) stretching vibrational modes exist at 2109 and 2259 cm⁻¹, and the bending/rocking modes exist at 996 and 1092 cm⁻¹.^[156] The heavier deuterium also likely reduces the frequency of the methyl torsional modes at low frequencies. The vibrational density of states in the gold-sulfur core, however, are unaffected by the deuterium and exhibit the same shape as seen in AIMD simulations. The vibrational modes were labeled by comparing these peaks to those observed in computational simulations of other small gold-thiolate nanoclusters.^[157] Visual inspection of the shape of the vibrational peaks for the cluster core confirm the similarity with those calculated for the Au₂₅ cluster. ^[158] An important feature to encode is the Au-S bonding since the ligand shell behavior depends strongly on the Au participation in the ligand ‘staple’ motif and indeed, may adopt a charge of Au(I).

Figure 4.2B compares the distributions of Au-S bond lengths, Au-S-Au bond angles, and S-Au-S angles from AIMD simulations (2 fs/step, Berendsen dynamics) and ACE simulations (1 fs/step, Langevin dynamics) of the Au₃₈Q structure. Although varying timestep lengths are implemented to address instabilities when using very long timesteps with the ACE potential, equivalent time frames are sampled to ensure that structures are at comparable stages of deviation from the ideal geometry. The concluding segments of each simulation are utilized to ensure that the temperature reaches equilibrium. In the 300K and 500K simulations, 1500

steps are skipped and the final 500 steps are used, and in the 800K simulation, 3000 steps are skipped and 578 steps used. The average bond length and bond angles are similar regardless of temperature, but the standard deviations of the bond length distributions spread with higher temperature, as expected.

High Temperature Dynamics

We found that high temperature ligand dynamics qualitatively match with what is expected from AIMD simulations, where the Au-S-Au ligand groups form long chains and even rings in the very high temperature DFT. Figure 4.2C shows a rendering of the final structure of the training AIMD simulation for Au₃₈Q,[159] with variable temperature ramps ending at 1200K over a simulation of 0.025 ns, alongside a rendering of the same structure heated in a simulation using the ACE potential heated to 1200K.

4.3 Cluster Isomerization and Cluster-Cluster Reactions

Au₂₅ Isomerization

In the case of thiolate-protected gold nanoclusters, isomers exhibit different gold cluster cores or simply different arrangements of stabilizing ligands. Isolating and characterising isomers in experiments is challenging particularly in the solution phase. In a few cases, crystallization to specific isomer structures has been successful. [143, 144, 146, 147] Modifying the synthesis conditions, including exchanging the stabilizing ligand chemistry and adding counter-ions to change the cluster charge state, can induce new isomers to form.[160] In this work, known clusters will simply be referred to as Au_nX where n denotes the number of gold atoms in the cluster, and X optionally encodes the isomer identity. Literature references and experimental ligand chemistry for each cluster are listed in Table 4.1.

Cao and collaborators have shown that Au₂₅(SR)₁₈⁻¹ clusters (with a water-soluble thiol) can dynamically interconvert between two isomers depending on solvent conditions and surfactant molecules. [161] The major isomer was successfully characterized in 2008 when its crystal structure (with organo-soluble thiol) was discovered simultaneously by Murray[162] and Jin[163] groups. Another isomer, stabilized by surfactant and change of solvent, was assigned to a theoretically predicted cluster[164] and observed in gas phase ion mobility studies. [165]

Here we denominate the neutral form of the ground state isomer Au_{25A}, and the neutral form of the minor isomer Au_{25B} that has been predicted earlier based on DFT calculations.[164] Notably, the transformation from Au_{25A} to Au_{25B} is recreated with the interatomic potential. More interestingly, a pair of chiral isomers that have not previously been reported, labeled Au_{25C1} and Au_{25C2}, are also observed. These Au_{25C} isomers transform into an additional isomer, Au_{25D}, that has only 11 gold atoms in the cluster core and is a possible precursor to

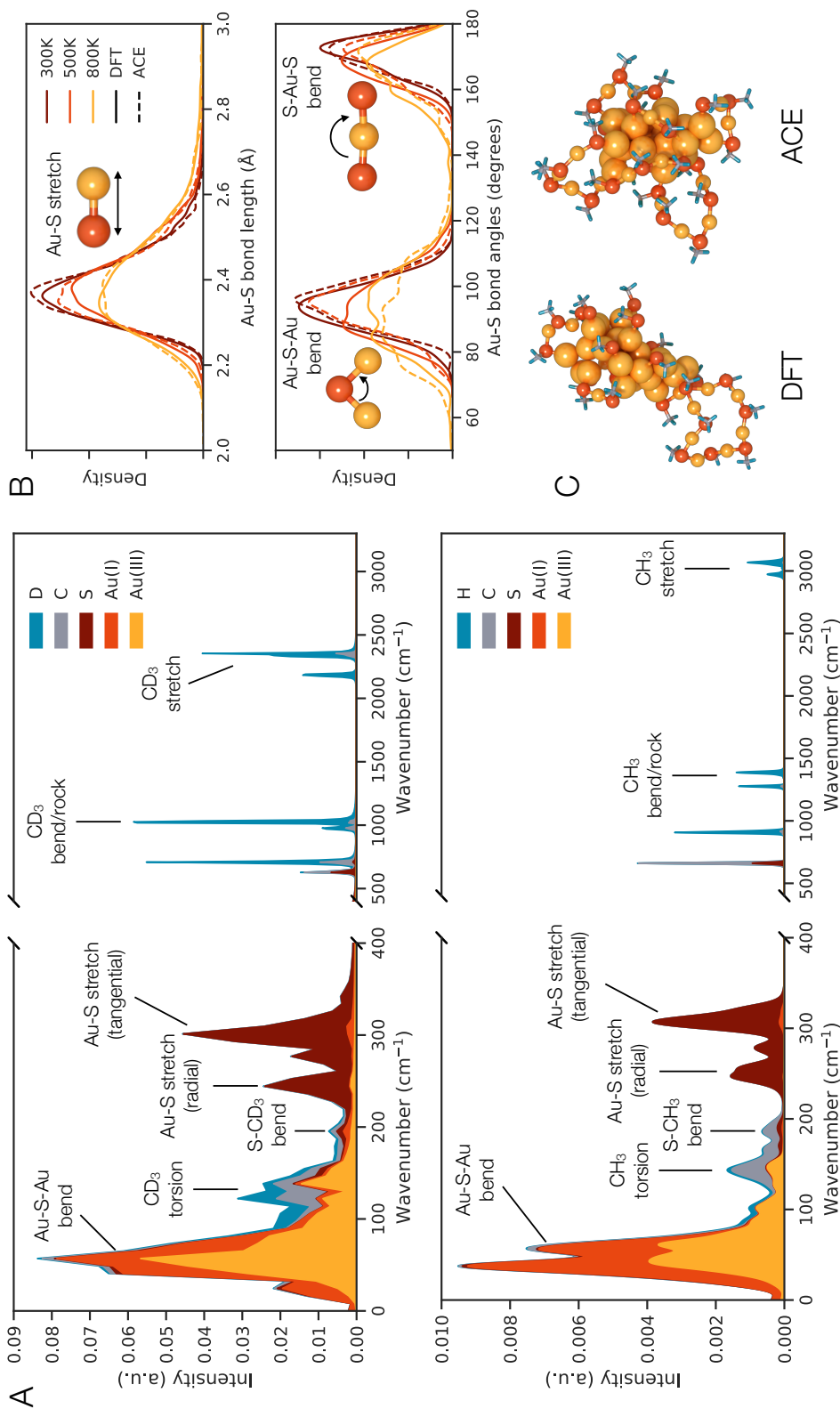


Figure 4.2: A) Vibrational density of states of Au₃₈S₄Q at 300K. Top: AIMD simulated, with hydrogen replaced with deuterium, Langevin dynamics, 1000 steps with 2 fs time steps (0.002 ns simulation) Bottom: ACE simulated, with Langevin dynamics, 90000 steps with 1 fs time steps (0.09 ns simulation). B) Characteristic bond lengths and angles in the ligand shell, as predicted with DFT and ACE. C) Snapshots of simulated Au₃₈S₄Q with deuterium at high temperatures. (Left) AIMD simulated using Berendsen dynamics for 0.025 ns, with a final temperature of 1200K. (Right) ACE simulated using Langevin dynamics for 0.025 ns, with a final temperature of 1200K.

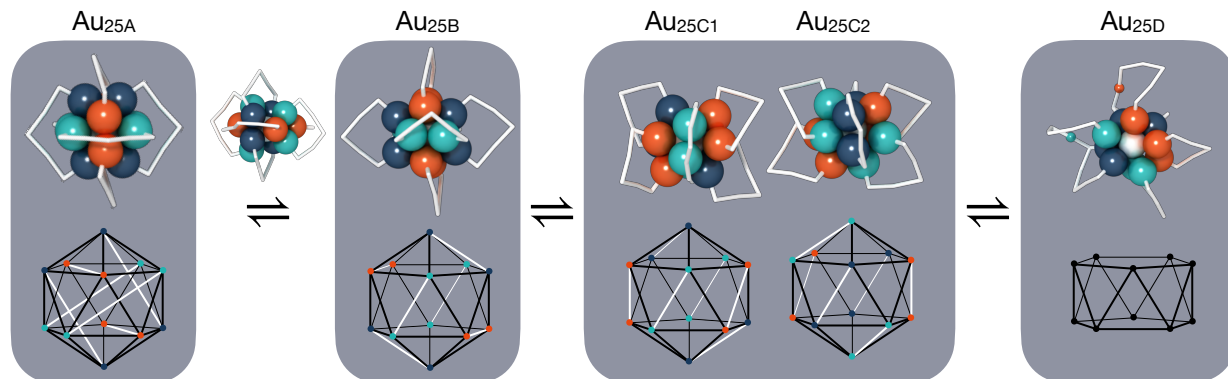


Figure 4.3: Au_{25} isomerization steps in a finite temperature simulation at 450K over 42 ns. The ground state structure, $\text{Au}_{25\text{A}}$, transforms into $\text{Au}_{25\text{B}}$, which then follows an asymmetric transition into chiral enantiomers $\text{Au}_{25\text{C1}}$ and $\text{Au}_{25\text{C2}}$, which further transform into $\text{Au}_{25\text{D}}$. Atomic renderings maintain the same coloring of each atom over the course of the transformations to help guide the eye, and gold-thiolate units ($-\text{SR}-\text{Au}-\text{SR}-\text{Au}-\text{SR}-$) are depicted in white. Schematics under the atomic renderings indicate the bond topology in each isomer, where black lines indicate gold connectivity in the icosahedral cluster core and white lines indicate ligand protecting unit connectivity. The $\text{Au}_{25\text{D}}$ structure is labile, thus having no fixed conformation of the ligand groups.

multi-cluster coalescence. A summary of the observed isomerization pathways is presented in Figure 4.3.

Simulations of $\text{Au}_{25\text{A}}$ at elevated temperatures (450K) reveal a temperature-induced transformation between $\text{Au}_{25\text{A}}$ and $\text{Au}_{25\text{B}}$ (elevated temperatures are used in order to accelerate the sampling of reactive events). In the $\text{Au}_{25\text{A}}$ isomer, gold atoms that are linked to one another via protecting $\text{SR}-\text{Au}-\text{SR}-\text{Au}-\text{SR}$ units are second nearest neighbors within the icosahedron, whereas they become first nearest neighbors in the $\text{Au}_{25\text{B}}$ isomer. The transformation is initiated by opening the gold cluster core, maintaining two planes of mirror symmetry (Figure 4.4). While the $\text{Au}_{25\text{B}}$ isomer exhibits slightly higher energy than the $\text{Au}_{25\text{A}}$ isomer, it exhibits greater freedom of movement and vibration in the ligand shell, indicating that the $\text{Au}_{25\text{B}}$ isomer is favored at high temperatures over the ground state $\text{Au}_{25\text{A}}$ isomer.[164]

Apart from the established isomers $\text{Au}_{25\text{A}}$ and $\text{Au}_{25\text{B}}$, we observe a reversible transformation occurring at 450 K, wherein $\text{Au}_{25\text{B}}$ converts into a previously unreported isomer, $\text{Au}_{25\text{C}}$. In contrast to $\text{Au}_{25\text{A}}$ and $\text{Au}_{25\text{B}}$, the newly identified isomer ($\text{Au}_{25\text{C}}$) is chiral, and further lacks the three mirror symmetry planes. Since both enantiomers easily interconvert between one and the other via the pathway $\text{Au}_{25\text{C1}} \rightleftharpoons \text{Au}_{25\text{B}} \rightleftharpoons \text{Au}_{25\text{C2}}$ and have nearly degenerate energies, we expect that racemic mixtures would exist (likely also in coexistence with $\text{Au}_{25\text{B}}$) if their synthesis was not guided by another chiral factor like a chiral ligand or circularly

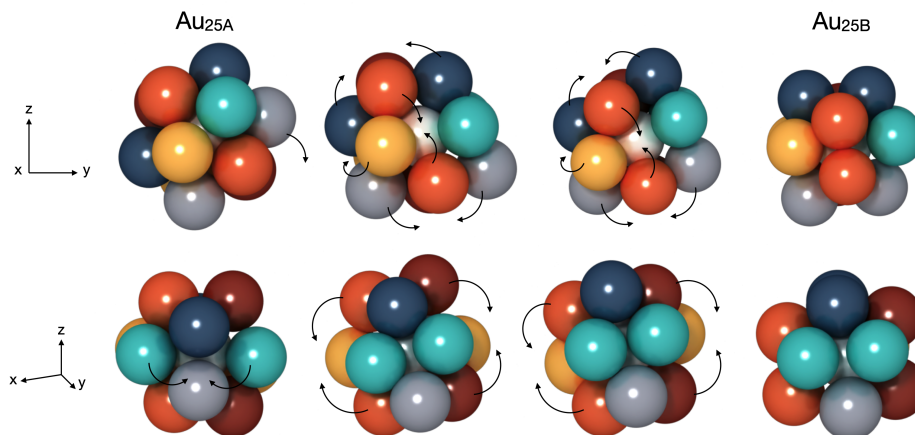


Figure 4.4: Transition steps between the $\text{Au}_{25\text{A}}$ and $\text{Au}_{25\text{B}}$ isomers. Like-colored atoms are connected via $\text{SR}-\text{Au}-\text{SR}-\text{Au}-\text{SR}$ ligands, which are omitted here for visualization purposes. In the first step of the transformation from the $\text{Au}_{25\text{A}}$ isomer to the $\text{Au}_{25\text{B}}$ isomer, two bonded atoms (teal) are pulled together due to the ligand that is attached to each vibrating away from the cluster core, thus forcing another atom (gray) from the cluster core. The transition state induced by this movement has mirror symmetry in the yz plane with an opening in the central atom for subsequent pairs of atoms (red, brown) to come together, with each remaining pair of atoms (yellow, navy) merging in quick succession.

polarized light. Interestingly, $\text{Au}_{25\text{C}}$ may be an important precursor in the coalescence of multiple Au_{25} clusters, as it transforms into a $\text{Au}_{11}[(\text{SR})_3\text{Au}_2]_2[(\text{SR})_6\text{Au}_5]_2$ ($\text{Au}_{25\text{D}}$) structure which exhibits an open facet, making it more accessible to incoming reacting species. $\text{Au}_{25\text{D}}$ exhibits facile movement of the cluster core, and as such, the decorating ligands quickly swap relative positions without breaking any Au-S bonds. The transformation of $\text{Au}_{25\text{D}}$ back to $\text{Au}_{25\text{C}}$ was not observed within the time frame of the simulation (42 ns).

Au_{25} Coalescence and Equilibration

In order to investigate coalescence, two $\text{Au}_{25\text{B}}$ clusters were simulated surrounded by vacuum at high temperatures (500K). The $\text{Au}_{25\text{B}}$ clusters follow the same individual transformation into $\text{Au}_{25\text{D}}$, and then interact with each other, initially via the attachment of protecting units ($\text{SR}-[\text{Au}-\text{SR}]_n$) to the opposite cluster, and then finally via the merging of the cluster cores (Figure 4.5). The atoms at this temperature show facile rearrangement, with gold atoms that were once part of the core joining the protecting groups, as well as the cluster core mixing easily. The coalesced structure has 50 Au atoms and 36 SCH_3 ligands, which is more ligands than the core needs to be protected (Au_{52} , for example, has 32 SCH_3 groups, see Table 3.2). Because of this supersaturation of ligand groups on the cluster core, the polymer-like units tend to pinch together, resulting in $[\text{AuSR}]_n$ ring formation. These rings will coordinate with

the cluster core, and from this position can desorb from the cluster entirely (with desorption defined as the point where all atomic distances are longer than 3.2Å, 2.8Å, 2.5Å, and 2Å for Au-Au, Au-S, S-C, and C-H bonds respectively). Several $[\text{AuSR}]_n$ ring sizes were observed ($n = 4, 5, 6, 8, 12, 13$), with $[\text{AuSR}]_4$ being the most commonly formed ring size. Since the ligand rings have a fixed ratio of gold atoms to thiolate groups, a predictable resulting cluster size is formed, $\text{Au}_{50-n}(\text{SCH}_3)_{36-n}$. As such, a variety of ligand to gold ratios are achievable: anywhere from $\text{Au}_{50}(\text{SCH}_3)_{36}$ ($n=0$) to a bare 14-atom gold cluster ($n=36$). This equilibration simulation was run for 134 ns, during which time, a variety of clusters were sampled, ranging from $\text{Au}_{50}(\text{SCH}_3)_{36}$ to $\text{Au}_{34}(\text{SCH}_3)_{20}$ ($0 \leq n \leq 16$). A summary of the sizes sampled over the complete trajectory is included in Figure 4.5.

Neutral $\text{Au}_{25}(\text{SCH}_3)_{18}$ in solution has been observed to transform into $\text{Au}_{38}(\text{SCH}_3)_{24}$ without any co-reactants at 65 degrees C.[166] In this simulation, the $\text{Au}_{38}(\text{SCH}_3)_{24}$ cluster size was generated via multiple pathways, including subtracting three $[\text{AuSR}]_4$, two $[\text{AuSR}]_6$ or an $[\text{AuSR}]_{12}$. Less stable cluster geometries are more likely to have $[\text{AuSR}]_n$ rings add onto the cluster, rearrange, and then leave again. As this simulation duration is relatively short, we hypothesize that given more time and via this ring-mediated ligand exchange, more stable clusters can be easily achieved, and thus the thermodynamic product will likely form.

The ligand exchange reaction has been observed via labeling different ligand types in solution and observing the ligands exchange over time.[167] While free monothiol exchange has been postulated to be responsible for the ligand exchange reaction in thiolate-protected nanoclusters, [151, 168, 169] our simulations indicate that in addition to free monothiol exchange, ligand exchange is facilitated via $[\text{AuSR}]_n$ ring exchange. The $[\text{AuSR}]_n$ rings have been observed previously[170–174] and form here spontaneously upon the merging of two clusters given the relative excess of protecting ligands to gold core.

4.4 Conclusion

We have developed and validated an interatomic potential in the ACE framework, trained on a large number of DFT calculations, suitable for dynamical studies of ligand-protected gold nanoclusters for timescales that are at least four orders of magnitude longer than what is available for traditional AIMD simulations. The potential is accurate over a range of shapes and sizes, can handle reactive chemistry and high temperatures, and may be used to simulate a variety of complex behaviors including crystallization, ligand exchange, agglomeration, and synthesis. Future work may include adding explicit or implicit solvation and partial charges on each atom, for greater accuracy in representing solvated nanoclusters. Similarly, extending the model to chemically varied ligand molecules would give insights into the steric effect on nanocluster behavior. The potential can be upfitted with additional training data and can be considered as a successful proof-of-concept to be extended for other ligand-protected metal clusters in the future. To this end, we have opened all training data and essential scripts for the benefit of the community.

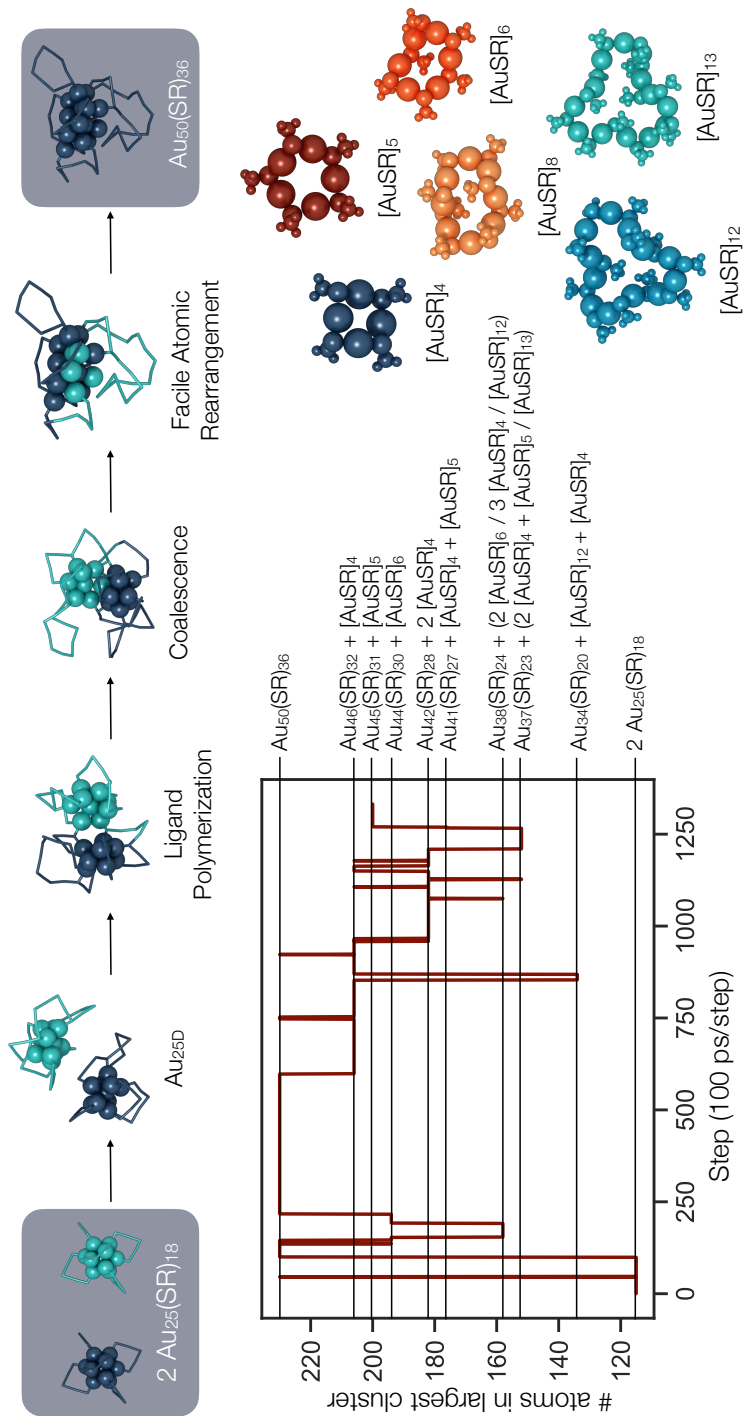


Figure 4.5: Finite temperature simulations (500K) of two Au_{25}B clusters show possible mechanisms of coalescence, here proceeding via isomerization into the Au_{25}D isomers, followed by ligand group interaction, and finally the merging of the cluster core. An excess of protecting ligands then leave the cluster as $[\text{AuSR}]_n$ rings with $n \in \{4, 5, 6, 8, 12, 13\}$. The $[\text{AuSR}]_n$ rings aid in size equilibration and metal exchange between the cluster core and protecting groups. Many sizes of clusters, each with the predictable formula $\text{Au}_{50-n}(\text{SR})_{36-n}$ are observed in the 134 ns simulation. The long MD trajectory (134 ns) is sampled by snapshots separated by 100 ps. The composition of the simulated system (main cluster and the fragments) is determined at each snapshot. $[\text{AuSR}]_8$ and $[\text{AuSR}]_{13}$ were observed, but with lifetimes shorter than the 100 ps sampling. Figure 4.6 shows several snapshots from the simulations.

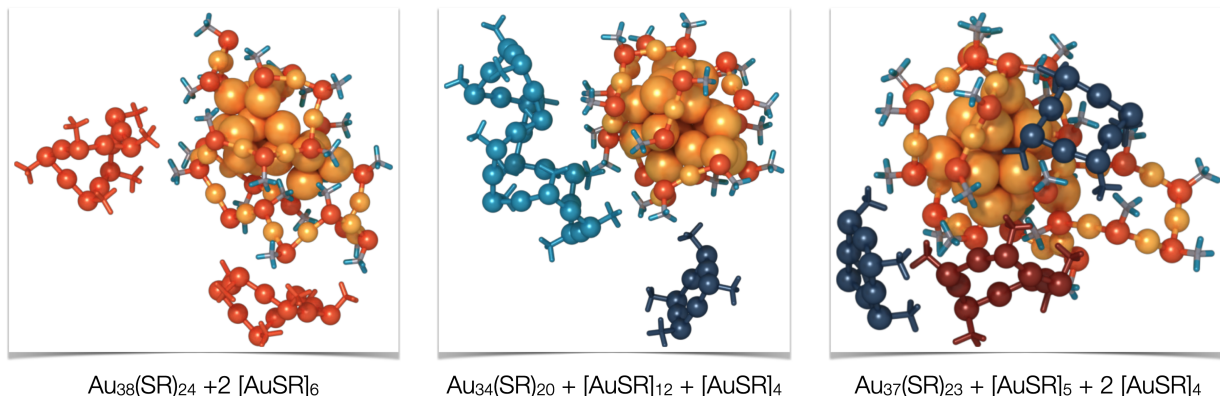


Figure 4.6: Snapshots of a MD simulation in which two Au_{25}B clusters were heated to 500K, resulting in their coalescence and equilibration into clusters with sizes $\text{Au}_{50-n}(\text{SR})_{36-n}$ and $[\text{AuSR}]_n$ rings with $n \in \{4,5,6,8,12,13\}$

Our $0.1 \mu\text{s}$ timescale simulations yielded rather striking predictions of possible atom-scale mechanisms for high-temperature dynamics of the $\text{Au}_{25}(\text{SR})_{18}$ cluster and its reactions. Chiral isomerization and subsequent transformation to higher-energy, more reactive isomers is observed, in particular featuring a “polymerized” layer of gold-thiolate units exposing a reactive gold surface that facilitates coalescence. Furthermore, after about 50 ns, the system achieved a “dynamical equilibrium” in which continuous reactions between the coalescent cluster and ring-like $[\text{AuSR}]_n$ fragments took place, leading to formation of a series of $\text{Au}_{50-n}(\text{SR})_{36-n}$ clusters including the well-known $\text{Au}_{38}(\text{SR})_{24}$ composition.

Our results might offer a key to understand atom-scale mechanisms of $\text{Au}_n(\text{SR})_m$ clusters taking place during energetic processes such as fragmentation reported in electrospray ionization mass spectrometry[175–179] and ligand removal that is observed during heating of clusters to activate them as catalysts on oxide surfaces. [180, 181]

Exchange of ligands and metal atoms between “magic” clusters in solvent phase has been reported frequently during the past years.[182, 183] Furthermore, NMR studies implied that even metal atoms inside a given “magic” ligand-stabilized silver cluster exchange between all symmetry-unique sites in the timescale (seconds) of the measurement.[184] Maran’s group reported already in 2018 that “magic” neutral $\text{Au}_{25}(\text{SR})_{18}$ clusters fuse together in solvent at slightly elevated temperatures to form the $\text{Au}_{38}(\text{SR})_{24}$ cluster which implies a greater thermodynamic stability of the latter one.[166] We have indeed found $\text{Au}_{38}(\text{SR})_{24}$ as one possible outcome of the Au_{25} fusion reaction in this work, but our current simulation times are too short to establish unambiguously a thermodynamic equilibrium where only the $\text{Au}_{38}(\text{SR})_{24}$ would dominate. However, all the experimental evidence gathered during the past years indicates that atom-scale dynamics of these types of nanomaterials under ambient conditions in solvents or in gas phase is still poorly understood, and theoretical developments facilitating reliable long timescale simulations are urgently needed. We hope that our work will open

avenues for such investigations at the microsecond time-scale and beyond.

4.5 Methods

Ab Initio Training Data

The fitted Au-S-C-H potential developed here is highly tuned to the training examples, specifically because gold nanoclusters exhibit molecular-like behavior that is very different to that of the bulk. The training data for this potential were sourced from previous studies on the Au₃₈ T and Q isomers[135, 159] that were initially discovered by Tian and Qian.[143, 144] 12,413 Au₃₈Q structures and 12,647 Au₃₈T structures in total were obtained from the Juarez-Mosqueda study and consist of AIMD trajectories with temperatures spanning 500K-1200K, deuterated structures, 2fs time steps and Berendsen dynamics[159].

Additionally, structures were sourced from a study by Pihlajamäki et al., as this study used a different machine learning architecture (EMLM) in order to enable Au-S-C-H simulations via Monte Carlo dynamics.[135] This set of structures included 5,749 structures that were generated via their Monte Carlo simulations and added to the training data, as well as their testing data set, which consists of 11,702 total structures generated with AIMD simulations of each Au₃₈ isomer at various temperatures (300K, 500K, 800K) with deuterated structures, 2fs time steps and Langevin dynamics. Here, we use the same testing dataset.

In addition to these initial 30,809 training structures, 1,133 structures were systematically generated, calculated with DFT, and added to the training set over the course of the fitting of this potential in a process called active learning (see Methods: Active Learning section).

We used the real space DFT code, GPAW,[185, 186] to generate training and testing data. For the sake of consistency, the settings were the same as used by Juarez-Mosqueda *et al.* [159] The chosen exchange-correlation functional was Perdew-Burke-Ernzerhof functional (PBE) [187] and grid spacing was set to 0.2 Å. Two versions of GPAW, GPAW 1.3.0 and GPAW 22.8.0, were used to calculate the training data. There are some reference energy differences between the two versions of GPAW, and the benchmarking of these energy differences is included in Supplementary Figure 4.7.

Active Learning

The AIMD training and testing datasets exhibit strong correlation, meaning that structural snapshots separated by only 2fs in time contribute minimally to additional information in the model. AIMD data is useful for parametrizing low-energy structures that are very similar to the starting geometry, however high energy structures that are far from equilibrium are unlikely to be captured well using only AIMD training data. Additionally, some interactions never arise over the course of a DFT simulation because they are non-physical. For example, sulfur atoms are rarely within a few angstroms of other sulfur atoms in the AIMD simulations, since it is not favorable for the ligand groups to come too close together due to repulsive steric interactions. As a result, spurious interactions between sulfur atoms were a major

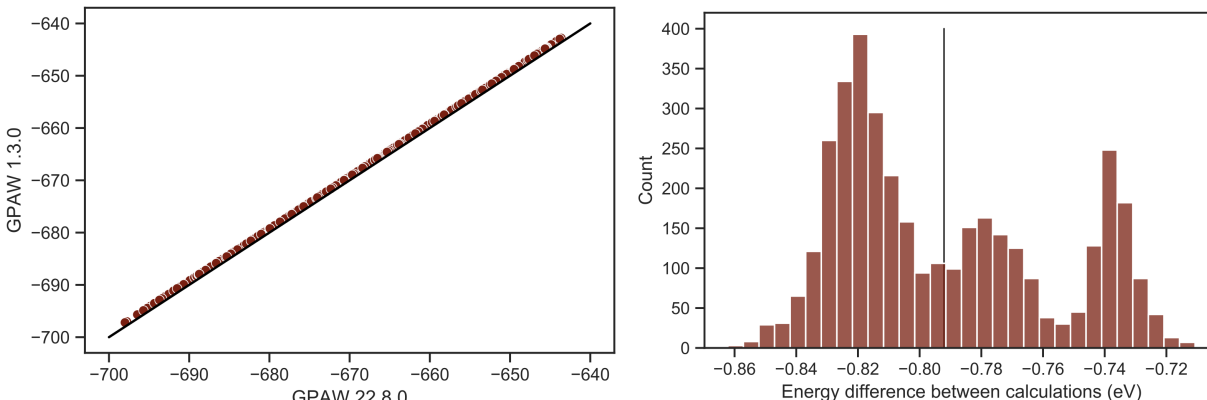


Figure 4.7: (Left) A systematic energy error was observed due to the versioning of the GPAW simulation code (1.3.0 vs. 22.8.0). In order to reconcile multiple datasets computed with the two versions of the code, benchmarking was performed by recalculating many training structures and quantifying the energy shift (0.79 eV). (Right) Deviations around this shift were observed and may contribute to statistical noise in the training data.

failure mode in general simulations of individual clusters and interacting ligand shells. In order to learn interactions that are not present in the training data, a process called active learning (AL) was employed so that the final model knows how to handle very general, and even non-physical, interactions.

In AL, the current best version of the potential is used to simulate test geometries, while a metric of the dissimilarity of the structure to the training set is assessed. The ACE potential framework has a metric for this dissimilarity, the extrapolation grade, that is calculated for every atom and measures how different the atomic environment is from those present in the training data.[188] As simulations are running, structures can be identified as having high extrapolation grade measurements (an extrapolation grade of greater than 1 indicates that the atomic environment extends beyond the bound of atomic environments that are present in the training data), at which point they can be calculated with DFT and added to the training set to populate these under-sampled regions of the PES. A total of 1,133 structures were added to the potential over the course of three rounds of AL. In each round of AL, non-physical interactions were identified and these failure modes were addressed and did not occur in subsequent versions of the potential (Figure 4.8).

ACE Potential Architecture

Using the ACE framework, it would be possible to learn any atomic property (e.g. magnetism) but here we use ACE to learn the energies and forces of nanoclusters, so that we may perform MD simulations. Its general nature means that the ACE formalism can be parametrized to have the same form as many common potential architectures, including mo-

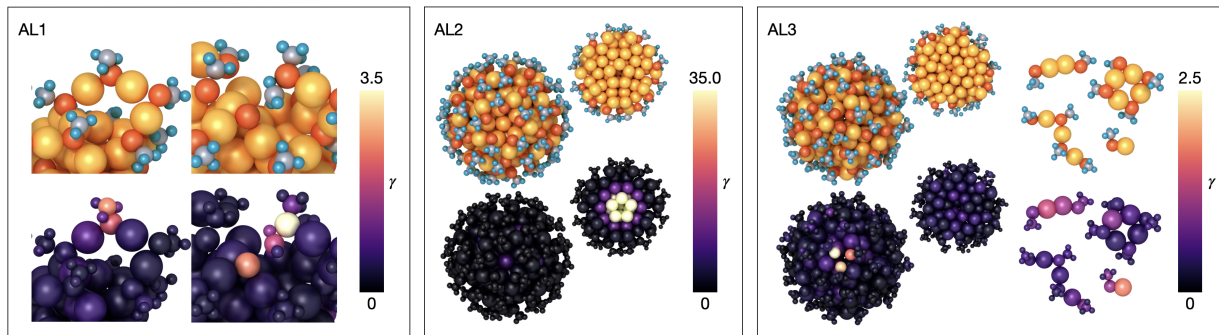


Figure 4.8: Three rounds of active learning were performed, addressing various non-physical interactions that occurred in testing the fitted potential (γ : extrapolation grade). In the first fitted potential, methyl groups tended to adopt planar configurations between the C and 3 H atoms, with the hydrogens tending to interact non-physically with the S atom. Additionally, methyl groups sometimes jumped from one sulfur to a neighboring thiol ligand. In a subsequent version of the potential, active learning on Au_{144} was performed, since bulk gold was not present in the training data consisting of smaller structures (Au_{38}). The final stage of active learning addressed the tendency of sulfur groups to coordinate in groups of 3, as well as adding data on small clusters and interacting ligand shells. In each step, the targeted behavior was resolved after active learning.

ment tensor potentials (MTP) and Gaussian approximation potentials (GAP). To construct an ACE potential, we begin by describing atomic environments using spherical harmonics, up to angular momentum l_{max} , and radial basis functions represented by the n_{max} first power-law scaled Chebyshev polynomials.[189] Atomic interactions are limited to 9\AA at which point radial components approach zero.

These atomic basis functions are combined into a new set of symmetrically invariant basis functions, B . Appropriate coefficients, $c_{nl}^{(K)}$, are learned over the course of fitting the potential to best represent the energies of the training examples.

$$E_i(\sigma, \mu) = \sum_{\mathbf{Knl}} c_{nl}^{(K)} B_{inl}$$

In this equation, i represents the atomic index, σ represents the collection of vectors between atom i and its neighbors, $(r_{1i}, r_{2i}, \dots, r_{Ni})$ and μ is the associated list of chemical species of each atom, $(\mu_1, \mu_2, \dots, \mu_N)$. K represents the multi-body order of the interaction, (e.g. an interaction between 4 atoms would be 4-body, $(K) = (4)$). The optimization of the coefficients, $c_{nl}^{(K)}$, is performed by minimizing a loss function, Λ , that is given by:

$$\Lambda = (1 - \kappa) \Delta_E^2 + \kappa \Delta_F^2$$

κ determines the relative contribution of the squared deviation in predicted energies, Δ_E^2 , and squared deviation in predicted forces, Δ_F^2 , to the total loss function, Λ . Here, κ is set

to 0.9 in order to prioritize learning the forces such that the dynamics of MD simulations would have greater fidelity to the true movements.

Here, we use linear embedding, so the total energy is taken simply as the linear sum of atomic energies. For more detail, we refer the reader to the development of ACE by Drautz.[58]

Body-Order Hierarchical Fitting

With over a thousand basis functions in the target potential structure, finding these optimal coefficients is non-trivial. Thus, the fitting was conducted in a sequential manner, with low body-order fits completed, and additional functions added and fit again. During fitting, active learning was also employed in order to improve the training examples and specifically target the regions of the potential energy surface that were the least well represented by the training data.

First a 2-body potential with 125 total basis functions was fitted to a convergence criterion of $1e-8$ in the gradient of the loss function. Then, using these learned 2-body interaction coefficients as starting values, 950 3-body interactions were added, and this potential was fitted again. Subsequently, the first round of AL was added. Next, 559 Au/S 4-body interactions were added and the potential was fitted again. It is expected that the scaling of accuracy is log-log linear in the number of functions and in the number of training data points,[190] however there is a risk of overfitting when using too many basis functions. In total, 1,634 basis functions make up the final potential.

Multi-body interactions were indeed necessary for capturing the complex behavior of the gold core and ligand shell. For example, with only 3-body interactions, sulfur often bonded to more than two gold atoms, even forming bonds with up to 4 gold atoms. With 4-body interactions, it is less common for sulfur to form more than two gold bonds, and may do so as a coordinating bond as opposed to a covalent bond.

The convergence of the final potential was achieved as 0.02 in the gradient of the loss function. The architecture of the final potential is included in Table 4.2.

Molecular Dynamics

All MD simulations were performed with the performant atomic cluster expansion (PACE) implementation in the LAMMPS simulation software (ML-PACE).[54, 191] A Langevin thermostat was used for all MD simulations with the Au-S-C-H ACE potential, using 1fs timesteps (unless otherwise noted). The evaluation speed for MD simulations of one (two) Au₂₅ cluster(s) with LAMMPS is 42 (24) ns/day on a single CPU node (containing 2 AMD EPYC 7763 Milan CPUs with 64 cores per CPU) Evaluation speeds may be improved with parallelization across multiple nodes or with the enabled GPU support with the KOKKOS-accelerated implementation of PACE. All simulation results and nanocluster structures were rendered with Ovito 3.8.3.[192]

Table 4.2: Architecture of final potential. The n_{\max} and l_{\max} are reported for each multi-body interaction type (i.e. 2-body/3-body/4-body)

Elements	Max Body-Order	n_{\max}	l_{\max}
Au-Au	4-body	11/5/5	0/3/3
S-S	3-body	8/3	0/2
C-C	3-body	6/2	0/1
H-H	3-body	4/1	0/1
Au-S	4-body	8/5/4	0/3/3
Au-C	3-body	8/3	0/2
Au-H	3-body	8/3	0/2
S-C	3-body	8/3	0/2
S-H	3-body	8/3	0/2
C-H	3-body	8/3	0/2
All Ternary	3-body	8/3	0/2

Usage note: It is not recommended to use this potential with large time steps, greater than 1fs/step. In simulations at 500K with 2fs time steps, unstable behavior was observed with reasonable starting geometries. High temperature behavior has not been extensively tested, so the recommended maximum temperature would be 500K, though no instabilities with 1fs timesteps up to 1200K have yet been observed in testing.

4.6 Acknowledgements

C.A.M. would like to acknowledge Ralf Drautz, Yury Lysogorskiy and Matous Mrovec for their helpful guidance and hosting a community ACE workshop, as well as María Francisca Matus and Sam Blau for useful discussions. C.A.M. acknowledges the National Defense Science and Engineering Graduate (NDSEG) fellowship and the Kavli ENSI Graduate Student Fellowship for financial support. The research at UC Berkeley / LBNL used resources of the National Energy Research Scientific Computing Center, a DOE Office of Science User Facility supported by the Office of Science of the U.S. Department of Energy under Contract No. DE-AC02-05CH11231 using NERSC award BES-ERCAP0024004. The research at University of Jyväskylä was supported by the Academy of Finland (grant 351582) and the Finnish national supercomputing center CSC.

4.7 Data Availability

The fitted potential, training and testing datasets, and simulation results are all available at https://materialsproject-contribs.s3.amazonaws.com/index.html#ausch_potent

ial/ DOI:10.17188/mpcontribs/2356816.

Chapter 5

Surface Environment Impact on Binary Metal Nanoparticle Phases

Reproduced in part with permission from “Chen, P.C., Gao, M., McCandler, C.A. et al. Complete miscibility of immiscible elements at the nanometre scale. Nat. Nanotechnol. (2024). <https://doi.org/10.1038/s41565-024-01626-0>” Copyright 2024 The Authors.

Understanding the mixing behaviour of elements in a multielement material is important to control its structure and property. When the size of a multielement material is decreased to the nanoscale, the miscibility of elements in the nanomaterial often changes from its bulk counterpart. However, there is a lack of comprehensive and quantitative experimental insight into this process. Here we explored how the miscibility of Au and Rh evolves in nanoparticles of sizes varying from 4 to 1 nm and composition changing from 15% Au to 85% Au. Quantitative electron microscopy analysis performed by the Yang group (led by Peng-Cheng Chen and Mengyu Gao) showed that the two immiscible elements exhibit a phase-separation-to-alloy transition in nanoparticles with decreased size and become completely miscible in sub-2 nm particles across the entire compositional range. I performed theoretical analyses to independently investigate the miscibility claims and, if validated, attempt to explain the nanoscale miscibility phenomena. Interestingly, the observed immiscibility-to-miscibility transition is dictated not only by particle size and composition, but also by the surface adsorbates resulting from the synthesis conditions.

5.1 Summary of Quantitative Electron Microscopy of Au-Rh Nanoparticles

A summary of the experimental findings and analysis performed by the Yang group (led by Peng-Cheng Chen and Mengyu Gao) is presented in Figure 5.1 as a size-dependent phase diagram of Au-Rh nanoparticles. The experimental data points of heterostructured, interme-

diated and alloyed particles are denoted by green Δ , red \square and blue \circ , respectively. Compared with the large miscibility gap in the Au–Rh bulk phase diagram, the gap is diminished in sub-4 nm Au–Rh particles and can be closed across the entire compositional range in the sub-2 nm size regime. With the decrease in particle size, Au–Rh nanoparticles exhibit a transition from heterostructured to intermediate and alloyed, whereas the actual transition occurs in a different size region for different compositions. The closer the Au/Rh ratio is to an equimolar value, the smaller the particle size needed to initiate this transition. The characterization of particles as being heterostructured and alloyed was surprising given the large miscibility gap in the bulk phase and previous theoretical studies predicting the core-shell geometry as the most favorable. As a result, I performed calculations to investigate further.

5.2 Theoretical Analysis of Miscibility in Au-Rh Nanoparticles

Semi-empirical models have been widely used to explain the nanosize effect on the mixing pattern of immiscible elements[193–195]. For nanoparticles, the undercoordinated atoms on the surface are considered to diminish the interaction between incompatible atoms like Au and Rh, which facilitates the alloying of elements. In comparison, computational simulations based on density functional theory (DFT) or molecular dynamics have predicted core-shell Au–Rh nanoparticles as the stable structure[196–198]. However, these models neglect surface passivation effects such as the adsorption of environmental species, which are highly likely to react with the nanoparticle surface area during synthesis. Given the different structures reported in the literature, we developed models that treat different types of Au–Rh structures (heterodimer, alloy and core-shell structures) to interpret how particle size, composition and available adsorbates affect miscibility. The models were parametrized with DFT calculations to calculate the total energy of Au–Rh nanoparticles and assess the thermodynamically stable configurations.

Thermodynamic Model Construction

For a bulk-scale bimetallic material, the Gibbs free energy of mixing can be described by Eq. 5.1-5.2, where x_{Au} and x_{Rh} are the atomic fractions, and R is the molar gas constant.

$$\Delta G_m = \Delta H_m - T\Delta S_m \quad (5.1)$$

$$\Delta S_m = -R[x_{Au}\ln x_{Au} + x_{Rh}\ln x_{Rh}] \quad (5.2)$$

As shown in Fig. 5.2a and 5.2b, the high immiscibility between Au and Rh can be explained by the positive Gibbs free energy of mixing (ΔG_m), which is mainly contributed by the enthalpy of mixing (ΔH_m). The positive ΔH_m means that Au and Rh are energetically unfavorable to be mixed as compared with their monometallic phases. In contrast, the negative configurational entropy term ($-T\Delta S_m$) promotes alloying. Within the temperature

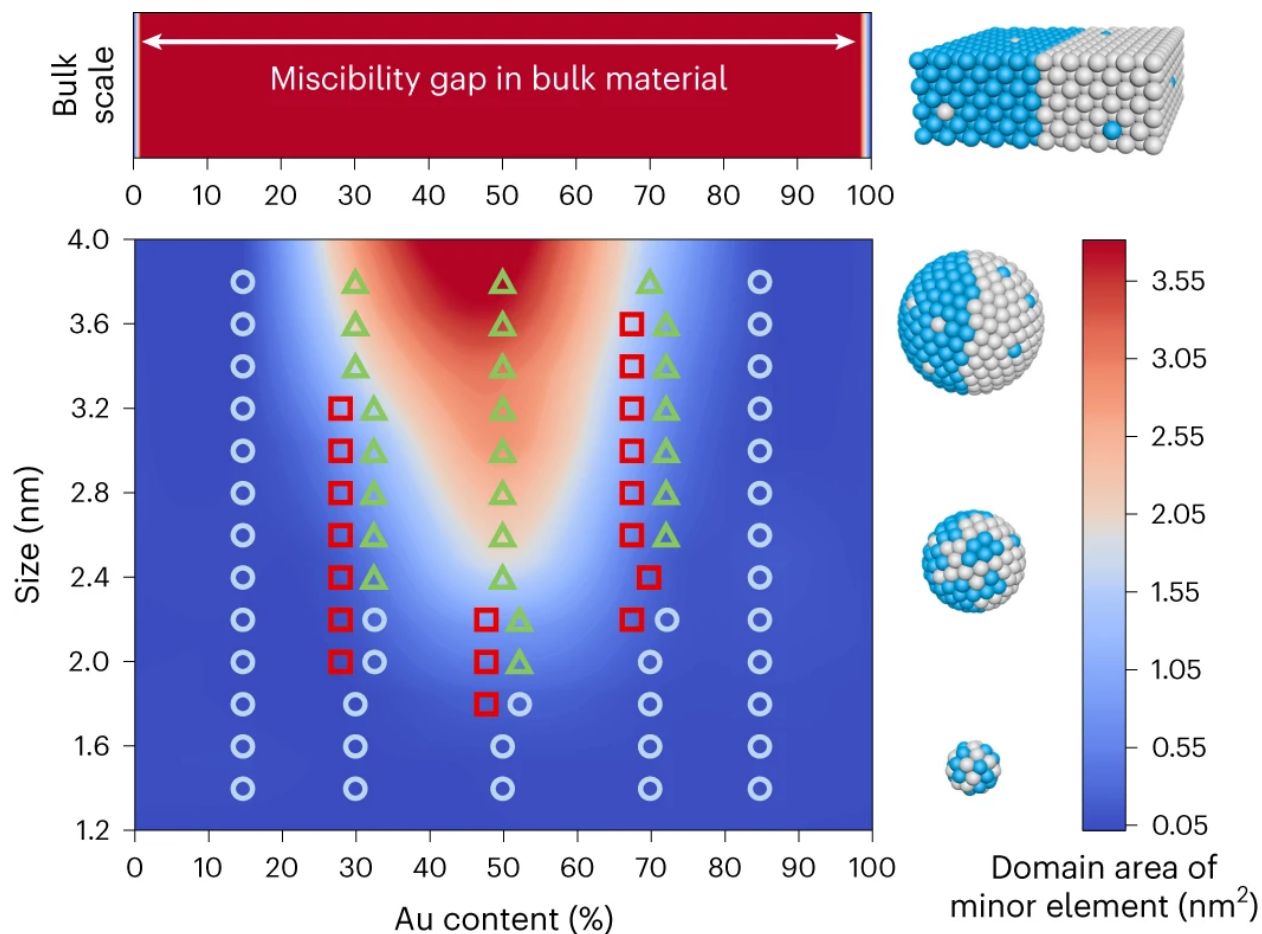


Figure 5.1: The phase map is projected based on the quantitative analysis of the cross-section area of the minor element domains, that is, Au domains in Rh-rich nanoparticles (Au_{0.15}Rh_{0.85}, Au_{0.3}Rh_{0.7} and Au_{0.5}Rh_{0.5}) and Rh domains in Au-rich nanoparticles (Au_{0.7}Rh_{0.3} and Au_{0.85}Rh_{0.15}). The experimentally observed data points of alloyed (circles, light blue), intermediate (squares, red) and heterostructured (triangles, green) nanoparticles are shown on the map. The schematic depicts the transition from phase separation to alloying in Au–Rh nanoparticles.

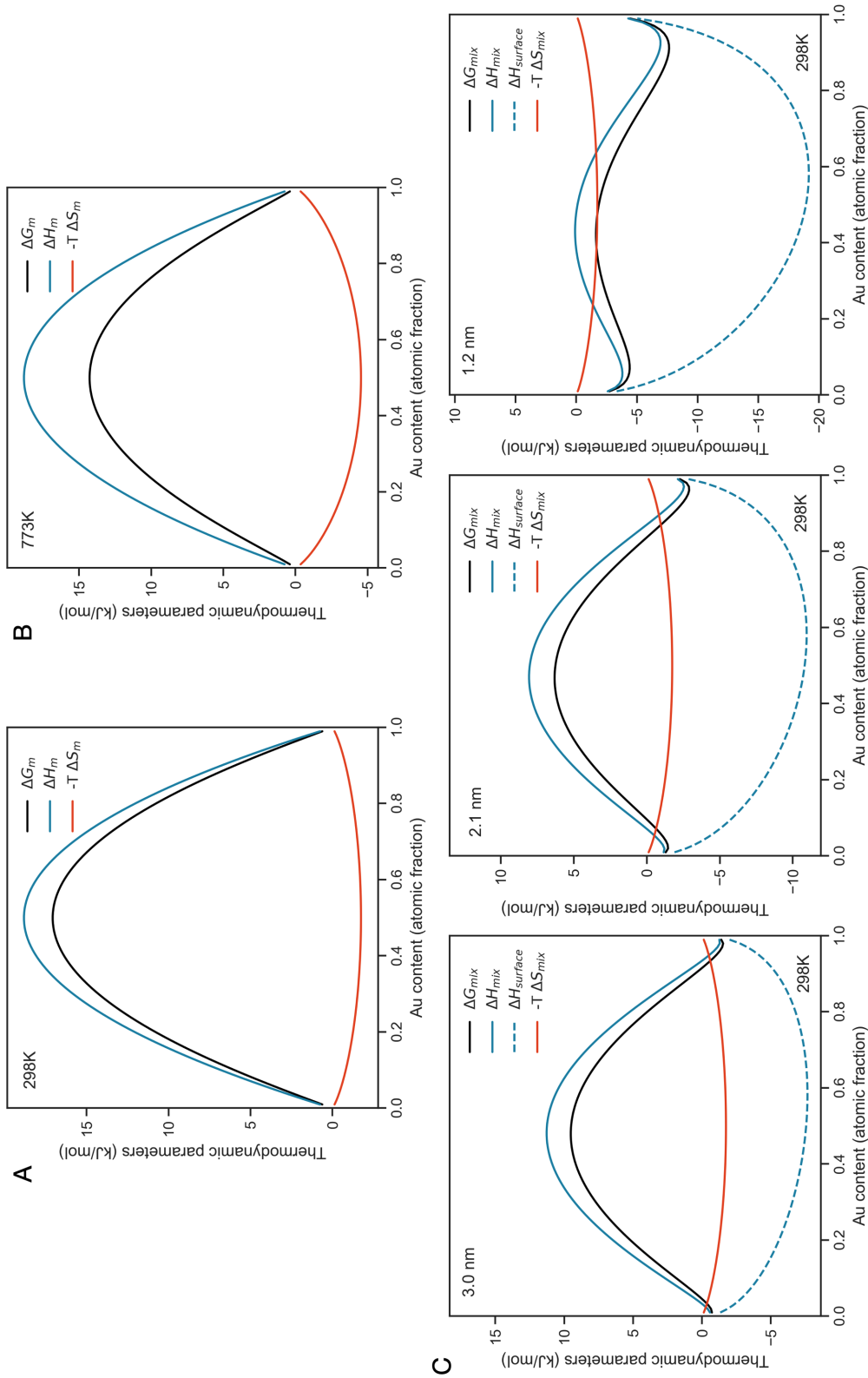


Figure 5.2: Thermodynamic parameters of bulk scale AuRh binary systems at (A) 298 K and (B) 773 K. The enthalpy of mixing (ΔH_m) at the bulk scale is obtained using the regular solution model. The entropy of mixing plotted here is the configurational entropy in a binary system. (C) Estimated thermodynamic parameters (Eq. 5.1-5.5) of AuRh nanoparticles with different particle sizes at 298K.

range of 25-500°C, the thermodynamic state of AuRh is dominated by the ΔH_m , meaning that Au and Rh are virtually immiscible in a bulk material within the entire compositional range at temperature lower than 500°C (Fig. 5.2a). In addition, it is easiest to phase separate Au and Rh when the material contains equimolar ratio of Au and Rh. In this case, the enthalpy of mixing (ΔH_m) and the corresponding ΔG_m reach the maxima.

For a AuRh binary system at the nano and cluster length scales, the enthalpy term can be rewritten as Eq. 5.3-5.5. The regular solution model is used here to approximate the bulk enthalpy of mixing, ΔH_{bulk} . The regular solution model assumes that the energy of the solid solution is due only to the interaction between nearest-neighbor pairs. The regular solution interaction parameter, w , represents the difference in bond energy between Au-Rh bonds and Au-Au/Rh-Rh bonds. Here, the regular solution interaction parameter is positive because Au and Rh have a positive enthalpy of mixing in the bulk. Z represents the average number of nearest neighbors per atom and n represents the number of atoms in a AuRh nanoparticle. Since the Au and Rh have FCC lattices in their bulk phase, Z is assumed to be 12 as there are 12 nearest neighbors per atom in the FCC lattice. An additional term $\Delta H_{\text{surface}}$ can be added to describe the surface effect, which addresses the change in surface and interfacial energies upon transition from the heterodimer phase to the alloy phase.

$$\Delta H_m = \Delta H_{\text{Bulk}} + \Delta H_{\text{Surface}} \quad (5.3)$$

$$\Delta H_{\text{Bulk}} = \frac{nZ}{2} x_{\text{Au}} x_{\text{Rh}} w \quad (5.4)$$

$$\Delta H_{\text{Surface}} = H_{\text{Surface, Alloy}} - H_{\text{Surface, Heterodimer}} \quad (5.5)$$

The surface enthalpies are calculated as the surface areas of each interface multiplied with the corresponding surface energy. Only alloyed and heterodimer structures were observed experimentally, but in order to confirm that core-shell structures are not present in the experiment, an energetic model for the core-shell structures was also tested. The total enthalpies of the interfaces of the heterodimer, alloy, and core-shell phase are written in Eq. 5.6, 5.7 and 5.8 where r represents the radius of a spherical nanoparticle, r_{in} represents the radius of the core of a core-shell nanoparticle, a represents the radius of the Au-Rh interface in a heterodimer, and a_{Au} and a_{Rh} represent the surface area of each element in the heterodimer. α , β and γ are the surface energy of Au, the surface energy of Rh, and the interfacial energy of Au-Rh, respectively.

$$\Delta H_{\text{Surface, Alloy}} = 4\pi r^2 (\alpha x_{\text{Au}} + \beta x_{\text{Rh}}) \quad (5.6)$$

$$\Delta H_{\text{Surface, Heterodimer}} = \gamma \pi a^2 + \alpha a_{\text{Au}} + \beta a_{\text{Rh}} \quad (5.7)$$

$$\Delta H_{\text{Surface, Core-shell}} = 4\pi r^2 \alpha + 4\pi r_{\text{in}}^2 \gamma \quad (5.8)$$

A schematic of the model construction and relevant variables is included in Figure 5.3. Previous work has used a similar approximation for a multi-component nanoparticle using a spherical construction and (111) surface tensions and found that it correctly accounted

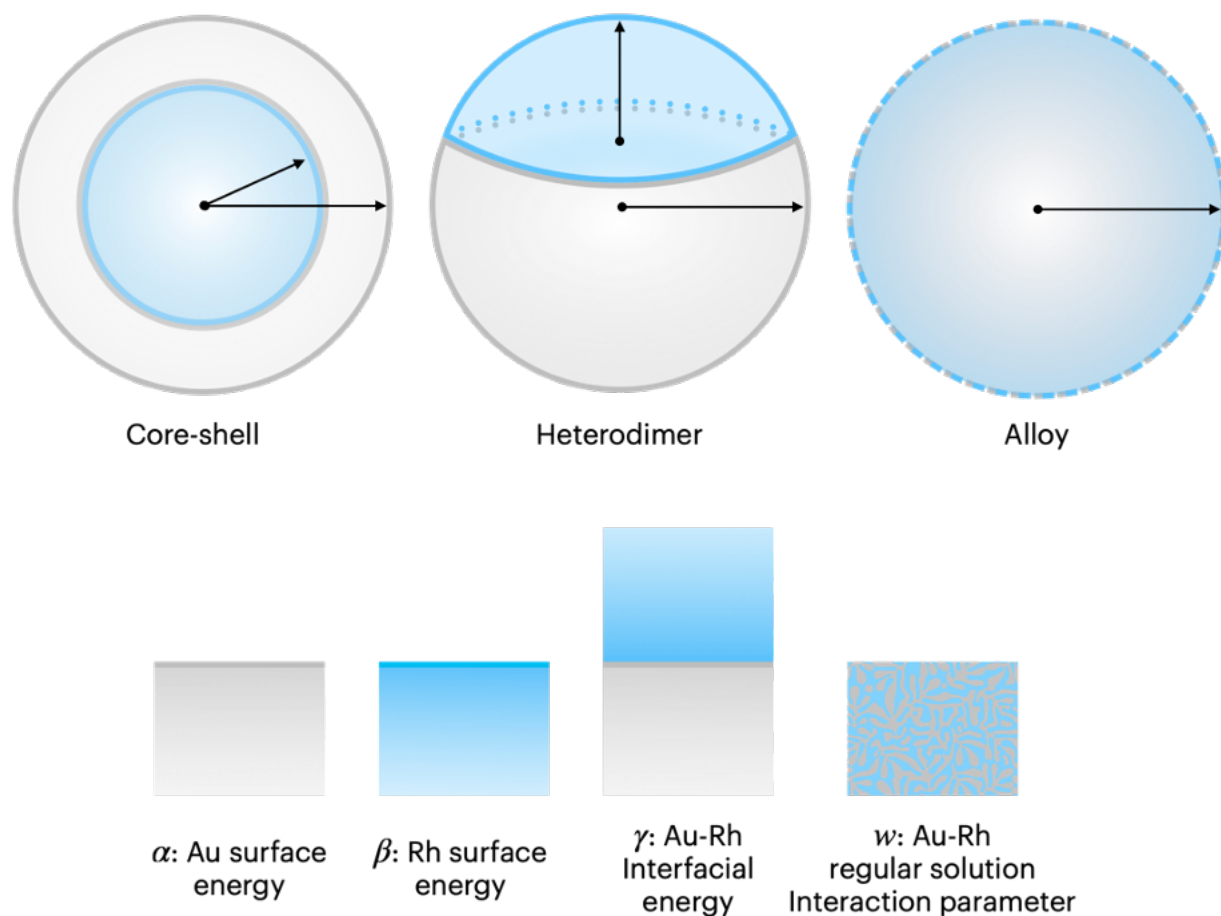


Figure 5.3: Models of core-shell, heterodimer, and alloy configurations used for assessing the thermodynamic structures of AuRh nanoparticles.

for the geometries of phase boundaries in several ternary nanoparticles.[199] In general, the surface term $\Delta H_{\text{surface}}$ suppresses the enthalpy curve toward a more negative value and promotes the alloying of Au and Rh (Fig. 5.2c). When the nanoparticle size decreases, the surface term $\Delta H_{\text{surface}}$ becomes more pronounced in determining the total enthalpy. Eventually, decreasing the material size to a critical diameter can make immiscible elements thermodynamically alloyable.

Values of α , β , γ and w for the Au-Rh system were estimated with density functional theory (DFT). To calculate α (β), the energy of a slab of Au (Rh) with the (111) surface exposed was calculated and referenced to the bulk Au energy. The periodic cell consisted of 6 layers of Au (Rh) with 9 atoms per layer and greater than 10\AA of vacuum spacing to avoid spurious interactions between periodic images. Given that the nanoparticles are not held in an ultra-high vacuum environment and are exposed to several organic species during

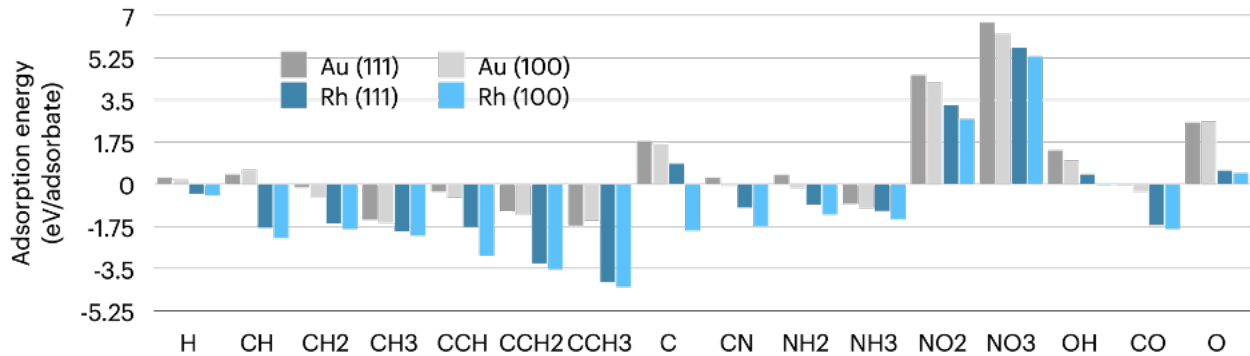


Figure 5.4: Adsorption energy predictions to the (111) and (100) surfaces of Au/Rh from the Open Catalysis Project’s adsorption prediction tool[200–202]. These adsorption energies are predictions based on a large dataset of adsorption on surfaces calculated with DFT. Adsorption energy calculations are referenced to stable gas molecules.

their synthesis, their surfaces are likely coated with passivating adsorbates. Organic species with the elements containing C, H, N, and O may coat the surface due to the presence of polystyrene and poly(2-vinyl pyridine) and flowing hydrogen and oxygen gas. The correction to the total surface energy due to the surface passivation is represented with the terms $\alpha_{\text{Passivation}}$ and $\beta_{\text{Passivation}}$.

$$\alpha = \frac{E(\text{Au}_{54}) - 54E(\text{Au})}{2 \times (0.295\text{nm}^2) \times 9} + \alpha_{\text{passivation}} = 3.5 \frac{\text{eV}}{\text{nm}^2} + \alpha_{\text{passivation}} \quad (5.9)$$

$$\beta = \frac{E(\text{Rh}_{54}) - 54E(\text{Rh})}{2 \times (0.269\text{nm}^2) \times 9} + \beta_{\text{passivation}} = 12.0 \frac{\text{eV}}{\text{nm}^2} + \beta_{\text{passivation}} \quad (5.10)$$

The passivation on each surface depends on many factors, including the surface composition, surface facet, adsorbate species and the chemical potential of the adsorbate. To estimate the magnitude of the surface passivation energy, several potential species that may contribute to the passivation of the Au and Rh surfaces were considered. Predictions for adsorption energies on the (111) and (100) surfaces of each species were made using the Open Catalysis Project’s adsorption prediction tool[200–202], as shown in Fig. 5.4. Each of the adsorbate species presented in Figure 5.4 are adsorbed to a pristine surface and are in their most favorable position of all the tested adsorption sites (on-top, hollow, bridging).

In general, Rh has stronger interactions with adsorbates than Au due to the general inertness of Au. Additionally, the adsorption energies to each surface are correlated, with adsorbates typically binding more strongly to the (100) surface than the (111) surface. Species that have a more negative adsorption energy, like CH_3 and CCH_3 , are more likely to adsorb to the surface than those with weak or positive adsorption energies. Here, CH_3 is used as a model adsorbate to show that the energy change due to adsorption can be large enough to induce a phase transformation from the core-shell geometry to the heterodimer or alloy

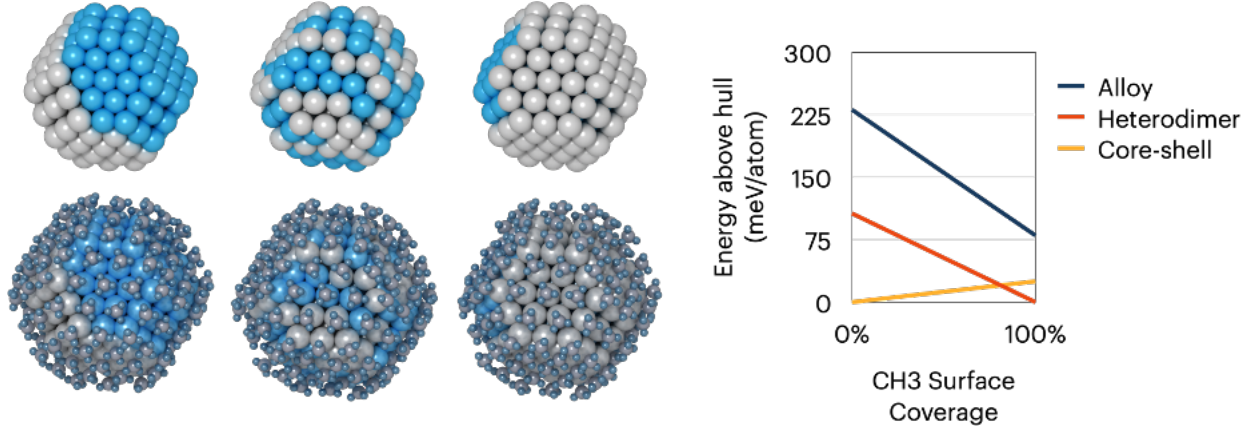


Figure 5.5: DFT calculations of $\text{Au}_{101}\text{Rh}_{100}$ (201-atom) nanoparticles with alloy, heterodimer, and core-shell geometries with and without a CH_3 adsorbate show a surface-environment induced phase transformation to the heterodimer geometry from the core-shell geometry. Temperature, 0K.

geometry. In a calculation of $\text{Au}_{101}\text{Rh}_{100}$ (201-atom) nanoparticles, the core-shell phase is most favorable in a vacuum environment, but the heterodimer phase is most stable when coated with CH_3 (Fig. 5.5).

To estimate γ , a periodic cell of 8 layers of Au and 8 layers of Rh with 9 atoms per layer and the (111) planes separating Au and Rh was modeled with DFT and compared with the bulk phases of Au and Rh. Two equivalent (111) Au-Rh interfaces are created in the periodic cell, each having a surface of 9 atoms. The surface energy is determined by subtracting the bulk energy of the same atoms from the total energy and dividing by the total surface area of the interfaces. An average of the Au and Rh primitive lattice parameters, 0.282 nm, was used as the average distance between nearest neighbor atoms.

$$\gamma = \frac{E(\text{Au}_{72}\text{Rh}_{72}) - 72E(\text{Au}) - 72E(\text{Rh})}{2 \times (0.282\text{nm}^2 \times 9)} = 7.2 \frac{\text{eV}}{\text{nm}^2} \quad (5.11)$$

To calculate the regular solution interaction parameter, w , the L1_2 geometry for various compositions and volumes of Au and Rh was constructed and calculated with DFT (Fig. 5.6), giving an estimate for the ΔH_{bulk} (Eq. 5.4). w is estimated to be 0.13 eV.

It should be noted that although this continuum model highlights the potential influence of the surface-environmental interactions during synthesis on nanoparticle miscibility, the real situation is more complicated than this simplified model. The model assumes a homogeneous distribution of different elements in each single phase and no structural relaxation to mitigate lattice strain. At ultrasmall sizes, nanoparticles are able to resolve lattice strain more than in the bulk. Additionally, the particles are assumed to be perfectly spherical, while the synthesized AuRh particles were not perfectly spherical. The bulk crystal structure is assumed to be face-centered cubic, while real nanoparticles sometimes adopt icosahedral

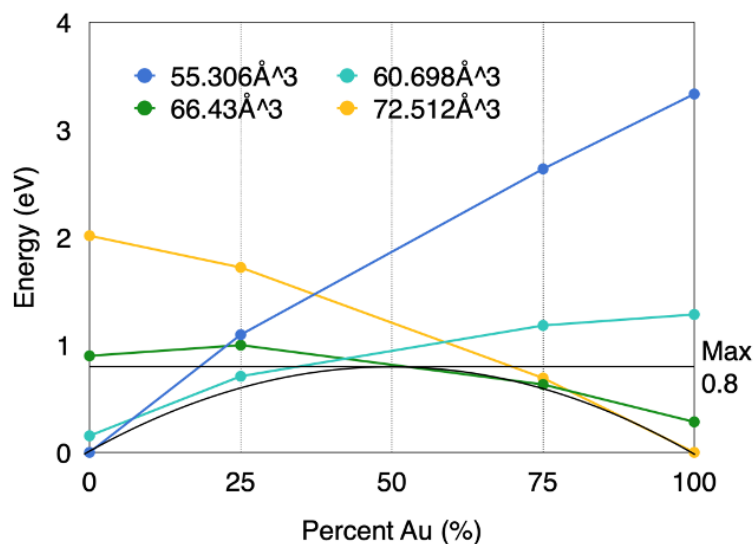


Figure 5.6: The energy of the face-centered cubic $L1_2$ geometry as a function of composition for various volumes. The regular solution interaction parameter, w , can be calculated from this data and Eq. S4. The $L1_2$ geometry has 4 atoms per unit cell, 12 nearest neighbors per atom, and the enthalpy of mixing can be estimated from the energy hull of these curves to be 0.8 eV with a composition of 50% Au and 50% Rh. The regular solution interaction parameter for Au-Rh, w , is estimated to be 0.13 eV.

atomic packing at ultrasmall sizes. The AuRh particles synthesized here appeared to adopt face-centered cubic crystal packing, with some defects and surface reconstruction. Finally, the surface energies are approximated by the total energy and adsorption energies of passivating species to the (111) facet, while the (100) facet is also expected to be a minor facet in a cuboctahedral nanoparticle geometry. Future work may endeavor to increase the complexity of the model and address these shortcomings.

Theoretical Au-Rh Nanoparticle Phase Diagrams

From the computed interfacial, surface and bulk energetics for the Au-Rh system and the thermodynamic relationships that govern the stabilities of each phase, a theoretical phase diagram can be constructed with size and composition determining the phase. The result confirms the size-dependent stability of each configuration in the Au-Rh nanoparticle system in agreement with the particles synthesized experimentally (Fig. 5.7). A smaller particle size leads to an enhanced surface effect that suppresses the mixing enthalpy towards a more negative value and promotes alloying, whereas an equimolar elemental ratio results in a maximized repulsion energy between Au-Rh and facilitates phase separation. The alloying is also promoted by configurational entropy. However, the entropy change from separated to alloyed states is relatively small compared with the variation in enthalpy from bulk Au-Rh

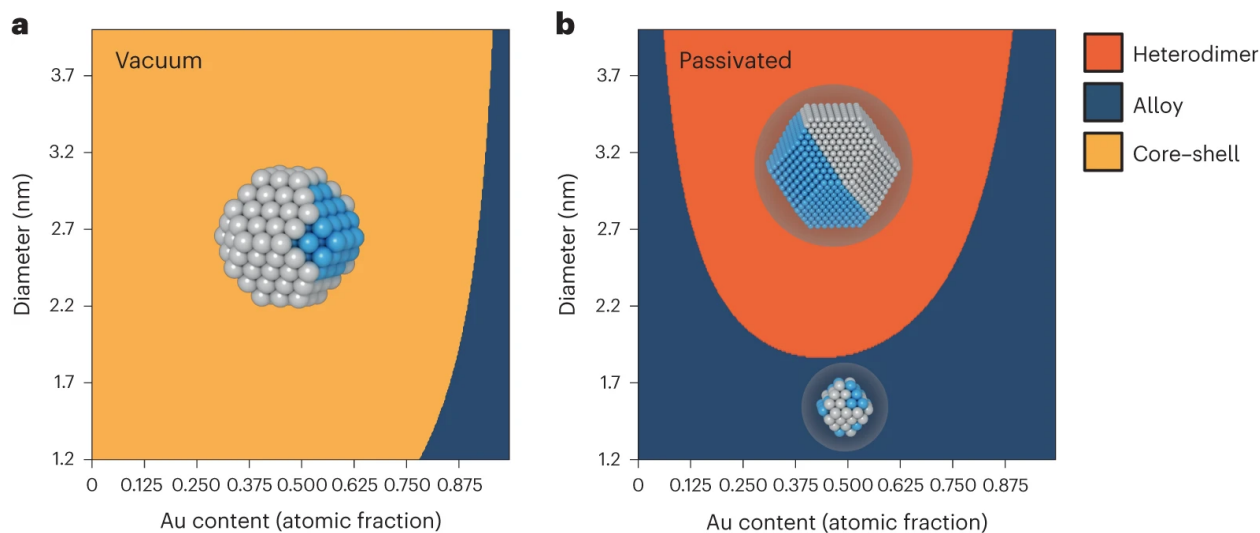


Figure 5.7: a. Size-dependent phase diagram expected for Au–Rh particles in ultrahigh-vacuum environments. Yellow phase, core–shell; dark-blue phase, alloy. b, Size-dependent phase diagram expected with passivated surfaces of Au–Rh. Red phase, heterostructure; dark-blue phase, alloy. Each diagram is for particles at 500 °C. Figs. 5.8 and 5.9 show the phase diagrams for the system with different passivation strengths and at variable temperatures. The inset shows models of core–shell, heterodimer and alloy configurations; the grey atoms are Au and the blue atoms are Rh. The theoretical phase diagram with passivated surfaces matches well with the diagram in Fig. 5.1

to ultrasmall particles (Fig. 5.2), rendering entropy to be a minor factor in determining the mixing state. Additionally, we find that the phase diagram is critically dependent on the passivating environment, and as such, we show the phase diagram in a vacuum environment (Fig. 5.7a) and in a passivated environment (Fig. 5.7b). The theoretical phase diagram for a nanoparticle in a passivated environment (Fig. 5.7b) matches well with the observations seen experimentally (Fig. 5.1).

In a vacuum environment, the surface energy difference for Au and Rh is calculated to be -9.8 eV/nm^2 . With this value, the model predicts that Au–Rh particles would strongly favour the core-shell character with Au enriched on the surface (Fig. 5.7a). However, during synthesis, organic species may adsorb to the undercoordinated surface atoms, and probably remain even though the nanoparticles are plasma-cleaned in O_2 and re-annealed in H_2 . Although the bare surface energy of Au is lower than that of Rh, adsorbates tend to bind more strongly to Rh than Au surfaces (Fig. 5.4). Therefore, surface passivation has the effect of reducing the difference in surface energies of each element, thereby destabilizing the core-shell phase and inducing a phase transformation from the core-shell to heterodimer or alloy geometry (Fig. 5.7, Fig. 5.5, and Fig. 5.8). According to a screening of several possible adsorbates, there are several organic adsorbates that bind strongly enough to each surface

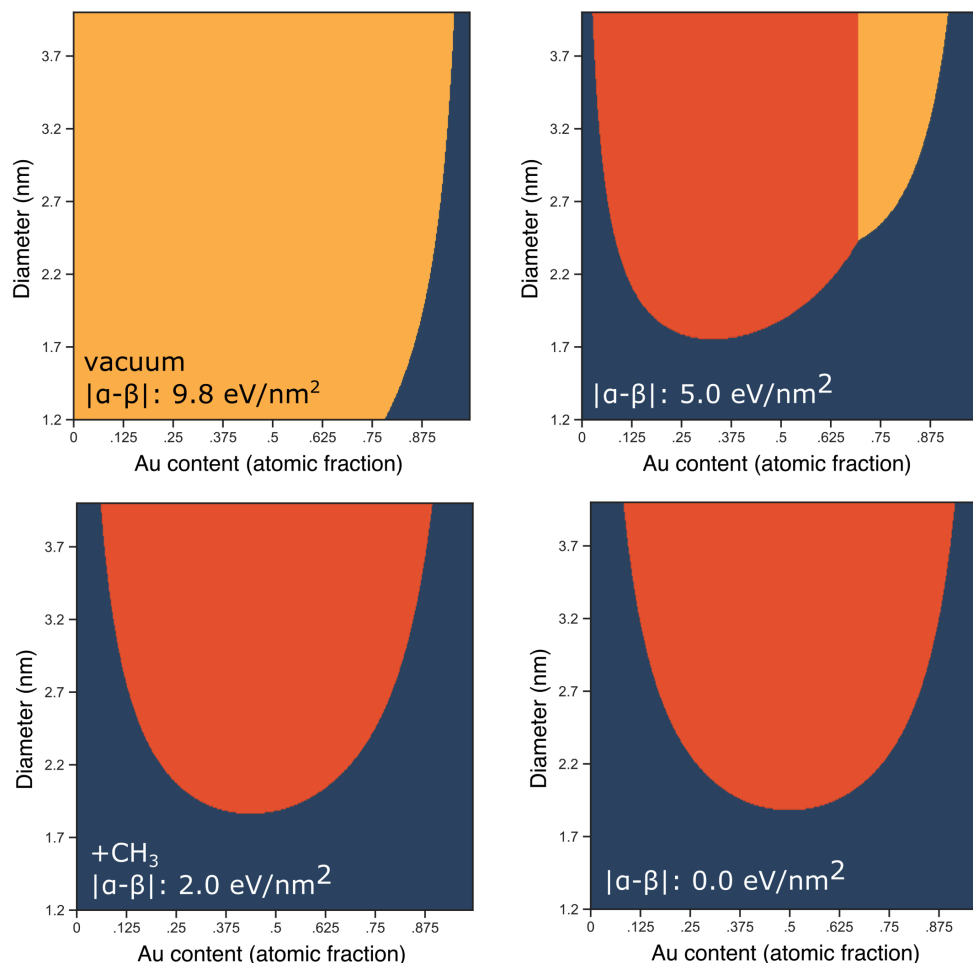


Figure 5.8: Effect of passivation strength on the size-dependent phase diagram of Au-Rh. From top left to bottom right, the differences in Au/Rh surface energies ($|\alpha - \beta|$) are 9.8 eV/nm², 5.0 eV/nm², 2.0 eV/nm², and 0.0 eV/nm². Temperature, 500 °C. Red phase: heterodimer; Blue phase: alloy; Yellow phase: core-shell.

to induce this transformation (Fig. 5.4 and Fig. 5.8). The predicted equilibrium structure of passivated ultrasmall Au-Rh nanoparticles at 500 °C is presented in Fig. 5.7b, which is in good agreement with the experimental findings.

Since the particles were held at temperatures in the range of 25°C-500°C over the course of their synthesis, we show how the phase diagram is modified at different temperatures in Fig. 5.9. While the phase boundary between the heterodimer and alloy phases moves to larger sizes with higher temperature, the overall shape of the phase diagram is largely the same at various temperatures.

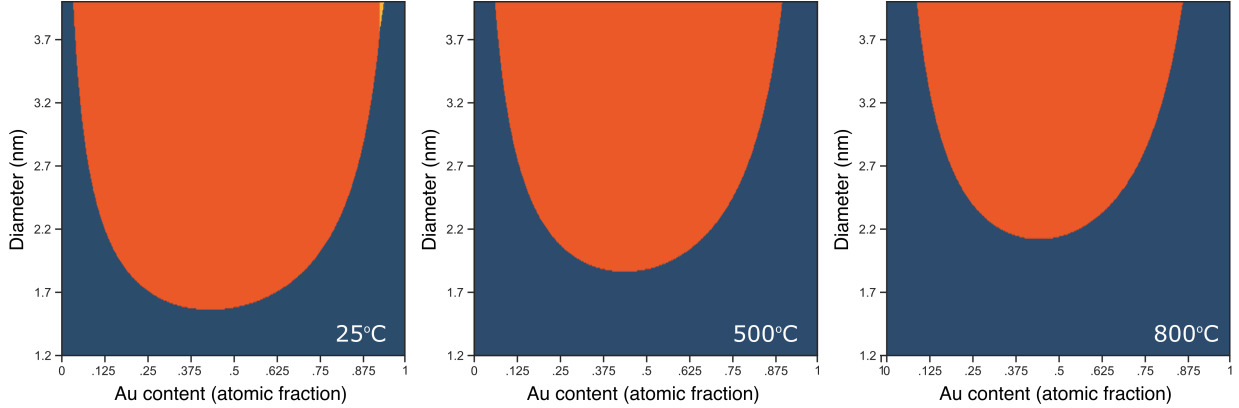


Figure 5.9: Effect of temperature on the size-dependent phase diagram of Au-Rh. From left to right, the temperatures are 25 °C, 500 °C and 800 °C. $|\alpha - \beta| = 2.0$ eV/nm². Red phase: heterodimer; Dark blue phase: alloy; Yellow phase: core-shell.

5.3 Conclusions

We have systematically explored the phase separation of Au and Rh in a nanoparticle. Despite the high incompatibility between Au and Rh in a bulk material, miniaturizing Au–Rh materials to the nano and cluster size regime can switch their miscibility relationship from immiscible to fully alloyable, as we have demonstrated for sub-2 nm Au–Rh alloy nanoparticles across a broad compositional range. We have found that the change in mixing behaviour is affected by particle size, composition and surface passivation. Surface passivation reduces the relative energy of Rh with respect to Au, destabilizing the core–shell geometries and instead favouring the heterodimer and alloy phases. In passivating environments, a thermodynamic model parametrized by DFT calculations validates that Au and Rh will alloy at ultrasmall sizes. Our work quantitatively proves that the bulk phase diagram does not necessarily apply to nanoscale materials. The experimental results call for the exploration of the phase separation behaviour of multielement nanosystems, before conclusively interpreting their thermodynamic structure. Understanding the thermodynamic behaviour of multielement nanoparticles will open up the ability to engineer the structures and properties of multielement nanoparticles for real-life applications.

5.4 Methods: DFT calculations

All the DFT calculations were performed with the Vienna ab initio simulation package 6,[114] with the generalized gradient approximation and the Perdew-Burke-Ernzerhof exchange-correlation functional, the projector augmented wave method[115, 116] and spin polarization. All the calculations of bulk phases were performed with a Brillouin-zone sampling of

$10 \times 10 \times 10$. Slab and interface calculations were performed with a Brillouin-zone sampling of $4 \times 4 \times 1$, with the longest cell dimension having a sampling of 1. To avoid spurious interactions in the periodic boundary conditions, all the distances between non-interacting surfaces were set to be greater than 10 \AA with vacuum separation. The DFT-calculated values of the Au-Rh system, including surface energy, interfacial energy and interaction parameters, were used to evaluate the total energy of the nanoparticles of different sizes, compositions and configurations.

Bibliography

- [1] Yang, R. X.; McCandler, C. A.; Andriuc, O.; Siron, M.; Woods-Robinson, R.; Horton, M. K.; Persson, K. A. Big Data in a Nano World: A Review on Computational, Data-Driven Design of Nanomaterials Structures, Properties, and Synthesis. *ACS Nano* **2022**, *16*, 19873–19891.
- [2] McCandler, C. A.; Dahl, J. C.; Persson, K. A. Phosphine-Stabilized Hidden Ground States in Gold Clusters Investigated via a Au(PH₃)_m Database. *ACS Nano* **2023**, *17*, 1012–1021.
- [3] McCandler, C.; Pihlajamäki, A.; Malola, S.; Häkkinen, H.; Persson, K. Gold-Thiolate Nanocluster Dynamics and Intercluster Reactions Enabled by a Machine Learned Interatomic Potential. 2024; <https://chemrxiv.org/engage/chemrxiv/article-details/65e774a466c138172943fb87>.
- [4] Chen, P.-C.; Gao, M.; McCandler, C. A.; Song, C.; Jin, J.; Yang, Y.; Maulana, A. L.; Persson, K. A.; Yang, P. Complete miscibility of immiscible elements at the nanometre scale. *Nat. Nanotechnol.* **2024**, *19*, 775–781.
- [5] Nesbitt, S.; Watson, M.; Golovko, V. B. Size Effect in Hydrogenation of Nitroaromatics Using Support-Immobilized Atomically Precise Gold Clusters. *J. Phys. Chem. C* **2021**, *125*, 3327–3336.
- [6] Omoda, T.; Takano, S.; Tsukuda, T. Toward Controlling the Electronic Structures of Chemically Modified Superatoms of Gold and Silver. *Small* **2021**, *17*, 2001439.
- [7] Soni, A. K.; Joshi, R.; Ningthoujam, R. S. In *Handbook on Synthesis Strategies for Advanced Materials*; Tyagi, A. K., Ningthoujam, R. S., Eds.; Springer Singapore: Singapore, 2021; pp 383–434, Series Title: Indian Institute of Metals Series.
- [8] Wan, X.-K.; Tang, Q.; Yuan, S.-F.; Jiang, D.-e.; Wang, Q.-M. Au₁₉ Nanocluster Featuring a V-Shaped Alkynyl–Gold Motif. *J. Am. Chem. Soc.* **2015**, *137*, 652–655.
- [9] Nesbitt, S. Use of Chemically Synthesised Atomically Precise Gold Nanoclusters in Catalytic Hydrogenation. Ph.D. thesis, University of Canterbury, 2018.

- [10] Piotrowski, M. J.; Piquini, P.; Da Silva, J. L. F. Density functional theory investigation of 3d , 4d , and 5d 13-atom metal clusters. *Phys. Rev. B* **2010**, *81*, 155446.
- [11] Sekhar De, H.; Krishnamurty, S.; Pal, S. Understanding the Reactivity Properties of Au_n (6 ≤ n ≤ 13) Clusters Using Density Functional Theory Based Reactivity Descriptors. *J. Phys. Chem. C* **2010**, *114*, 6690–6703.
- [12] Hakkinen, H.; Landman, U. Gold clusters AuN, 2 ≤ N ≤ 10 and their anions. *Phys. Rev. B* **2000**, *62*, 4.
- [13] Fernández, E. M.; Soler, J. M.; Garzón, I. L.; Balbás, L. C. Trends in the structure and bonding of noble metal clusters. *Phys. Rev. B* **2004**, *70*, 165403.
- [14] Xiao, L.; Wang, L. From planar to three-dimensional structural transition in gold clusters and the spin–orbit coupling effect. *Chem. Phys. Lett.* **2004**, *392*, 452–455.
- [15] Walker, A. V. Structure and energetics of small gold nanoclusters and their positive ions. *J. Chem. Phys.* **2005**, *122*, 094310.
- [16] Dong, Y.; Springborg, M. Global structure optimization study on Au_{2–20}. *Eur. Phys. J. D* **2007**, *43*, 15–18.
- [17] Assadollahzadeh, B.; Schwerdtfeger, P. A systematic search for minimum structures of small gold clusters Au_n (n=2–20) and their electronic properties. *J. Chem. Phys.* **2009**, *131*, 064306.
- [18] Fa, W.; Luo, C.; Dong, J. Bulk fragment and tubelike structures of AuN (N = 2–26). *Phys. Rev. B* **2005**, *72*, 205428.
- [19] Li, X.-B.; Wang, H.-Y.; Yang, X.-D.; Zhu, Z.-H.; Tang, Y.-J. Size dependence of the structures and energetic and electronic properties of gold clusters. *J. Chem. Phys.* **2007**, *126*, 084505.
- [20] Johansson, M. P.; Warnke, I.; Le, A.; Furche, F. At What Size Do Neutral Gold Clusters Turn Three-Dimensional? *J. Phys. Chem. C* **2014**, *118*, 29370–29377.
- [21] Kinaci, A.; Narayanan, B.; Sen, F. G.; Davis, M. J.; Gray, S. K.; Sankaranarayanan, S. K. R. S.; Chan, M. K. Y. Unraveling the Planar-Globular Transition in Gold Nanoclusters through Evolutionary Search. *Sci. Reports* **2016**, *6*, 34974.
- [22] Goldsmith, B. R.; Florian, J.; Liu, J.-X.; Gruene, P.; Lyon, J. T.; Rayner, D. M.; Fielicke, A.; Scheffler, M.; Ghiringhelli, L. M. Two-to-three dimensional transition in neutral gold clusters: The crucial role of van der Waals interactions and temperature. *Phys. Rev. Mater.* **2019**, *3*, 016002.

- [23] Chaves, A. S.; Piotrowski, M. J.; Da Silva, J. L. F. Evolution of the structural, energetic, and electronic properties of the 3d, 4d, and 5d transition-metal clusters (30 TM_n systems for n = 2–15): a density functional theory investigation. *Phys. Chem. Chem. Phys.* **2017**, *19*, 15484–15502.
- [24] Manna, S.; Hernandez, A.; Wang, Y.; Lile, P.; Liu, S.; Mueller, T. A Database of Low-Energy Atomically Precise Nanoclusters. 2021; ChemRxiv. 10.26434/chemrxiv-2021-0fq3q (accessed December 1, 2021).
- [25] Wu, P.; Liu, Q.; Chen, G. Nonlocal effects on the structural transition of gold clusters from planar to three-dimensional geometries. *RSC Adv.* **2019**, *9*, 20989–20999.
- [26] Gilb, S.; Weis, P.; Furche, F.; Ahlrichs, R.; Kappes, M. M. Structures of small gold cluster cations Au⁺_n, n < 14: Ion mobility measurements versus density functional calculations. *J. Chem. Phys.* **2002**, *116*, 8.
- [27] Wang, J.; Wang, G.; Zhao, J. Density-functional study of Au_n (n = 2–20) clusters: Lowest-energy structures and electronic properties. *Phys. Rev. B* **2002**, *66*, 035418.
- [28] Isenberg, N. M.; Taylor, M. G.; Yan, Z.; Hanselman, C. L.; Mpourmpakis, G.; Gounaris, C. E. Identification of optimally stable nanocluster geometries *via* mathematical optimization and density-functional theory. *Mol. Syst. Des. & Eng.* **2020**, *5*, 232–244.
- [29] Shichibu, Y.; Konishi, K. HCl-Induced Nuclearity Convergence in Diphosphine-Protected Ultrasmall Gold Clusters: A Novel Synthetic Route to “Magic-Number” Au₁₃ Clusters. *Small* **2010**, *6*, 1216–1220.
- [30] Johnson, G. E.; Olivares, A.; Hill, D.; Laskin, J. Cationic gold clusters ligated with differently substituted phosphines: effect of substitution on ligand reactivity and binding. *Phys. Chem. Chem. Phys.* **2015**, *17*, 14636–14646.
- [31] Malola, S.; Nieminen, P.; Pihlajamäki, A.; Hämäläinen, J.; Kärkkäinen, T.; Häkkinen, H. A method for structure prediction of metal-ligand interfaces of hybrid nanoparticles. *Nat. Commun.* **2019**, *10*, 3973.
- [32] Loh, N. D.; Sen, S.; Bosman, M.; Tan, S. F.; Zhong, J.; Nijhuis, C. A.; Král, P.; Matsudaira, P.; Mirsaidov, U. Multistep nucleation of nanocrystals in aqueous solution. *Nat. Chem.* **2017**, *9*, 77–82.
- [33] Shi, B. X.; Wales, D. J.; Michaelides, A.; Myung, C. W. Going for Gold(-Standard): Attaining Coupled Cluster Accuracy in Oxide-Supported Nanoclusters. *J. Chem. Theory Comput.* **2024**, *20*, 5306–5316.

- [34] Ghasemi, S. A.; Amsler, M.; Hennig, R. G.; Roy, S.; Goedecker, S.; Lenosky, T. J.; Umrigar, C. J.; Genovese, L.; Morishita, T.; Nishio, K. Energy landscape of silicon systems and its description by force fields, tight binding schemes, density functional methods, and quantum Monte Carlo methods. *Phys. Rev. B* **2010**, *81*, 214107.
- [35] Johnston, R. L. Evolving better nanoparticles: Genetic algorithms for optimising cluster geometries. *Dalton Trans.* **2003**, 4193–4207.
- [36] Wales, D. J.; Doye, J. P. K. Global Optimization by Basin-Hopping and the Lowest Energy Structures of Lennard-Jones Clusters Containing up to 110 Atoms. *J. Phys. Chem. A* **1997**, *101*, 5111–5116.
- [37] Pickard, C. J.; Needs, R. J. Ab initio random structure searching. *J. Physics: Condens. Matter* **2011**, *23*, 053201.
- [38] Pannetier, J.; Bassas-Alsina, J.; Rodriguez-Carvajal, J.; Caignaert, V. Prediction of crystal structures from crystal chemistry rules by simulated annealing. *Nature* **1990**, *346*, 343–345.
- [39] Wang, Y.; Lv, J.; Zhu, L.; Ma, Y. Crystal structure prediction via particle-swarm optimization. *Phys. Rev. B* **2010**, *82*, 094116.
- [40] Chen, M.; Dixon, D. A. Tree Growth—Hybrid Genetic Algorithm for Predicting the Structure of Small (TiO₂)_n, n = 2–13, Nanoclusters. *J. Chem. Theory Comput.* **2013**, *9*, 3189–3200.
- [41] Glover, F. Tabu Search—Part I. *ORSA J. on Comput.* **1989**, *1*, 190–206.
- [42] Tan, L.; Pickard, C. J.; Yu, K.; Sapelkin, A.; Misquitta, A. J.; Dove, M. T. Structures of CdSe and CdS Nanoclusters from Ab Initio Random Structure Searching. *J. Phys. Chem. C* **2019**, *123*, 29370–29378.
- [43] Ciobanu, C. V.; Wang, C.-Z.; Ho, K.-M. *Atomic Structure Prediction of Nanostructures, Clusters and Surfaces*; Wiley-VCH, 2012.
- [44] Rossi, G.; Ferrando, R. Searching for low-energy structures of nanoparticles: a comparison of different methods and algorithms. *J. Physics: Condens. Matter* **2009**, *21*, 084208.
- [45] Woodley, S. M.; Day, G. M.; Catlow, R. Structure prediction of crystals, surfaces and nanoparticles. *Philos. Trans. Royal Soc. A: Math. Phys. Eng. Sci.* **2020**, *378*, 20190600.
- [46] Marom, N.; Kim, M.; Chelikowsky, J. R. Structure Selection Based on High Vertical Electron Affinity for TiO₂ Clusters. *Phys. Rev. Lett.* **2012**, *108*, 106801.

- [47] Bhattacharya, S.; Sonin, B. H.; Jumonville, C. J.; Ghiringhelli, L. M.; Marom, N. Computational design of nanoclusters by property-based genetic algorithms: Tuning the electronic properties of (TiO₂)_n clusters. *Phys. Rev. B* **2015**, *91*, 241115.
- [48] Sokol, A. A.; Catlow, C. R. A.; Miskufova, M.; Shevlin, S. A.; Al-Sunaidi, A. A.; Walsh, A.; Woodley, S. M. On the problem of cluster structure diversity and the value of data mining. *Phys. Chem. Chem. Phys.* **2010**, *12*, 8438.
- [49] Manna, S.; Wang, Y.; Hernandez, A.; Lile, P.; Liu, S.; Mueller, T. A database of low-energy atomically precise nanoclusters. *Sci. Data* **2023**, *10*, 308.
- [50] Chaves, A. S.; Rondina, G. G.; Piotrowski, M. J.; Tereshchuk, P.; Da Silva, J. L. F. The Role of Charge States in the Atomic Structure of Cun and Ptn (n = 2–14 atoms) Clusters: A DFT Investigation. *J. Phys. Chem. A* **2014**, *118*, 10813–10821.
- [51] Rondina, G. G.; Da Silva, J. L. F. Revised Basin-Hopping Monte Carlo Algorithm for Structure Optimization of Clusters and Nanoparticles. *J. Chem. Inf. Model.* **2013**, *53*, 2282–2298.
- [52] Zuo, Y.; Chen, C.; Li, X.; Deng, Z.; Chen, Y.; Behler, J.; Csányi, G.; Shapeev, A. V.; Thompson, A. P.; Wood, M. A.; Ong, S. P. Performance and Cost Assessment of Machine Learning Interatomic Potentials. *J. Phys. Chem. A* **2020**, *124*, 731–745.
- [53] Weinreich, J.; Römer, A.; Paleico, M. L.; Behler, J. Properties of α -Brass Nanoparticles. 1. Neural Network Potential Energy Surface. *J. Phys. Chem. C* **2020**, *124*, 12682–12695.
- [54] Lysogorskiy, Y.; Oord, C. v. d.; Bochkarev, A.; Menon, S.; Rinaldi, M.; Hammer-schmidt, T.; Mrovec, M.; Thompson, A.; Csányi, G.; Ortner, C.; Drautz, R. Performant implementation of the atomic cluster expansion (PACE) and application to copper and silicon. *npj Comput. Mater.* **2021**, *7*, 1–12.
- [55] Loeffler, T. D.; Manna, S.; Patra, T. K.; Chan, H.; Narayanan, B.; Sankara-narayanan, S. Active Learning A Neural Network Model For Gold Clusters & Bulk From Sparse First Principles Training Data. *ChemCatChem* **2020**, *12*, 4796–4806.
- [56] Cao, L.; Li, C.; Mueller, T. The Use of Cluster Expansions To Predict the Structures and Properties of Surfaces and Nanostructured Materials. *J. Chem. Inf. Model.* **2018**, *58*, 2401–2413.
- [57] Li, C.; Raciti, D.; Pu, T.; Cao, L.; He, C.; Wang, C.; Mueller, T. Improved Prediction of Nanoalloy Structures by the Explicit Inclusion of Adsorbates in Cluster Expansions. *J. Phys. Chem. C* **2018**, *122*, 18040–18047.
- [58] Drautz, R. Atomic cluster expansion for accurate and transferable interatomic potentials. *Phys. Rev. B* **2019**, *99*, 014104.

- [59] Batzner, S.; Musaelian, A.; Sun, L.; Geiger, M.; Mailoa, J. P.; Kornbluth, M.; Molinari, N.; Smidt, T. E.; Kozinsky, B. E(3)-Equivariant Graph Neural Networks for Data-Efficient and Accurate Interatomic Potentials. *Nat. Commun.* **2022**, *13*, 2453.
- [60] Musaelian, A.; Batzner, S.; Johansson, A.; Sun, L.; Owen, C. J.; Kornbluth, M.; Kozinsky, B. Learning local equivariant representations for large-scale atomistic dynamics. *Nat. Commun.* **2023**, *14*, 579.
- [61] Batatia, I.; Kovacs, D. P.; Simm, G. N. C.; Ortner, C.; Csanyi, G. MACE: Higher Order Equivariant Message Passing Neural Networks for Fast and Accurate Force Fields. 2022.
- [62] Tadmor, E. B.; Elliott, R. S.; Sethna, J. P.; Miller, R. E.; Becker, C. A. The potential of atomistic simulations and the knowledgebase of interatomic models. *JOM* **2011**, *63*, 17–17.
- [63] Becker, C. A.; Tavazza, F.; Trautt, Z. T.; Buarque de Macedo, R. A. Considerations for choosing and using force fields and interatomic potentials in materials science and engineering. *Curr. Opin. Solid State Mater. Sci.* **2013**, *17*, 277–283.
- [64] Hale, L. M.; Trautt, Z. T.; Becker, C. A. Evaluating variability with atomistic simulations: the effect of potential and calculation methodology on the modeling of lattice and elastic constants. *Model. Simul. Mater. Sci. Eng.* **2018**, *26*, 055003.
- [65] McPartlin, M.; Mason, R.; Malatesta, L. Novel cluster complexes of gold(0)–gold(I). *J. Chem. Soc. D* **1969**, *0*, 334–334.
- [66] Jin, R.; Zeng, C.; Zhou, M.; Chen, Y. Atomically Precise Colloidal Metal Nanoclusters and Nanoparticles: Fundamentals and Opportunities. *Chem. Rev.* **2016**, *116*, 10346–10413.
- [67] Azubel, M.; Koivisto, J.; Malola, S.; Bushnell, D.; Hura, G. L.; Koh, A. L.; Tsunoyama, H.; Tsukuda, T.; Pettersson, M.; Häkkinen, H.; Kornberg, R. D. Electron microscopy of gold nanoparticles at atomic resolution. *Science* **2014**, *345*, 909–912.
- [68] Li, S.; Tian, W.; Liu, Y. The ligand effect of atomically precise gold nanoclusters in tailoring catalytic properties. *Nanoscale* **2021**, *13*, 16847–16859.
- [69] Pettibone, J. M.; Hudgens, J. W. Gold Cluster Formation with Phosphine Ligands: Etching as a Size-Selective Synthetic Pathway for Small Clusters? *ACS Nano* **2011**, *5*, 2989–3002.
- [70] Spivey, K.; Williams, J. I.; Wang, L. Structures of undecagold clusters: Ligand effect. *Chem. Phys. Lett.* **2006**, *432*, 163–166.

- [71] Shafai, G.; Hong, S.; Bertino, M.; Rahman, T. S. Effect of Ligands on the Geometric and Electronic Structure of Au₁₃ Clusters. *J. Phys. Chem. C* **2009**, *113*, 12072–12078.
- [72] Burgos, J. C.; Mejía, S. M.; Metha, G. F. Effect of Charge and Phosphine Ligands on the Electronic Structure of the Au₈ Cluster. *ACS Omega* **2019**, *4*, 9169–9180.
- [73] Periyasamy, G.; Remacle, F. Ligand and Solvation Effects on the Electronic Properties of Au₅₅ Clusters: A Density Functional Theory Study. *Nano Lett.* **2009**, *9*, 3007–3011.
- [74] Hong, S.; Shafai, G.; Bertino, M.; Rahman, T. S. Toward an Understanding of Ligand Selectivity in Nanocluster Synthesis. *J. Phys. Chem. C* **2011**, *115*, 14478–14487.
- [75] Ligare, M. R.; Johnson, G. E.; Laskin, J. Observing the real time formation of phosphine-ligated gold clusters by electrospray ionization mass spectrometry. *Phys. Chem. Chem. Phys.* **2017**, *19*, 17187–17198.
- [76] Luo, Z.; Castleman, A. W. Special and General Superatoms. *Accounts Chem. Res.* **2014**, *47*, 2931–2940.
- [77] Groom, C. R.; Bruno, I. J.; Lightfoot, M. P.; Ward, S. C. The Cambridge Structural Database. *Acta Crystallogr. Sect. B: Struct. Sci. Cryst. Eng. Mater.* **2016**, *72*, 171–179.
- [78] Ivanov, S. A.; Arachchige, I.; Aikens, C. M. Density Functional Analysis of Geometries and Electronic Structures of Gold-Phosphine Clusters. The Case of Au₄(PR₃)₄²⁺ and Au₄(μ₂-I)₂(PR₃)₄. *J. Phys. Chem. A* **2011**, *115*, 8017–8031.
- [79] Qiu, Y. Q.; Qin, C. S.; Su, Z. M.; Yang, G. C.; Pan, X. M.; Wang, R. S. DFT/FF study on electronic structure and second-order NLO property of dinuclear gold complex [Au(SeC₂B₁₀H₁₁)(PPh₃)]₂. *Synth. Met.* **2005**, *152*, 273–276.
- [80] Chen, X.; Wu, K.; Snijders, J. G.; Lin, C. Electronic Structures and Nonlinear Optical Properties of Trinuclear Transition Metal Clusters M-(μ-S)-M' (M = Mo, W; M' = Cu, Ag, Au). *Inorg. Chem.* **2003**, *42*, 532–540.
- [81] Häberlen, O. D.; Chung, S.-C.; Rösch, N.; Rösch, N. Relativistic density-functional studies of naked and ligated gold clusters. *Int. J. Quantum Chem.* **1994**, *52*, 595–610.
- [82] Häberlen, O. D.; Roesch, N. Effect of phosphine substituents in gold(I) complexes: a theoretical study of MeAuPR₃, R = H, Me, Ph. *J. Phys. Chem.* **1993**, *97*, 4970–4973.
- [83] Chase, M. W., Jr. *NIST-JANAF Thermochemical Tables, Monograph 9*, 4th ed.; J. Phys. Chem. Ref. Data, 1998; pp 1–1951.
- [84] Bakar, M. A.; Sugiuchi, M.; Iwasaki, M.; Shichibu, Y.; Konishi, K. Hydrogen bonds to Au atoms in coordinated gold clusters. *Nat. Commun.* **2017**, *8*, 576.

- [85] Shichibu, Y.; Zhang, M.; Kamei, Y.; Konishi, K. $[\text{Au}_7]^{3+}$: A Missing Link in the Four-Electron Gold Cluster Family. *J. Am. Chem. Soc.* **2014**, *136*, 12892–12895.
- [86] Shichibu, Y.; Kamei, Y.; Konishi, K. Unique [core+two] structure and optical property of a dodeca-ligated undecagold cluster: critical contribution of the exo gold atoms to the electronic structure. *Chem. Commun.* **2012**, *48*, 7559–7561.
- [87] Susukida, K.; Lugo-Fuentes, L. I.; Matsumae, S.; Nakanishi, K.; Nakamoto, M.; Yamamoto, Y.; Shang, R.; Barroso-Flores, J.; Jimenez-Halla, J. O. C. CCDC 2023935: Experimental Crystal Structure Determination. 2020.
- [88] Schulz-Dobrick, M.; Jansen, M. CCDC 668368: Experimental Crystal Structure Determination. 2008.
- [89] Marsh, R. E. Crystal structure of $\text{Au}_7(\text{PPh}_3)_7^+$: corrigendum. *Inorg. Chem.* **1984**, *23*, 3682–3682.
- [90] Van der Velden, J. W. A.; Beurskens, P. T.; Bour, J. J.; Bosman, W. P.; Noordik, J. H.; Kolenbrander, M.; Buskes, J. A. K. M. Intermediates in the formation of gold clusters. Preparation and x-ray analysis of $[\text{Au}_7(\text{PPh}_3)_7]^+$ and synthesis and characterization of $[\text{Au}_8(\text{PPh}_3)_6\text{I}]\text{PF}_6$. *Inorg. Chem.* **1984**, *23*, 146–151.
- [91] Marsh, R. E. Some thoughts on choosing the correct space group. *Acta Crystallogr. Sect. B: Struct. Sci.* **1995**, *51*, 897–907.
- [92] Yang, Y.; Sharp, P. R. New Gold Clusters $[\text{Au}_8\text{L}_6](\text{BF}_4)_2$ and $[(\text{AuL})_4](\text{BF}_4)_2$ ($\text{L} = \text{P}(\text{mesityl})_3$). *J. Am. Chem. Soc.* **1994**, *116*, 6983–6984.
- [93] Zeller, E.; Beruda, H.; Schmidbaur, H. Tetrahedral gold cluster $[\text{Au}_4]^{2+}$: crystal structure of $\{[(\text{tert-Bu})_3\text{PAu}]_4\}^{2+}(\text{BF}_4)_2 \cdot 2\text{CHCl}_3$. *Inorg. Chem.* **1993**, *32*, 3203–3204.
- [94] Briant, C. E.; Hall, K. P.; Mingos, D. M. P.; Wheeler, A. C. Synthesis and structural characterisation of hexakis(triphenyl phosphine)hexagold(2+) nitrate, $[\text{Au}_6(\text{PPh}_3)_6][\text{NO}_3]_2$, and related clusters with edgesharing bitetrahedral geometries. *J. Chem. Soc. Dalton Trans.* **1986**, 687–692.
- [95] Bellon, P.; Manassero, M.; Sansoni, M. An octahedral gold cluster: crystal and molecular structure of hexakis[tris-(p-tolyl)phosphine]-octahedro-hexagold bis(tetraphenylborate). *J. Chem. Soc. Dalton Trans.* **1973**, 2423–2427.
- [96] Van der Velden, J. W. A.; Bour, J. J.; Bosman, W. P.; Noordik, J. H. Reactions of cationic gold clusters with Lewis bases. Preparation and x-ray structure investigation of $[\text{Au}_8(\text{PPh}_3)_7](\text{NO}_3)_2 \cdot 2\text{CH}_2\text{Cl}_2$ and $\text{Au}_6(\text{PPh}_3)_4[\text{Co}(\text{CO})_4]_2$. *Inorg. Chem.* **1983**, *22*, 1913–1918.

- [97] Van der Velden, J. W. A.; Bour, J. J.; Bosman, W. P.; Noordik, J. H. Synthesis and X-ray crystal structure determination of the cationic gold cluster compound $[\text{Au}_8(\text{PPh}_3)_7](\text{NO}_3)_2$. *J. Chem. Soc. Chem. Commun.* **1981**, 1218–1219.
- [98] Shen, H.; Selenius, E.; Ruan, P.; Li, X.; Yuan, P.; Lopez-Estrada, O.; Malola, S.; Lin, S.; Teo, B. K.; Häkkinen, H.; Zheng, N. CCDC 1967410: Experimental Crystal Structure Determination. 2020.
- [99] Schulz-Dobrick, M.; Jansen, M. CCDC 615444: Experimental Crystal Structure Determination. 2007.
- [100] Malinina, E.; Drozdova, V.; Bykov, A.; Belousova, O.; Polyakova, I.; Zhizhin, K.; Kuznetsov, N. CCDC 687192: Experimental Crystal Structure Determination. 2008.
- [101] Smits, J. M. M.; Beurskens, P. T.; Bour, J. J.; Vollenbroek, F. A. X-ray analysis of octakis(tri-*p*-tolylphosphine) enneagoldtris(hexafluorophosphate), $[\text{Au}_9\{\text{P}(\text{p-MeC}_6\text{H}_4)_3\}_8](\text{PF}_6)_3$: A redetermination. *J. Crystallogr. Spectrosc. Res.* **1983**, 13, 365–372.
- [102] Schulz-Dobrick, M.; Jansen, M. CCDC 690419: Experimental Crystal Structure Determination. 2009.
- [103] Schulz-Dobrick, M.; Jansen, M. CCDC 690422: Experimental Crystal Structure Determination. 2009.
- [104] Schulz-Dobrick, M.; Jansen, M. CCDC 615445: Experimental Crystal Structure Determination. 2007.
- [105] Schulz-Dobrick, M.; Jansen, M. CCDC 690418: Experimental Crystal Structure Determination. 2009.
- [106] Wang, J.-Q.; Guan, Z.-J.; Liu, W.-D.; Yang, Y.; Wang, Q.-M. CCDC 1895800: Experimental Crystal Structure Determination. 2019.
- [107] Wang, J.-Q.; Guan, Z.-J.; Liu, W.-D.; Yang, Y.; Wang, Q.-M. CCDC 1895797: Experimental Crystal Structure Determination. 2019.
- [108] Mundy, J. A. et al. Liberating a hidden antiferroelectric phase with interfacial electrostatic engineering. *Sci. Adv.* **2022**, 8, eabg5860.
- [109] Xiao, L.; Tollberg, B.; Hu, X.; Wang, L. Structural study of gold clusters. *J. Chem. Phys.* **2006**, 124, 114309.
- [110] Pyykko, P. Relativistic effects in structural chemistry. *Chem. Rev.* **1988**, 88, 563–594.
- [111] Grönbeck, H.; Broqvist, P. Comparison of the bonding in Au_8 and Cu_8 : A density functional theory study. *Phys. Rev. B* **2005**, 71, 073408.

- [112] Bonačić-Koutecký, V.; Burda, J.; Mitrić, R.; Ge, M.; Zampella, G.; Fantucci, P. Density functional study of structural and electronic properties of bimetallic silver–gold clusters: Comparison with pure gold and silver clusters. *J. Chem. Phys.* **2002**, *117*, 3120–3131.
- [113] Zhao, J.; Yang, J.; Hou, J. G. Theoretical study of small two-dimensional gold clusters. *Phys. Rev. B* **2003**, *67*, 085404.
- [114] Kresse, G.; Furthmüller, J. Efficient iterative schemes for ab initio total-energy calculations using a plane-wave basis set. *Phys. Rev. B* **1996**, *54*, 11169–11186.
- [115] Kresse, G.; Joubert, D. From ultrasoft pseudopotentials to the projector augmented-wave method. *Phys. Rev. B* **1999**, *59*, 1758–1775.
- [116] Perdew, J. P.; Burke, K.; Ernzerhof, M. Generalized Gradient Approximation Made Simple. *Phys. Rev. Lett.* **1996**, *77*, 3865–3868.
- [117] Narayanan, B.; Kinaci, A.; Sen, F. G.; Davis, M. J.; Gray, S. K.; Chan, M. K. Y.; Sankaranarayanan, S. K. R. S. Describing the Diverse Geometries of Gold from Nanoclusters to Bulk—A First-Principles-Based Hybrid Bond-Order Potential. *J. Phys. Chem. C* **2016**, *120*, 13787–13800.
- [118] Hussain, A.; Muller, A. J.; Nieuwenhuys, B. E.; Gracia, J. M.; Niemantsverdriet, J. W. Two Gold Surfaces and a Cluster with Remarkable Reactivity for CO Oxidation, a Density Functional Theory Study. *Top. Catal.* **2011**, *54*, 415–423.
- [119] Grimme, S.; Antony, J.; Ehrlich, S.; Krieg, H. A consistent and accurate ab initio parametrization of density functional dispersion correction (DFT-D) for the 94 elements H–Pu. *J. Chem. Phys.* **2010**, *132*, 154104.
- [120] Häkkinen, H.; Moseler, M.; Landman, U. Bonding in Cu, Ag, and Au Clusters: Relativistic Effects, Trends, and Surprises. *Phys. Rev. Lett.* **2002**, *89*, 033401.
- [121] Xiong, X.-G.; Xu, W.-H.; Li, J.; Pyykkö, P. Aspects of bonding in small gold clusters. *Int. J. Mass Spectrom.* **2013**, *354–355*, 15–18.
- [122] Tsukuda, T.; Häkkinen, H. *Protected Metal Clusters: From Fundamentals to Applications*, 1st ed.; Elsevier: Amsterdam, 2015; Vol. 9.
- [123] Jin, R.; Zeng, C.; Zhou, M.; Chen, Y. Atomically Precise Colloidal Metal Nanoclusters and Nanoparticles: Fundamentals and Opportunities. *Chem. Rev.* **2016**, *116*, 10346–10413.
- [124] Chakraborty, I.; Pradeep, T. Atomically Precise Clusters of Noble Metals: Emerging Link between Atoms and Nanoparticles. *Chem. Rev.* **2017**, *117*, 8208–8271.

- [125] Matus, M. F.; Häkkinen, H. Atomically Precise Gold Nanoclusters: Towards an Optimal Biocompatible System from a Theoretical–Experimental Strategy. *Small* **2021**, *17*, 2005499.
- [126] Matus, M. F.; Häkkinen, H. Understanding ligand-protected noble metal nanoclusters at work. *Nat. Rev. Mater.* **2023**, *8*, 372–389.
- [127] Unke, O. T.; Chmiela, S.; Sauceda, H. E.; Gastegger, M.; Poltavsky, I.; Schütt, K. T.; Tkatchenko, A.; Müller, K.-R. Machine Learning Force Fields. *Chem. Rev.* **2021**, *121*, 10142–10186.
- [128] Noé, F.; Tkatchenko, A.; Müller, K.-R.; Clementi, C. Machine Learning for Molecular Simulation. *Annu. Rev. Phys. Chem.* **2020**, *71*, 361–390.
- [129] Schmidt, J.; Marques, M. R. G.; Botti, S.; Marques, M. A. L. Recent advances and applications of machine learning in solid-state materials science. *npj Comput. Mater.* **2019**, *5*, 83.
- [130] Schleder, G. R.; Padilha, A. C. M.; Acosta, C. M.; Costa, M.; Fazzio, A. From DFT to machine learning: recent approaches to materials science—a review. *J. Phys. Mater.* **2019**, *2*, 032001.
- [131] Friederich, P.; Häse, F.; Proppe, J.; Aspuru-Guzik, A. Machine-learned potentials for next-generation matter simulations. *Nat. Mater.* **2021**, *20*, 750–761.
- [132] Järvi, T. T.; van Duin, A. C. T.; Nordlund, K.; Goddard, W. A. Development of Interatomic ReaxFF Potentials for Au–S–C–H Systems. *J. Phys. Chem. A* **2011**, *115*, 10315–10322.
- [133] Bae, G.-T.; Aikens, C. M. Improved ReaxFF Force Field Parameters for Au–S–C–H Systems. *J. Phys. Chem. A* **2013**, *117*, 10438–10446.
- [134] Pohjolainen, E.; Chen, X.; Malola, S.; Groenhof, G.; Häkkinen, H. A Unified AMBER-Compatible Molecular Mechanics Force Field for Thiolate-Protected Gold Nanoclusters. *J. Chem. Theory Comput.* **2016**, *12*, 1342–1350.
- [135] Pihlajamäki, A.; Hämäläinen, J.; Linja, J.; Nieminen, P.; Malola, S.; Kärkkäinen, T.; Häkkinen, H. Monte Carlo Simulations of Au₃₈(SCH₃)₂₄ Nanocluster Using Distance-Based Machine Learning Methods. *J. Phys. Chem. A* **2020**, *124*, 4827–4836.
- [136] Pihlajamäki, A.; Malola, S.; Kärkkäinen, T.; Häkkinen, H. Orientation Adaptive Minimal Learning Machine: Application to Thiolate-Protected Gold Nanoclusters and Gold-Thiolate Rings. arXiv:2203.09788v2 [physics.comp-ph] (submitted 2022-03-18, accessed 2023-05-26), 2022.

- [137] Chen, S.; Wang, S.; Zhong, J.; Song, Y.; Zhang, J.; Sheng, H.; Pei, Y.; Zhu, M. The Structure and Optical Properties of the [Au₁₈(SR)₁₄] Nanocluster. *Angewandte Chemie Int. Ed.* **2015**, *54*, 3145–3149.
- [138] Yang, S.; Chai, J.; Song, Y.; Fan, J.; Chen, T.; Wang, S.; Yu, H.; Li, X.; Zhu, M. In Situ Two-Phase Ligand Exchange: A New Method for the Synthesis of Alloy Nanoclusters with Precise Atomic Structures. *J. Am. Chem. Soc.* **2017**, *139*, 5668–5671.
- [139] Das, A.; Li, T.; Li, G.; Nobusada, K.; Zeng, C.; Rosi, N. L.; Jin, R. Crystal structure and electronic properties of a thiolate-protected Au₂₄ nanocluster. *Nanoscale* **2014**, *6*, 6458–6462.
- [140] Zhu, M.; Eckenhoff, W. T.; Pintauer, T.; Jin, R. Conversion of Anionic [Au₂₅(SCH₂CH₂Ph)₁₈]- Cluster to Charge Neutral Cluster via Air Oxidation. *J. Phys. Chem. C* **2008**, *112*, 14221–14224.
- [141] Higaki, T.; Liu, C.; Chen, Y.; Zhao, S.; Zeng, C.; Jin, R.; Wang, S.; Rosi, N. L.; Jin, R. Oxidation-Induced Transformation of Eight-Electron Gold Nanoclusters: [Au₂₃(SR)₁₆]- to [Au₂₈(SR)₂₀]0. *J. Phys. Chem. Lett.* **2017**, *8*, 866–870.
- [142] Nimmala, P. R.; Knoppe, S.; Jupally, V. R.; Delcamp, J. H.; Aikens, C. M.; Dass, A. Au₃₆(SPh)₂₄ Nanomolecules: X-ray Crystal Structure, Optical Spectroscopy, Electrochemistry, and Theoretical Analysis. *J. Phys. Chem. B* **2014**, *118*, 14157–14167.
- [143] Qian, H.; Eckenhoff, W. T.; Zhu, Y.; Pintauer, T.; Jin, R. Total Structure Determination of Thiolate-Protected Au₃₈ Nanoparticles. *J. Am. Chem. Soc.* **2010**, *132*, 8280–8281.
- [144] Tian, S.; Li, Y.-Z.; Li, M.-B.; Yuan, J.; Yang, J.; Wu, Z.; Jin, R. Structural isomerism in gold nanoparticles revealed by X-ray crystallography. *Nat. Commun.* **2015**, *6*, 8667.
- [145] Zeng, C.; Chen, Y.; Liu, C.; Nobusada, K.; Rosi, N. L.; Jin, R. Gold tetrahedra coil up: Kekulé-like and double helical superstructures. *Sci. Adv.* **2015**, *1*, e1500425.
- [146] Zhuang, S.; Liao, L.; Zhao, Y.; Yuan, J.; Yao, C.; Liu, X.; Li, J.; Deng, H.; Yang, J.; Wu, Z. Is the kernel–staples match a key–lock match? *Chem. Sci.* **2018**, *9*, 2437–2442.
- [147] Zhuang, S.; Liao, L.; Yuan, J.; Xia, N.; Zhao, Y.; Wang, C.; Gan, Z.; Yan, N.; He, L.; Li, J.; Deng, H.; Guan, Z.; Yang, J.; Wu, Z. Fcc versus Non-fcc Structural Isomerism of Gold Nanoparticles with Kernel Atom Packing Dependent Photoluminescence. *Angewandte Chemie Int. Ed.* **2019**, *58*, 4510–4514.
- [148] Zeng, C.; Chen, Y.; Iida, K.; Nobusada, K.; Kirschbaum, K.; Lambright, K. J.; Jin, R. Gold Quantum Boxes: On the Periodicities and the Quantum Confinement in the Au₂₈, Au₃₆, Au₄₄, and Au₅₂ Magic Series. *J. Am. Chem. Soc.* **2016**, *138*, 3950–3953.

- [149] Zhuang, S.; Liao, L.; Li, M.-B.; Yao, C.; Zhao, Y.; Dong, H.; Li, J.; Deng, H.; Li, L.; Wu, Z. The fcc structure isomerization in gold nanoclusters. *Nanoscale* **2017**, *9*, 14809–14813.
- [150] Zeng, C.; Liu, C.; Chen, Y.; Rosi, N. L.; Jin, R. Atomic Structure of Self-Assembled Monolayer of Thiolates on a Tetragonal Au₉₂ Nanocrystal. *J. Am. Chem. Soc.* **2016**, *138*, 8710–8713.
- [151] Heinecke, C. L.; Ni, T. W.; Malola, S.; Mäkinen, V.; Wong, O. A.; Häkkinen, H.; Ackerson, C. J. Structural and Theoretical Basis for Ligand Exchange on Thiolate Monolayer Protected Gold Nanoclusters. *J. Am. Chem. Soc.* **2012**, *134*, 13316–13322.
- [152] Yan, N.; Xia, N.; Liao, L.; Zhu, M.; Jin, F.; Jin, R.; Wu, Z. Unraveling the long-pursued Au₁₄₄ structure by x-ray crystallography. *Sci. Adv.* **2018**, *4*, eaat7259.
- [153] Jadzinsky, P. D.; Calero, G.; Ackerson, C. J.; Bushnell, D. A.; Kornberg, R. D. Structure of a Thiol Monolayer-Protected Gold Nanoparticle at 1.1 Å Resolution. *Science* **2007**, *318*, 430–433.
- [154] Das, A.; Liu, C.; Byun, H. Y.; Nobusada, K.; Zhao, S.; Rosi, N.; Jin, R. Structure Determination of [Au₁₈(SR)₁₄]. *Angewandte Chemie Int. Ed.* **2015**, *54*, 3140–3144.
- [155] Ong, S. P.; Richards, W. D.; Jain, A.; Hautier, G.; Kocher, M.; Cholia, S.; Gunter, D.; Chevrier, V. L.; Persson, K. A.; Ceder, G. Python Materials Genomics (pymatgen): A robust, open-source python library for materials analysis. *Comput. Mater. Sci.* **2013**, *68*, 314–319.
- [156] Shimanouchi, T. Tables of molecular vibrational frequencies, consolidated volume I. *National Bureau Stand.* **1972**, 1–160.
- [157] Tlahuice-Flores, A.; Whetten, R. L.; Jose-Yacaman, M. Vibrational Normal Modes of Small Thiolate-Protected Gold Clusters. *J. Phys. Chem. C* **2013**, *117*, 12191–12198.
- [158] Akola, J.; Kacprzak, K. A.; Lopez-Acevedo, O.; Walter, M.; Grönbeck, H.; Häkkinen, H. Thiolate-Protected Au₂₅ Superatoms as Building Blocks: Dimers and Crystals. *J. Phys. Chem. C* **2010**, *114*, 15986–15994.
- [159] Juarez-Mosqueda, R.; Malola, S.; Häkkinen, H. Ab initio molecular dynamics studies of Au₃₈(SR)₂₄ isomers under heating. *Eur. Phys. J. D* **2019**, *73*, 62.
- [160] Li, Y.; Zhou, M.; Jin, R. Programmable Metal Nanoclusters with Atomic Precision. *Adv. Mater.* **2021**, *33*, 2006591.
- [161] Cao, Y.; Malola, S.; Matus, M. F.; Chen, T.; Yao, Q.; Shi, R.; Häkkinen, H.; Xie, J. Reversible isomerization of metal nanoclusters induced by intermolecular interaction. *Chem* **2021**, *7*, 2227–2244.

- [162] Heaven, M. W.; Dass, A.; White, P. S.; Holt, K. M.; Murray, R. W. Crystal Structure of the Gold Nanoparticle $[\text{N}(\text{C}_8\text{H}_{17})_4][\text{Au}_{25}(\text{SCH}_2\text{CH}_2\text{Ph})_{18}]$. *J. Am. Chem. Soc.* **2008**, *130*, 3754–3755.
- [163] Zhu, M.; Aikens, C. M.; Hollander, F. J.; Schatz, G. C.; Jin, R. Correlating the Crystal Structure of A Thiol-Protected Au_{25} Cluster and Optical Properties. *J. Am. Chem. Soc.* **2008**, *130*, 5883–5885.
- [164] Matus, M. F.; Malola, S.; Bonilla, E. K.; Barngrover, B. M.; Aikens, C. M.; Häkkinen, H. A topological isomer of the $\text{Au}_{25}(\text{SR})_{18}$ - nanocluster. *Chem. Commun.* **2020**, *56*, 8087–8090.
- [165] Kalenius, E.; Malola, S.; Matus, M. F.; Kazan, R.; Bürgi, T.; Häkkinen, H. Experimental Confirmation of a Topological Isomer of the Ubiquitous $\text{Au}_{25}(\text{SR})_{18}$ Cluster in the Gas Phase. *J. Am. Chem. Soc.* **2021**, *143*, 1273–1277.
- [166] Dainese, T.; Antonello, S.; Bogialli, S.; Fei, W.; Venzo, A.; Maran, F. Gold Fusion: From $\text{Au}_{25}(\text{SR})_{18}$ to $\text{Au}_{38}(\text{SR})_{24}$, the Most Unexpected Transformation of a Very Stable Nanocluster. *ACS Nano* **2018**, *12*, 7057–7066.
- [167] Zeng, C.; Liu, C.; Pei, Y.; Jin, R. Thiol Ligand-Induced Transformation of $\text{Au}_{38}(\text{SC}_2\text{H}_4\text{Ph})_{24}$ to $\text{Au}_{36}(\text{SPh-t-Bu})_{24}$. *ACS Nano* **2013**, *7*, 6138–6145.
- [168] Salassa, G.; Sels, A.; Mancin, F.; Bürgi, T. Dynamic Nature of Thiolate Monolayer in $\text{Au}_{25}(\text{SR})_{18}$ Nanoclusters. *ACS Nano* **2017**, *11*, 12609–12614.
- [169] Fernando, A.; Aikens, C. M. Ligand Exchange Mechanism on Thiolate Monolayer Protected $\text{Au}_{25}(\text{SR})_{18}$ Nanoclusters. *J. Phys. Chem. C* **2015**, *119*, 20179–20187.
- [170] Grönbeck, H.; Walter, M.; Häkkinen, H. Theoretical Characterization of Cyclic Thiolated Gold Clusters. *J. Am. Chem. Soc.* **2006**, *128*, 10268–10275.
- [171] Corbierre, M. K.; Lennox, R. B. Preparation of Thiol-Capped Gold Nanoparticles by Chemical Reduction of Soluble $\text{Au}(\text{I})$ -Thiolates. *Chem. Mater.* **2005**, *17*, 5691–5696.
- [172] Chen, S.; Templeton, A. C.; Murray, R. W. Monolayer-Protected Cluster Growth Dynamics. *Langmuir* **2000**, *16*, 3543–3548.
- [173] Hostetler, M. J.; Wingate, J. E.; Zhong, C.-J.; Harris, J. E.; Vachet, R. W.; Clark, M. R.; Londono, J. D.; Green, S. J.; Stokes, J. J.; Wignall, G. D.; Glish, G. L.; Porter, M. D.; Evans, N. D.; Murray, R. W. Alkanethiolate Gold Cluster Molecules with Core Diameters from 1.5 to 5.2 nm: Core and Monolayer Properties as a Function of Core Size. *Langmuir* **1998**, *14*, 17–30.
- [174] Häkkinen, H.; Walter, M.; Grönbeck, H. Divide and Protect: Capping Gold Nanoclusters with Molecular Gold–Thiolate Rings. *J. Phys. Chem. B* **2006**, *110*, 9927–9931.

- [175] Dass, A.; Stevenson, A.; Dubay, G. R.; Tracy, J. B.; Murray, R. W. Nanoparticle MALDI-TOF mass spectrometry without fragmentation: Au₂₅(SCH₂CH₂Ph)₁₈ and mixed monolayer Au₂₅(SCH₂CH₂Ph)_(18-x)(L)_(x). *J. Am. Chem. Soc.* **2008**, *130*, 5940–5946.
- [176] Negishi, Y.; Takasugi, Y.; Sato, S.; Yao, H.; Kimura, K.; Tsukuda, T. Kinetic stabilization of growing gold clusters by passivation with thiolates. *J. Phys. Chem. B* **2006**, *110*, 12218–12221.
- [177] Schaaff, T. G.; Shafigullin, M. N.; Khoury, J. T.; Vezmar, I.; Whetten, R. L. Properties of a ubiquitous 29 kDa Au:SR cluster compound. *J. Phys. Chem. B* **2001**, *105*, 8785–8796.
- [178] Shichibu, Y.; Negishi, Y.; Tsukuda, T.; Teranishi, T. Large-Scale Synthesis of Thiolated Au₂₅ Clusters via Ligand Exchange Reactions of Phosphine-Stabilized Au₁₁ Clusters. *J. Am. Chem. Soc.* **2005**, *127*, 13464–13465.
- [179] Fields-Zinna, C. A.; Sardar, R.; Beasley, C. A.; Murray, R. W. Electrospray Ionization Mass Spectrometry of Intrinsically Cationized Nanoparticles, [Au_{144/146}(SC₁₁H₂₂N(CH₂CH₃)₃₊)_x(S(CH₂)₅CH₃)_y]_{x+}. *J. Am. Chem. Soc.* **2009**, *131*, 16266–16271.
- [180] Truttmann, V.; Drexler, H.; Stöger-Pollach, M.; Kawawaki, T.; Negishi, Y.; Barrabés, N.; Rupprechter, G. CeO₂ Supported Gold Nanocluster Catalysts for CO Oxidation: Surface Evolution Influenced by the Ligand Shell. *ChemCatChem* **2022**, *14*, e202200322.
- [181] Zhang, B.; Sels, A.; Salassa, G.; Pollitt, S.; Truttmann, V.; Rameshan, C.; Llorca, J.; Olszewski, W.; Rupprechter, G.; Bürgi, T.; Barrabés, N. Ligand Migration from Cluster to Support: A Crucial Factor for Catalysis by Thiolate-protected Gold Clusters. *ChemCatChem* **2018**, *10*, 5372–5376.
- [182] Krishnadas, K. R.; Ghosh, A.; Baksi, A.; Chakraborty, I.; Natarajan, G.; Pradeep, T. Intercluster Reactions between Au₂₅(SR)₁₈ and Ag₄₄(SR)₃₀. *J. Am. Chem. Soc.* **2016**, *138*, 140–148.
- [183] Neumaier, M.; Baksi, A.; Weis, P.; Schneider, E. K.; Chakraborty, P.; Hahn, H.; Pradeep, T.; Kappes, M. M. Kinetics of Intercluster Reactions between Atomically Precise Noble Metal Clusters [Ag₂₅(DMBT)₁₈]⁻ and [Au₂₅(PET)₁₈]⁻ in Room Temperature Solutions. *J. Am. Chem. Soc.* **2021**, *143*, 6969–6980.
- [184] Salassa, G.; Krishnadas, K. R.; Pupier, M.; Viger-Gravel, J.; Bürgi, T. Role of Intercluster and Interligand Dynamics of [Ag₂₅(DMBT)₁₈]⁻ Nanoclusters by Multinuclear Magnetic Resonance Spectroscopy. *J. Phys. Chem. C* **2021**, *125*, 2524–2530.

- [185] Mortensen, J. J.; Hansen, L. B.; Jacobsen, K. W. Real-space grid implementation of the projector augmented wave method. *Phys. Rev. B* **2005**, *71*, 035109.
- [186] Enkovaara, J. et al. Electronic structure calculations with GPAW: a real-space implementation of the projector augmented-wave method. *J. Phys.: Condens. Matter* **2010**, *22*, 253202.
- [187] Perdew, J. P.; Burke, K.; Ernzerhof, M. Generalized gradient approximation made simple. *Phys. Rev. Lett.* **1996**, *77*, 3865.
- [188] Lysogorskiy, Y.; Bochkarev, A.; Mrovec, M.; Drautz, R. Active learning strategies for atomic cluster expansion models. *Phys. Rev. Mater.* **2023**, *7*, 043801.
- [189] Bochkarev, A.; Lysogorskiy, Y.; Menon, S.; Qamar, M.; Mrovec, M.; Drautz, R. Efficient parametrization of the atomic cluster expansion. *Phys. Rev. Mater.* **2022**, *6*, 013804.
- [190] Christensen, A. S.; Lilienfeld, O. A. v. On the role of gradients for machine learning of molecular energies and forces. *Mach. Learn. Sci. Technol.* **2020**, *1*, 045018.
- [191] Thompson, A. P.; Aktulga, H. M.; Berger, R.; Bolintineanu, D. S.; Brown, W. M.; Crozier, P. S.; in 't Veld, P. J.; Kohlmeyer, A.; Moore, S. G.; Nguyen, T. D.; Shan, R.; Stevens, M. J.; Tranchida, J.; Trott, C.; Plimpton, S. J. LAMMPS - a flexible simulation tool for particle-based materials modeling at the atomic, meso, and continuum scales. *Comput. Phys. Commun.* **2022**, *271*, 108171.
- [192] Stukowski, A. Visualization and analysis of atomistic simulation data with OVITO—the Open Visualization Tool. *Model. Simul. Mater. Sci. Eng.* **2009**, *18*, 015012.
- [193] Qi, W. H.; Wang, M. P. Size effect on the cohesive energy of nanoparticle. *J. Mater. Sci. Lett.* **2002**, *21*, 1743–1745.
- [194] Xiong, S.; Qi, W.; Huang, B.; Wang, M. Size-, Shape- and Composition-Dependent Alloying Ability of Bimetallic Nanoparticles. *ChemPhysChem* **2011**, *12*, 1317–1324.
- [195] Qi, W. H.; Huang, B. Y.; Wang, M. P. Size and shape-dependent formation enthalpy of binary alloy nanoparticles. *Phys. B: Condens. Matter* **2009**, *404*, 1761–1765.
- [196] Piccolo, L.; Li, Z. Y.; Demiroglu, I.; Moyon, F.; Konuspayeva, Z.; Berhault, G.; Afanasiev, P.; Lefebvre, W.; Yuan, J.; Johnston, R. L. Understanding and controlling the structure and segregation behaviour of AuRh nanocatalysts. *Sci. Reports* **2016**, *6*, 35226.
- [197] Vanzan, M.; Jones, R. M.; Corni, P. S.; D'Agosta, P. R.; Baletto, P. F. Exploring AuRh Nanoalloys: A Computational Perspective on the Formation and Physical Properties. *Chemphyschem* **2022**, *23*.

- [198] Valizadeh, Z.; Abbaspour, M. Surface energy, relative stability, and structural properties of Au-Pt, Au-Rh, Au-Cu, and Au-Pd nanoclusters created in inert-gas condensation process using MD simulation. *J. Phys. Chem. Solids* **2020**, *144*, 109480.
- [199] Chen, P.-C.; Liu, M.; Du, J. S.; Meckes, B.; Wang, S.; Lin, H.; Dravid, V. P.; Wolverton, C.; Mirkin, C. A. Interface and heterostructure design in polyelemental nanoparticles. *Science* **2019**, *363*, 959–964.
- [200] Lan, J.; Palizhati, A.; Shuaibi, M.; Wood, B. M.; Wander, B.; Das, A.; Uyttendaele, M.; Zitnick, C. L.; Ulissi, Z. W. AdsorbML: a leap in efficiency for adsorption energy calculations using generalizable machine learning potentials. *npj Comput. Mater.* **2023**, *9*, 1–9.
- [201] Gasteiger, J.; Shuaibi, M.; Sriram, A.; Günnemann, S.; Ulissi, Z.; Zitnick, C. L.; Das, A. GemNet-OC: Developing Graph Neural Networks for Large and Diverse Molecular Simulation Datasets. 2022; <http://arxiv.org/abs/2204.02782>, arXiv:2204.02782 [cond-mat, physics:physics].
- [202] Chanussot, L. et al. Open Catalyst 2020 (OC20) Dataset and Community Challenges. *ACS Catal.* **2021**, *11*, 6059–6072.